5-2022

NOVEL REGULATORS OF CELLULAR SECRETION ALTER THE TUMOR MICROENVIRONMENT TO DRIVE METASTASIS

Rakhee Bajaj

NOVEL REGULATORS OF CELLULAR SECRETION ALTER THE TUMOR MICROENVIRONMENT TO DRIVE METASTASIS

By

Rakhee Bajaj, M.Sc.

APPROVED:

_____
Don L. Gibbons, M.D., Ph.D.
Advisory Professor

_____
Michelle Barton, Ph.D.
Advisory Professor

_____
Jonathan Kurie, M.D.
Advisory Professor

_____
Sendurai Mani, Ph.D.
Advisory Professor

_____
George Calin, Ph.D.
Advisory Professor

APPROVED:

_____
Dean, The University of Texas
MD Anderson Cancer Center UTHealth Graduate School of Biomedical Sciences

NOVEL REGULATORS OF CELLULAR SECRETION ALTER THE TUMOR MICROENVIRONMENT TO DRIVE METASTASIS

A

DISSERTATION

Presented to the Faculty of

The University of Texas

MD Anderson Cancer Center UTHealth

Graduate School of Biomedical Sciences

in Partial Fulfillment

of the Requirements

for the Degree of

DOCTOR OF PHILOSOPHY

by

Rakhee Bajaj, M.Sc.
Houston, Texas

May, 2022

Dedication

To all the kids who wanted a microscope instead of a toy for their birthday,

Embrace the weird.

Acknowledgements

The people you surround yourself with during your PhD journey define how you remember the experience. I am lucky to have found folks who supported and encouraged me every step of the way. Hence, I would like to acknowledge them for all their help, patience, and guidance.

First, I would like to thank my mentor, Dr. Don Gibbons for taking a chance on me and believing in me, despite all my many mishaps in the lab. Your guidance and trust in me have given me the confidence to get out of my comfort zone and experience new things. It gives me the conviction for the career track I have now decided to take. So, thank you for being an amazing mentor and scientist who always challenged and encouraged me.

Having a wonderful advisory committee made for productive and not-so stressful committee meetings. So, thank you Drs. Michelle Barton, Jonathan Kurie, Sendurai Mani, and George Calin for having discussions with me like a peer. I would like to especially acknowledge Dr. Michelle Barton for giving me a chance to rotate in her lab, and being the person I can finally call my role model. I will always be grateful for your mentorship, guidance, and the ability to make science fun and relaxed. I would also like to thank Dr. Jonathan Kurie for sharing all his wisdom regarding the Golgi. My project would not be where it is without his assistance.

No research is possible without the generous awards, scholarships and grants. Hence, I would like to recognize GSBS and the donors for the scholarships and grants I received: T. C. Hsu scholarship and Drs. Khandan Keyomarsi and Stephanie Watowich for the CPRIT Research Training Grant (RP170067).

Next, I would like to thank the current and past members of the Gibbons lab for making it an amazing place for science and discovery: Dr. Samrat Kundu, Dr. Jessica Konen, Dr. Bertha Rodriguez (Letty), Dr. David Peng, Dr. Roxsan Manshouri, Dr. Aparna Padhye, Laura Gibson, Jared Fradette, Amanda Warner, Haoyi Wu, Mabel Perez-Oquendo, Dr. Joshua Ochieng, and Dr. Limo Chen. I especially recognize: Sam for training me on experiments and on how to ask the right questions; Jessica for advising me in the fields of science, TV shows, restaurants-to-try, and shopping; Letty, and David for always being available to answer my stupidest doubts and for brainstorming ideas; and Roxsan for always finding me in the tissue culture room and distracting me with coffee or thai food. I will always look back at my time in the lab with fondness and nostalgia. Outside our lab, I would like to thank Drs. Priyam Bannerjee, Xiaochao Tan, and Guan-yu Xiao for all their help with my work on the Golgi.

I was very fortunate to find friends who made graduate school and Houston more enjoyable and memorable. Drs. Merve and Cem Dede for being some of the most genuine, generous, and caring people I have had the pleasure to meet. The times with Merve when we laughed until we cried made all my failures during graduate school seem insignificant. I am also grateful to: Tanvi Visal for all our ‘w(h)ine & dine’ nights that revived us before the next failed experiment, Mary Figueroa for being up for trying new restaurants and exploring Houston, and for being nice to me on her birthday; to Hannah Savage for always saying the right thing to calm me down about grad school or life in general, and to Dr. Walaa Kattan for all our study sessions during candidacy – not sure how I would’ve managed to get through the exam without those.

I would also like to thank Anand Bagaria for always finding the time (India time) to help me practice for my hour-long presentations because ‘if he gets it, anyone will’.

Finally, I owe my deepest gratitude to my family. My mother, Sudha Bajaj, who has been my only constant cheerleader since I was sixteen and who has supported all my decisions that have helped me get to where I am. My father, Krishnakumar Bajaj, for having my back and trusting me to be in another country by myself at the age of seventeen. I owe all my success in life to their unconditional love, support, and dedication. My uncle and aunt, Om Prakash and Rajashree Bajaj, for their love and guidance. My crazy siblings: Supriya Bajaj, Kushal Bajaj, Khushboo Bajaj, Priyanka Bajaj, and Deepali Khetan for always being there, for their encouragement, and for showing me the balance between work and life – a way to stay sane during grad school. My grandfather, Girdharilal Bajaj, and his guru, Satyanarayan Goenka, for showing me the principles that have helped shape my work and life ethics. Lastly, my partner, Aloy Das Mahapatra (Ollie) for being the first person I call when I receive an acceptance or a rejection. Thank you for your patience, love, support, and encouragement as I achieve my dreams. My answer is yes, I will!

NOVEL REGULATORS OF CELLULAR SECRETION ALTER THE TUMOR MICROENVIRONMENT TO DRIVE METASTASIS

Rakhee Bajaj, M.Sc.

Advisory Professor: Don L. Gibbons, M.D., Ph.D.

Lung cancer is a highly aggressive disease responsible for ~25% of all cancer-related deaths, due in part to its proclivity to metastasize. Treating metastasis holds potential for improving patient survival but requires a deeper investigation into the underlying mechanisms. Some of these processes that can regulate metastasis are: (1) Oncogenic targets of epithelial micro-RNAs (miRNAs) are epigenetically de-repressed upon loss of the miRNAs during epithelial-to-mesenchymal transition (EMT) and in cancer. EMT confers plasticity and fitness to cancer cells promoting their survival through the metastatic cascade. This cascade and EMT are initiated by loss of the miRNA200 family (miR-200) and the miRNA-96 cluster (miR~96), which allows its targets to be de-repressed in mesenchymal cells. Targets that are upregulated by the loss of miR-200 and miR~96 are Zeb1 and Foxf2, which associate with metastasis and poor patient prognosis. (2) Altered Golgi morphology and enhanced Golgi exocytosis during EMT promotes lung cancer metastasis. Zeb1-mediated EMT regulates Golgi dynamics and integrity, thereby enhancing and polarizing Golgi exocytosis to the invasive front of the tumors to promote metastasis. Altered Golgi functions promote secretion of extracellular components like MMPs, collagens, glycosaminoglycans, cytokines, etc., thus priming the tumor microenvironment for malignancy. However, the drivers that orchestrate these changes in the Golgi remain undefined. Additionally, inhibiting Golgi secretion has been unsuccessful for treating

metastatic lung cancer in the clinic. Thus, improving our understanding of regulators of Golgi integrity and exocytosis will aid in impeding this dynamic process to treat metastasis.

In this dissertation, using a high-throughput invasion screen, I established Impad1 and Kdelr2 as robust, independent drivers of lung cancer invasion and metastasis. I further elucidated that Impad1 is a novel target of the epithelial miRNAs, miR-200 and miR~96, and is de-repressed during EMT. Impad1 modulates Golgi morphology, and vesicular trafficking through its interaction with a trafficking protein, Syt11. These changes in the Golgi dynamics alter the extracellular matrix and the immune landscape to promote invasion and metastasis. Inhibiting Impad1 disrupted the cancer cell secretome, reversed the invasive phenotype, and enhanced anti-tumor immune surveillance. I identified Impad1 as a novel functional link that connects EMT- and Golgi secretome-mediated changes to lung cancer metastasis. Additionally, I demonstrated that Kdelr2 also enhances Golgi-mediated exocytosis of MMPs to drive invasion and metastasis; however, it works independent of EMT. Hence, the data highlights that EMT is sufficient but not necessary to modulate Golgi dynamics and secretion during cancer malignancy. Collectively, this work signifies the importance of the Golgi and cellular secretion in lung cancer progression. Moreover, it also establishes novel drivers that can be targeted to control Golgi-mediated exocytosis, thereby impeding metastatic disease.

Table of Contents

List of Illustrations

List of Tables

Abbreviations

NSCLC – Non-small cell lung cancer

SCLC – Small cell lung cancer

LuAd – Lung adenocarcinoma

ECM – Extracellular matrix

GEMMs – Genetically-engineered mouse models

GOF – Gain-of-function

LOF – Loss-of-function

KP – $Kras^{G12D}$,$p53^{R172H\Delta G}$

EMT – Epithelial-to-mesenchymal transition

MET – Mesenchymal-to-epithelial transition

miRNA - microRNA

miR-200 – miRNA-200 family (miR-200a/b/c/429/141)

miR~96 – miRNA-96 cluster (miR~96/183/182)

3’-UTR – 3’ untranslated region

TGFβ – Transforming growth factor β

KM – $KRAS^{LSLG12D/+}$;$miR\text{-}200c^{fl/fl}$

KPM200 – $KRAS^{LSLG12D/+}$;$p53^{R172H}$;$miR\text{-}200c^{fl/fl}$

KM96 – $KRAS^{LSLG12D/+}$;$miR\sim96c^{fl/fl}$

ER – Endoplasmic reticulum

PM – Plasma membrane

EC – Extracellular space

PTM – Post-translational modification

KDELR - KDEL endoplasmic reticulum protein retention receptor

TIME – Tumor immune microenvironment

MMPs – Matrix metalloproteases

GAGs – Glycosaminoglycans

TIMP-1 - Tissue inhibitor of metalloproteinase-1

CS – Chondroitin sulfate

HS – Heparan sulfate

TCGA – The cancer genome atlas

ORFs – open reading frames

RT – room temperature

FBS – Fetal bovine serum

PBS – Phosphate buffered saline

BFA – Brefeldin A

CM – Conditioned media

SQ – Subcutaneous

TBS-T – 10 mM Tris, 100 mM NaCl, and 0.1% Tween 20

cDNA – complementary DNA

SDS-PAGE – SDS-polyacrylamide gel electrophoresis

Impad1 – Inositol Monophosphatase domain containing 1

Kdelr2 – KDEL endoplasmic reticulum protein retention receptor 2

ERGIC – Endoplasmic Reticulum Golgi intermediary complex

GAGs – Glycosaminoglycans

Chapter 1: Introduction

1.1 Lung Cancer

Lung cancer is responsible for the highest cancer-related mortality in the United States and worldwide, surpassing the subsequent two leading cancer types combined (Siegel, Miller, Fuchs, & Jemal, 2022). More importantly it is predicted to remain the leading cause of cancer-deaths until 2040 (Rahib, Wehner, Matrisian, & Nead, 2021). Lung cancer can be divided into two major histologic forms: non-small cell lung cancer (NSCLC) and small cell lung cancer (SCLC). NSCLC, which is the predominant type occurring in 85% of lung cancer patients, can be further subdivided into lung adenocarcinoma (LuAd), squamous cell carcinoma, and large cell subtypes (Herbst, Heymach, & Lippman, 2008).

1.1.1 Lung cancer metastasis

The high mortality in NSCLC patients is primarily due to the propensity of lung cancer cells to metastasize, where 45% of the cases are diagnosed with late-stage metastatic disease (Siegel et al., 2022). Metastasis is a dynamic, multi-step cascade during which cancer cells disseminate from the primary tumor, invade through the extracellular matrix (ECM), intravasate, travel through the circulatory system, extravasate, and form secondary tumors at distant locations. Treatments that prevent, or slowdown NSCLC metastasis are predicted to improve patient outcome (Eccles, Chatterjee, & Rodger, 2017; Steeg & Theodorescu, 2008). New therapies have shown promise in treating NSCLC, which include: (1) Immunotherapy – Atezolizumab, Nivolumab, Pembrolizumab, and Durvalumab. (2) Targeted therapy – EGFR

inhibitors, BRAF inhibitors, ROS1 inhibitors, and ALK inhibitors, to name a few (Lim, Hong, & Kim, 2020; Yuan, Huang, Chen, Wu, & Xu, 2019). However, the 5-year survival as well as the predicted deaths in the next two decades for lung cancer have improved minimally despite extensive research in the field due to the complexity and incomplete understanding of the metastatic cascade.

1.1.2 Models to study lung cancer progression and metastasis

To further our understanding of lung cancer progression and metastasis, various syngeneic and genetically-engineered mouse models (GEMMs) have been developed (Gibbons, Byers, & Kurie, 2014). Spontaneous gain-of-function (GOF) of the oncogene Kras via the *Kras*^{G12D} mutation enables mice to form non-metastatic lung adenocarcinoma (denoted as Kras) (Gibbons, Lin, Creighton, Zheng, et al., 2009). Introduction of a *Tp53*$^{R172H\Delta G}$ mutation, associated with the Li Fraumeni disease, allows the double mutant lung adenocarcinoma tumors (denoted as Kras$^{G12D/+}$,p53 $^{R172H\Delta G}$ – KP) to become malignant (S. Zheng, El-Naggar, Kim, Kurie, & Lozano, 2007). These KP mice develop metastatic lung adenocarcinoma that recapitulate lung cancer patient disease, thus making it an excellent model to study NSCLC. Furthermore, our group developed cell lines from the primary tumors as well as the various metastatic lesions of the KP mice and re-implanted them into syngeneic mice (129/Sv) to stratify them based on their metastatic abilities (i.e. KP cell panel) (Gibbons, Lin, Creighton, Rizvi, et al., 2009). Cell lines from the primary tumors (eg. 393P) showed no metastatic lesions, whereas those from the subcutaneous (eg. 344SQ) or lymph node (eg. 344LN) metastases were highly aggressive. There are also human NSCLC cell lines that were used to recapitulate the work in patient-

resembling models. These include cell lines such as the Kras mutant lines H358 and A549, the Kras, P53 mutant lines H441, H157, and H1299, as well as an EGFR mutant line HCC827. These models with the same fundamental genetic alterations ($Kras^{G12D}$,$p53^{R172H\Delta G}$) presenting distinct invasive and metastatic ability indicate that genetic drivers in addition to Kras and p53 are responsible for promoting cancer cell invasion and metastasis.

1.2 Role of epithelial-to-mesenchymal transition (EMT) in lung cancer metastasis

Epithelial-to-mesenchymal transition (EMT) is a physiological process by which epithelial cells lose their apical-basal polarity and gain mesenchymal characteristics that allow them to disseminate and migrate from their place of origin (Kalluri & Weinberg, 2009; Thiery, Acloque, Huang, & Nieto, 2009). EMT is reversible where mesenchymal-like (mesenchymal) cells can undergo a mesenchymal-to-epithelial transition (MET) to revert to their original state. Cells undergo EMT during three biological processes: differentiation (type 1), wound healing (type 2), and cancer (type 3). Despite the different biological processes associated with the distinct types of EMT, the underlying signals and mechanisms regulating them overlap. Type 1 EMT is imperative during implantation, embryonic gastrulation, and organ development but does not lead to fibrosis or invasiveness. Type 2 EMT is repair-associated that is induced upon trauma, produces fibroblasts and other cells required for healing, and terminates once inflammation is attenuated. Lastly, type 3 EMT occurs in cancer cells and is hypothesized to allow tumor cells to dissociate from the primary tumor, invade

through the ECM, and metastasize to secondary locations. Like in other epithelial cancers, EMT plays a key role in lung cancer progression and metastasis. In addition to metastasis, EMT also promotes fitness of cancer cells by conferring stemness, and resistance to drug- and chemo- therapy to the cells (Ferrarotto et al., 2016; Shibue & Weinberg, 2017; Zhang et al., 2014; X. Zheng et al., 2015). Moreover, mesenchymal cells alter the tumor immune microenvironment (TIME) and regulate response to immunotherapy; hence indicating the possibility of using EMT-mediated secretion as a predictive biomarker for immunotherapy response (Chen et al., 2014; Lou et al., 2016).

1.2.1 Zeb1 and epithelial microRNAs (miRNAs) are key regulators of EMT

EMT is finely regulated by a multitude of factors including transcription regulators, miRNAs, and external stimuli (Ma & Weinberg, 2008; Tsai & Yang, 2013; Yang & Weinberg, 2008). These factors also correlate with the EMT status of the cells and are termed EMT markers. Byers et al. identified a 76-gene signature in lung cancer that can be used to determine the EMT state of the cell (Byers et al., 2013). Our group and others have shown that the Zeb1 transcription factor and epithelial miRNAs, the miRNA-200 family (miR-200) and the miRNA-96 cluster (miR~96), are key regulators of EMT in lung cancer (Larsen et al., 2016). Using our KP GEMMs and cell models we have shown that Zeb1 and the epithelial miRNAs are part of a double-negative feedback loop that modulate EMT, and correlate with the EMT status of the cells (Gibbons, Lin, Creighton, Rizvi, et al., 2009). miRNAs are small, non-coding RNAs that regulate gene transcription by binding to the 3’-untranslated region (3’-

UTR) of the mRNA. Once bound, miRNAs hamper translation and/or degrade and destabilize the mRNA. The miR-200 family consists of 5 members: miR-200a, miR-200b, miR-200c, miR-141, and miR-429. miR-200b/c/429, and miR-200a/141 bind to the same seed sequence in the target mRNA, respectively. The miR~96 cluster consists of 3 miRNAs: miR-96, miR-182, and miR-183, which are found on the same chromosome locus. Epithelial cells have high miR-200 and miR~96 levels that repress mesenchymal proteins such as Zeb1, allowing for the expression of epithelial factors like E-cadherin (Philip A. Gregory et al., 2008; Wellner et al., 2009). During EMT, Zeb1 binds to the E-box recognition sites in the promoter of miR-200, miR~96, and epithelial proteins like E-cadherin, thereby inhibiting their transcription; this allows for the presentation of mesenchymal characteristics (Ahn et al., 2012; Burk et al., 2008). Hence high Zeb1, and low miR-200/miR~96/E-cadherin levels are some of the markers for EMT.

1.2.2 De-repression of oncogenes during EMT

EMT markers are used to not only distinguish the mesenchymal state of the cell but have also been associated with lung cancer patient survival. Previous work has shown that loss of miR-200/miR~96 and heightened Zeb1 expression associates with increased metastasis, resistance to therapies, and significantly poor patient survival (Chen et al., 2014; Gibbons, Lin, Creighton, Rizvi, et al., 2009; Gibbons, Lin, Creighton, Zheng, et al., 2009; Manshouri et al., 2019; Meidhof et al., 2015; Padhye et al., 2021; Spaderna et al., 2008; Ungewiss et al., 2016; Wellner et al., 2009). Apart from Zeb1, there are other oncogenes that are derepressed during EMT upon loss of miR-200 and miR~96. One such factor is Foxf2, a transcription activator that is a direct

target of the epithelial miRNAs and is upregulated during EMT (Kundu et al., 2016). Furthermore, Foxf2 drives lung cancer invasion and metastasis, and negatively correlates with patient prognosis. Despite the imperative relation between Zeb1/miR-200/miR~96 and EMT-mediated disease progression, inhibiting Zeb1 or supplementing epithelial miRNAs to regulate EMT and treat metastasis has posed pharmacological challenges (Nieto, Huang, Jackson, & Thiery, 2016). This is primarily due to the ubiquitous role of these factors in modulating cellular pathways, and the heterogeneity of tumor cells that undergo EMT (Padhye et al., 2021). Hence, this requires a better understanding of the processes downstream of EMT that drive metastasis and can be selectively inhibited in mesenchymal cells.

1.2.3 Models to study EMT

We have previously developed several cell line and mouse models in the lab to study the process of EMT. Doxycycline induction of epithelial state regulators, miR-200 and miR~96, in mesenchymal murine (344SQ) and human (H157) cells caused them to undergo MET, thereby bestowing epithelial characteristics, and making them less invasive and metastatic (Kundu et al., 2016; D. H. Peng et al., 2019). Conversely, Zeb1 induction in epithelial murine (393P) and human (H441) cells promoted EMT, thereby making the cells more mesenchymal, invasive, and metastatic. Furthermore, treating the KP murine and human NSCLC cell lines with TGFβ, a cytokine belonging to the transforming growth factor family, also drives EMT, and invasion and metastasis of the cells (Gregory et al., 2011).

We also established GEMMs that develop heterogenous tumors that are more recapitulative of disease progression in patients (Padhye et al., 2021; D. H. Peng et

al., 2019). Briefly, miR-200 (miR-200c$^{-/-}$) or miR~96 (miR~96c$^{-/-}$) conditionally floxed mice were crossed with the previously described KRAS (KRAS$^{G12D/+}$) or KP (KRAS$^{G12D/+}$;p53$^{-/-}$) mice to give KRAS$^{G12D/+}$;miR-200c$^{-/-}$ (KM200), KRAS$^{LSLG12D/+}$;p53$^{-/-}$;miR-200c$^{-/-}$ (KPM200), and KRAS$^{G12D/+}$;miR~96c$^{-/-}$ (KM96) GEMMs. These KM, KPM200, and KM96 mice developed tumors that were heterogenous, mesenchymal, and malignant, thus making it an exceptional model to study the role of EMT in lung cancer metastasis. Syngeneic cell lines were derived from the KPM200 tumors in order to study inherent vs acquired EMT.

1.3 Role of Golgi dynamics in cancer

Proper protein trafficking—from the endoplasmic reticulum (ER) to the plasma membrane (PM), to various target organelles, or to the extracellular (EC) space—is required for cell survival (Palade, 1975). Alterations in protein secretion can lead to numerous diseases including obesity, diabetes, chronic inflammation, and cancer (Paltridge, Belle, & Khew-Goodall, 2013). Proteins that contain a specific transmembrane domain or a leader sequence are transported to the Golgi where the organelle functions to modify, sort, and traffic the proteins to their destined locations. Briefly, proteins synthesized in the ER travel in an anterograde direction through the *cis*-, *medial*-, and *trans*- Golgi compartments. Trafficked proteins may undergo post-translational modifications (PTMs) in these compartments, where PTMs such as glycosylation or proteolytic cleavage, act as signals for specific receptor interactions that direct the spatial fate of the protein (Lodish H, 2000a, 2000b). Secreted proteins help form the ECM, interact with or modify the ECM, or mediate signaling to other

cells. The Golgi also regulates retrograde transport of proteins from the PM to the Golgi, or from the Golgi to the ER. ER-resident chaperone proteins, like calreticulin and heat shock proteins, contain a KDEL ligand that binds to the Golgi KDEL receptor (KDELR), facilitating return of these proteins back to the ER. Retrograde trafficking allows for the recycling of proteins back to their original site of function (Wiersma, Michalak, Abdullah, Bremer, & Eggleton, 2015b).

The Golgi is responsible for the secretion of components that help form the TME, which includes the cancer cell secretome, the ECM, and the immune landscape (Agrawal, Jwa, Lebrun, Job, & Rakwal, 2010). Hence, alterations in Golgi dynamics of cancer cells can make the secretome, the TIME, and the ECM more malignant (Albacete-Albacete, Sanchez-Alvarez, & Del Pozo, 2021). These changes include altered trafficking, exocytosis, orientation, morphology, and Golgi-mediated PTMs. Golgi-associated gene mutations are ubiquitous across most cancers and are responsible for driving the moderations seen in the Golgi and the TME. For example, in NSCLC, chromosome 1q21-43, which contains many Golgi-related genes involved in trafficking, is frequently amplified and associates with worse patient survival (Tan et al., 2020). This suggests the importance of the organelle in cancer progression and metastasis.

1.3.1 Aberrant Golgi exocytosis, a hallmark of metastatic cells

Vesicular trafficking

Vesicular trafficking has been described as the “intracellular highway to carcinogenesis” (Goldenring, 2013). Proper Golgi-mediated trafficking in cells maintains the steady flow of proteins from the Golgi to other organelles, the cell

surface, and the EC space. Cancer cells hijack this process to exocytose components that eventually remodel the secretome and the TME for metastasis. These components include proteins such as matrix metalloproteases (MMPs), collagens, cytokines, and glycoproteins like glycosaminoglycans (GAGs), and glycolipids, which can determine cancer metastasis (Deryugina & Quigley, 2006; Julien et al., 2009; D. H. Peng et al., 2020; D. H. Peng et al., 2017). Tan et al. demonstrated that Golgi-associated proteins can enhance vesicular trafficking and exocytosis of factors such as MMPs, tissue inhibitor of metalloproteinase-1 (TIMP1), and cytokines (CXCL1, IL-1α, IL-8, VEGF) that promote lung cancer metastasis (Tan et al., 2020). The metastatic cascade in lung cancer includes the secretion of cytokines that frequently alter the TIME by modulating lymphoid-derived or myeloid-derived immune cell populations (Lou et al., 2016). Additionally, GAGs such as chondroitin sulfate (CS), heparan sulfate (HS), and keratan sulfate are critical modifications facilitating the formation of the ECM and are known to assist metastatic outgrowth. For example, Perlecan, an HS proteoglycan core protein, enhances secretion of IL-6 that eventually promotes lung cancer invasion and metastasis (Franses, Baker, Chitalia, & Edelman, 2011). Hence, the malignant nature of these EC factors makes exocytosis a hallmark of cancer metastasis. However, the underlying mechanisms and drivers regulating exocytosis during metastasis remain unclear.

Golgi morphology

Another aspect of the Golgi that also alters exocytosis is its morphology. The Golgi is a dynamic organelle that modifies its structure to accommodate the physiological state of the cell. There are three main states of the Golgi—condensed,

elongated, and fragmented—between which the organelle oscillates in a context-dependent manner. These morphologies have different described effects on cancer metastasis depending on the type of cancer. Lung cancer cells have an EMT-mediated condensed Golgi that enhances trafficking, exocytosis, invasion, and metastasis (Tan et al., 2017). Alternatively, Golgi proteins mediate a ribbon-like elongated Golgi structure that increases exocytosis of pro-invasive components that drive metastatic breast, melanoma, and colon cancers (Makhoul, Gosavi, & Gleeson, 2019), whereas the fragmented Golgi in prostate cancer also promotes carcinogenesis (Petrosyan, 2015, 2019). Thus, targeting the functional morphology of the organelle is a fine-tuned balance and requires a deeper investigation into the key players of the process.

1.3.2 Golgi exocytosis is regulated during EMT

Vesicular trafficking during EMT

EMT is one of the cellular phenomena that repositions and restructures the Golgi to enhance and re-direct traffic towards the leading edge of cells, enabling migratory and invasive behavior (Tan et al., 2017). Zeb1-mediated EMT in lung cancer enhanced anterograde trafficking to the PM, and vesicle tethering to the Golgi. This increased transport promoted secretion of pro-invasive and metastatic factors into the EC space.

Golgi morphology during EMT

Additionally, EMT also leads to compaction and polarization of the Golgi with improved ribbon linking and cisternal stacking (Bui, Mejia, Díaz, & Wang, 2021; Tan et al., 2017). The Golgi proteins orchestrating this correlate with shorter survival in

cancer patients, and direct and enhance protein exocytosis; thereby, driving lung cancer metastasis.

The modification of Golgi dynamics, both trafficking and morphology, during EMT eventually alters the cancer cell secretome and the TME to promote metastasis. Reka et al. performed GeLC-tandem mass spectrometry and identified the secretome signature for cancer cells undergoing TGFβ-induced EMT, which predicted for patient survival (Reka et al., 2014). Our group showed that collagen deposition and crosslinking in the ECM are upregulated during EMT, which in turn enhances integrin/FAK/Src signaling in cancer cells to promote invasion and metastasis (Padhye et al., 2019). Moreover, increased collagen deposition also suppresses an effective immune surveillance of the TIME by leading to an exhausted CD8+ T cell state (D. H. Peng et al., 2020; D. H. Peng et al., 2017). Thus, a link functionally connects EMT, Golgi changes, and the secretome that makes cancer cells more metastatic and resistant to therapy. However, the underlying molecular drivers and mechanisms that define that link remain unclear.

1.3.3 Targeting the Golgi to treat cancer metastasis

Therapeutics targeting protein secretion are an attractive approach to disrupt metastasis as inhibition of secretory pathways can prevent extracellular deposition of pro-tumorigenic factors. The Golgi already has a host of drugs that target aspects of the organelle; thus, limiting and inhibiting cancer-mediated secretion (Zappa, Failli, & De Matteis, 2018). Despite the extraordinary response in preclinical models, there are complications in translating these drugs into the clinic. These include toxicity, low solubility, non-specificity, and compensation from multiple secretory pathways that

have overlapping functions. Therefore, understanding how the Golgi and Golgi-mediated secretion alter the metastatic cascade holds potential for improving patient prognosis through development of diagnostic and therapeutic tools.

1.4 Overview of dissertation research

This dissertation is sectioned into 3 chapters that describe the role of Golgi secretion in altering the TME for lung cancer progression. Overall, the project aims to delineate the underlying mechanisms of metastasis; and establishes Golgi secretion as a key process in the cascade. Furthermore, the project aims to identify the therapeutic vulnerabilities of Golgi secretion in order to prevent or inhibit lung cancer invasion and metastasis.

Chapter 3 focuses on identifying putative drivers of lung cancer invasion by using a high-throughput invasion screen. Functional *in vitro* and *in vivo* assays for invasion and metastasis, respectively, demonstrate that two hits from the screen, Impad1 and Kdelr2, are sufficient and necessary to drive NSCLC invasion and metastasis. Additionally, they alter processes that more specifically modulate tumor metastasis without modifying tumor growth or cellular proliferation. Chapter 4 delves further into the mode-of-regulation of the two hits to understand their role in tumorigenesis. Previously published cell and GEM models of EMT will establish that Impad1 is a direct target of miR-200 and miR~96, and is de-repressed during EMT upon loss of the epithelial miRNAs; thus determining the mechanism of Impad1 upregulation in NSCLC. Alternatively, an EMT-independent regulation of Kdelr2 will also be illustrated. Lastly, chapter 5 investigates the processes regulated by Impad1

and Kdelr2 in order to drive invasion and metastasis. Various Golgi and secretome studies will establish that the two independent drivers of lung cancer metastasis regulate a common cellular pathway: Golgi-mediated exocytosis. Proteomic profiling and in-depth confocal analyses will reveal that Impad1 acts as a functional link that connects EMT to changes in Golgi dynamics that alter the secretome leading to immunesuppression and a malignant TME. An exhaustive Impad1 interactome analysis will further unravel that Impad1 interacts with other trafficking proteins, Syt11 and Arf5, to orchestrate changes in Golgi functions. Additionally, knockdown and inhibition studies indicate that Impad1-mediated changes in the secretome and metastasis is reversible; hence signifying its potential as a therapeutic target for lung cancer. Finally, moving beyond EMT, I demonstrate that Kdelr2 enhances Golgi exocytosis of MMPs to drive invasion and metastasis independent of EMT.

Collectively, this project will improve our understanding of the role of Golgi dynamics and exocytosis in cancer metastasis. Given the complexity in targeting Golgi secretion in the clinic, identifying drivers like Impad1 and Kdelr2, and their interactors will expose novel avenues for therapeutically inhibiting or preventing metastasis. This work also has extensive implications beyond cancer. Firstly, it enhances our basic understanding of Golgi biology and its regulators. Moreover, it provides information that can be used to treat diseases such as chondrodysplasia that are also mediated by alterations in Golgi secretion.

Chapter 2: Materials and methods

Content of this chapter is derived from the publication Bajaj R, Kundu ST, Grzeskowiak CL, Fradette JJ, Scott KL, Creighton CJ, Gibbons DL. “Impad1 and Kdelr2 drive invasion and metastasis by enhancing Golgi-mediated secretion.” *Oncogene*. 2020 Aug 04. PubMed PMID: 32753652 with approval from Nature Publishing Group.

2.1 Screens

Both *in vitro* invasion and *in vivo* metastasis screens were performed in parallel (Bajaj et al., 2020; Grzeskowiak et al., 2018; S. T. Kundu et al., 2018). Candidate genes for both screens were selected by exploiting microarray data collected from the KP GEMMs, as well as the KP cell panel. Genes upregulated in the metastatic lesions as compared to the primary tumors in the KP mice were coincided with the genes upregulated in the syngeneic tumors from the 344SQ metastatic KP cell line as compared to the tumors from the 393P non-metastatic KP cell line. These common genes were then triangulated with genes that showed >1.5-fold copy number amplification in The Cancer Genome Atlas (TCGA) lung adenocarcinoma dataset. 217 candidate genes identified were barcoded and their open reading frames (ORFs) individually overexpressed in the 393P non-invasive, non-metastatic cells.

2.1.1 *In vitro* screen

The 393P overexpressing cells were individually plated in quadruplicates in the 96-well Boyden chamber invasion plates (Corning BioCoat^{TM}, #354167). 12 groups of 20 cell lines each were randomly selected and seeded per plate. The chambers were

prepared as per manufacturer instructions (pre-warmed for 10 mins to room temperature (RT) in 5% CO_2. 75uL of warm serum-free RPMI-1640 media was added to rehydrate plates for 2 hours). 15,000 cells were plated per chamber in fresh serum-free media with 4 replicates per gene (n = 4). Complete media (10% fetal bovine serum (FBS) + RPMI-1640) was added to the lower basal chamber. Invasion plates were incubated for 28 hours at 37℃ in 5% CO_2. Chambers were washed twice with deionized water and stained with Calcein AM for 1 hour. Following this, fluorescence was counted on a Victor II plate reader.

2.1.2 *In vitro* screen data analysis

Readings were taken for 230 genes across 12 pools, each in quadruplicates. We used two different methods of statistical analysis to identify hits in order to reduce statistical variation. Using the replicates, the average raw reading was calculated for each gene excluding the outliers to establish the approximate expression level for the genes without the impact of technical fluctuations. The genes were then scored based on their statistical deviation in the relative expression, compared to mCherry control in each group. To do this, first, fold change was calculated as the ratio of each gene's average reading to the average mCherry reading from the same group. Statistical variation in fold change was then obtained by determining the standard deviation (SD) of fold change across all genes, across all groups (5.89). To determine whether a gene's fold change was significant for the degree of statistical fluctuation in fold changes across all cohorts, each gene's fold change versus mCherry was converted into the number of standard deviations (method 1). To do this, first, for each pool, the standard deviation fold change across all pools (5.89) was converted to a raw reading

basis by multiplying the standard deviation by each pool's average mCherry reading. This established 'normalized,' pool-specific standard deviation values reflective of statistical fluctuations in fold change across all pools. Second, the number of standard deviations was calculated for each gene as the ratio of the difference between the average reading for the gene and that of mCherry to the group-specific standard deviation. The number of standard deviations report the relative expression level of each gene versus an expression level equivalent to 1 standard deviation above the average expression over mCherry. To determine the final list of hits the number of standard deviations were used. It was observed that the distribution 2 of this metric generally followed a Gamma distribution, with most genes reporting a metric near 0 (170 out of 230) and showing positive skew. An approximate Gamma distribution was fit to the metric values for each gene with an Alpha value of 1.07 and a Beta value of 0.29. The final hit list was comprised of genes with a metric value in excess of the 90th percentile of the fit Gamma distribution (0.70). Furthermore, to limit statistical variation and false positive hits, the results from the screen were simultaneously analyzed by another way (method 2). To do this, the SD of the gene as determined previously was compared to the SD of mCherry within its particular cohort as an alternative to comparing it to the SD of mCherry across all groups. The genes that showed fold change invasion higher than 3X SD of mCherry were established as invasion hits. We further validated those genes that were significant after applying methods 1 and 2.

2.2 Cell culture

For all cell culture work, cells were grown in complete media (10% FBS + RPMI-1640) at 37℃ in 5% CO_2 unless otherwise mentioned. Inducible cells were doxycycline

induced for 24 hours before experiments unless specified. Human lung cancer cell lines HCC827, H441, H157, H358, A549, H1299 cells were procured from the National Cancer Institute (MCI-H series) or the Hamon Center for Therapeutic Oncology Research, University of Texas Southwestern Medical Center (HCC series). NMuMG murine breast cancer cells were procured from ATCC. HEK-293 cells in DMEM Mouse KP cell lines were developed and maintained as described before. Cell lines were named based on mouse number and site of derivation (eg. 393P – primary tumor, 344SQ – subcutaneous metastatic lesion). Cell lines were generated and characterized in our lab and mycoplasma tested (Gibbons, Lin, Creighton, Rizvi, et al., 2009).

2.2.1 Generating cell lines

Human Impad1 and Kdelr2 cDNA were individually cloned into pLD6EF vector by Gateway Cloning for constitutive and stable expression of the gene, for the screen. For inducible expression of human Impad1 or mouse Kdelr2 (ORIGENE #MR202320), they were individually sub-cloned into the pTRIPZ vector using the cut sites EcoRI-XhoI. For lentivirus transduction, plasmids were transfected into HEK-293 cells with the viral envelope (MD2G – Addgene #12259) and packaging (psPAX2 – Addgene #12260) plasmids. Transfections were performed by using Lipofectamine 3000 as per manufacturer protocol (Life Technologies, #L3000008). Virus was collected and filtered through 0.45 μM sterile filters every 24 hours until 72 hours post-transfection. All parental cells (393P, 344SQ, 344LN, 344P, HCC827) were incubated with 2 rounds of fresh virus and Polybrene (1 μM; Millipore, #TR1003-G). Cells were selected with

puromycin for stable overexpression of genes; cloning and sequencing primers, and puromycin concentration used as follows.

Gene	Sequence	Purpose	Species
Impad1 Forward	TATATATAGAATTCATGGCCCCCATGGGCATCCG	Cloning	Murine
Impad1 Reverse	CTATATATATAGAGCTCTCACTTATCGTCGTCATC CTTGTAATCATGTCCTGACTTTTCTAAATCCGG	Cloning	Murine
Impad1-1 Forward	TATATATAACCGGTATGGCCCCCATGGGCATCCG	Cloning	Murine
Impad1-1 Reverse	CTATATATATAACGCGTTCACTTATCGTCGTCATC CTTGTAATCATGTCCTGACTTTTCTAAATCCGG	Cloning	Murine
Impad1 Forward	TATATATAGAATTCATGGCCCCCATGGGCATCCG	Cloning	Human
Impad1 Reverse	CTATATATATACTCGAGTCACTTATCGTCGTCATC CTTGTAATCATTTATGTCCTGTCTTTTCTAGATC	Cloning	Human
Impad1 Forward	ATGTGGATGCCTCTGACAAG	Seq	Murine
Impad1 Reverse	CTTCTCATTGTAGGAAGAACGG	Seq	Murine
Impad1 Forward	GAACACGTGGATGCAGCTGAT	Seq	Human
Impad1 Reverse	CATTGTAGGAAGAGCGGGCTT	Seq	Human
Kdelr2 Forward	GTATTGCGAATTCATGAACATCTTCCGGCT	Cloning	Murine
Kdelr2 Reverse	TACAGCGTCGACTTAAACCTTATCGTCGTC	Cloning	Murine

Table 2-1. List of primers used for cloning and sequencing.

Cell Line	Puromycin Concentration
393P	4 μM
344SQ	10 μM
344P	5 μM
344LN	4 μM
HCC827	1 μM

Table 2-2. Concentration of Puromycin used to select cells.

2.2.2 RNA interference

The TRC Lentiviral pLKO.1 plasmid expressing scrambled control shRNA or murine Impad1 shRNA (SH1-TRCN0000173584, SH2-TRCN0000174471, SH3-TRCN0000175469) or Kdelr2 shRNA (shA- TRCN0000093585, shB-TRCN0000093586, shC-TRCN0000093588) were from GE-Dharmacon (now Horizon Discovery). 344SQ, 344P, 344LN cells were virally infected and stably selected as described before.

siRNA transfection was performed with RNAiMAX Lipofectamine (Life Technologies, #13778) as per manufacturer protocol. For mouse Syt11, siRNA pool (Dharmacon, #SO-2959152G) transfection was performed for ~40 hours at a final concentration of 30nM in 393P cells. In 344SQ cells, two rounds of siSyt11 transfections were carried out for ~72 hours at a final concentration of 30nM. For mouse Arf5, siRNA pool (Dharmacon, #SO-2952843G) transfection was performed for ~40 hours at a final concentration of 50nM in 393P cells. Non-targeting pool was used as negative control (Dharmacon, #SO-2968428G). siRNA sequences as follows.

Gene	Sequence	Purpose	Species
Impad1 SH1	ATTCCCTAGCATATTCCAGGC	shRNA	Murine
Impad1 SH2	TTACATACTGTTAAGTACGGG	shRNA	Murine
Impad1 SH3	TTCTCATTGTAGGAAGAACGG	shRNA	Murine
Kdelr2 shA	TATCGTGATTTCCATCATAGG	shRNA	Murine
Kdelr2 shB	ATCTTCAGCAGTAGGATGACG	shRNA	Murine
Kdelr2 shC	TTTCATGTAGATCAGGTACAC	shRNA	Murine
Syt11-1	GCACAGUCUGAGCGAGUAC	siRNA	Murine
Syt11-2	AUGUCAAGGUGAACGUCUA	siRNA	Murine
Syt11-3	GAGAGAGGUCUGCGAGAGU	siRNA	Murine
Syt11-4	CGAUCGCACUACUAAGAAU	siRNA	Murine
Arf5-1	AUGCCAUGCCCGUGAGCGA	siRNA	Murine
Arf5-2	UCUUUGUGGUAGACAGCAA	siRNA	Murine

Arf5-3	GAGCAGGGAUCUGGAUUUA	siRNA	Murine
Arf5-4	AGAUGCUGCAGGAGGAUGA	siRNA	Murine

Table 2-3. List of shRNAs and siRNAs used to knockdown respective genes.

2.3 Proliferation assay

Cells were seeded at 750 cells/well in 96-well plates. Proliferation was quantified using the MTT (Sigma, #M5655-1G) protocol and absorbance was measured at 570 nm with background measured at 630 nm after 2 hours.

2.4 *In vitro* invasion experiments

All inducible cells were induced with 2μM doxycycline for 24 hours unless specified. N = 3 unless mentioned. Data are represented as mean$\pm$SD and significance by Student's *t* test. Variance is unequal and hence I use parametric *t*-test. *p < 0.05; **p < 0.002.

2.4.1 2D migration and invasion assays

50,000 cells/well were resuspended in serum-free RPMI-1640 and plated in the 24-well Transwell (8 μM inserts, Corning Star) migration or Boyden chamber (BD-Biosciences, #354480) invasion wells. Doxycycline induction was continued for inducible cells. Complete media was added to the lower chamber and cells were incubated at 37℃ in 5% CO_2 for 16 hours. Inserts were stained with 0.1% crystal violet and non-migrating/non-invading cells were cleaned with cotton swabs. Cells that migrated or invaded were imaged in five fields at 10X magnification. An imageJ macro was used to quantify the number of cells and results were represented as previously described. Data was plotted as number of cells migrated or invaded.

2.4.2 Wound healing assay

Induced cells were grown to confluency in 6-well plates. Once confluent, a single scratch was made on the cell monolayer by using a 200 μl tip (Martinotti & Ranzato, 2020). Cells were washed twice with 1X PBS, incubated with 1μM Mitomycin C for 4 hours, and washed again with 1X PBS. Doxycycline induction was continued for inducible cells. Two representative images were taken at 10X magnification at 0 hours and after 24-hour incubation with complete media. Images were taken with the inverted microscope (Leica Microsystems, Germany). Percentage of wound healing was determined by comparing area healed between 0 hours and 24 hours by experimental cells compared to control cells. N = 3 images/well and 2 wells/sample.

2.4.3 3D invasion assay

1,500 cells/well were plated in 8-well chambered slides in a matrix comprising of 1.5 mg/ml collagen/Matrigel (BD-Biosciences #354230 and #354236). Cells were replenished with complete media with 2% Matrigel every 2 days. For inducible cells, complete media with 2μM doxycycline and 2% matrigel was added every day. Spheroids with protrusions were imaged every 2 days with an inverted microscope, and quantified and plotted as %invasive structures. All structures that reached a pre-determined size were included in the quantifications.

2.4.4 Secretome-mediated Invasion assays

To measure Golgi secretion – 1x10^6 cells were plated in 60 mm tissue culture dishes after 24-hour doxycycline induction. Conditioned media (CM) was collected from the confluent cells after 24 hours, where cells were either treated with DMSO or 1 μM Brefeldin-A (Golgi plug; BD Biosciences, #51-2301-KZ) for the last 6 hours. CM

was then filtered through 0.45 uM sterile filters. 50,000 cells/well of 393P WT parental cells were suspended in this CM and plated in invasion Boyden chambers. RPMI-1640 with 20% FBS was added to the lower wells and cells were incubated at 37℃ in 5% CO_2 for 16 hours. Invaded cells were then stained, imaged, and quantified as mentioned in section 2.4.1.

To measure MMP secretion – $1x10^6$ cells were plated in 60 mm tissue culture dishes after 24-hour doxycycline induction. CM was collected from the confluent cells after 24 hours and filtered through 0.45 µM sterile filters. 50,000 cells/well of 393P WT parental cells were suspended in the CM treated with DMSO or 1 μM Ilomastat (Sellekchem, #S7157) and plated in invasion Boyden chambers. RPMI-1640 with 20% FBS was added to the lower wells and cells were incubated at 37℃ in 5% CO_2 for 16 hours. Invaded cells were then stained, imaged, and quantified as mentioned in section 2.4.1.

Upon Syt11 transient knockdown – Syt11 siRNA (30nM) knockdown was done in 6-well plates. Cells were then induced with doxycycline for 24 hours and conditioned media was collected from siControl or siSyt11 cells. Invasion assay was performed as described above.

2.5 *In vivo* metastasis experiments

All experiments were reviewed and approved by the Institutional Animal Care and Use Committee at The University of Texas M.D. Anderson Cancer Center. Cells were implanted subcutaneously (SQ) into the flank of syngeneic 129/Sv male and female mice and tumor growth was monitored manually twice a week for 6–8 weeks. Once the tumors reached a volume of 1500 mm^3, mice were euthanized with CO_2 and

macroscopic metastatic nodules on the lung surface were manually quantified. Mice injected with doxycycline-inducible cells were fed 625mg/kg of doxycycline feed (Envigo, #Rx-3204076) starting 48 hours after implantation. Lung and tumor tissues were fixed in 10% Formalin and then proceeded for sectioning and H&E staining. SQ tumors were also snap-frozen in liquid nitrogen to collect RNA and protein. Power analysis for determining sample size was done using 80% power and 5% two-sided type 1 error. Multiple comparisons ANOVA test was done for tumor growth over time curves to obtain significance for each time point. No randomization or blinding was performed as only the phenotypic testing of genes was done in syngeneic mice.

Mouse from 344SQ GFP cohort **(Figure 3-4Figure 3-6)** was excluded based on PRISM outlier statistics. Mice that had no tumor growth from 393P GFP and Impad1 cohorts **(Figure 3-4)** were excluded.

2.6 Immunohistochemistry (IHC)

Formalin-fixed, paraffin-embedded tissues were cut into 4µm sections. The sections were de-thawed in Xylene and rehydrated in sequentially diluted ethanol baths. Citric acid (s1399, Dako, USA) was used for antigen retrieval and 3% H_2O_2 was used to block endogenous peroxidase activity. Sections were then blocked with 5% goat serum for 1 hour, incubated O/N at 4ºC with primary antibody and 1 hour at RT with biotin-conjugated secondary antibody. Immunohistochemistry was carried out using Streptavidin (Life technologies #SNN1004), Envision+ System (Dako), and HRP-DAB (Dako) colorimetric detection. Antibody details as follows.

Target	Dilution	Vendor	Cat#	Host Species
Impad1	1 to 70	R&D Systems	AF7028	Sheep
Flag	1 to 1000	Abcam	21536	Rabbit

Kdelr2	1 to 750	Invitrogen	PA5-75397	Rabbit
Zeb1	1 to 200	Genetex	GTX105278	Rabbit
E-cadherin	1 to 300	CST	3195	Rabbit
Anti-rabbit	1 to 300	Dako	E0353	Secondary
Anti-sheep	1 to 150	Abcam	ab6746	Secondary

Table 2-4. List of antibodies used for IHC.

2.7 Quantitative reverse-transcriptase PCR (qRT-PCR)

For mRNA – Cells were lysed in TRIzol (Ambion) and RNA was isolated by using the Direct-zol RNA miniprep plus kit (Zymo #R2072). Complementary DNA (cDNA) was obtained by RT-PCR with 2ng/μL RNA and qScriptTM (030497, Quanta Bio). qPCR was performed on a 7500 Fast Real-Time PCR System (Applied Biosystems) with SYBR® Green PCR Master Mix (Life technologies). L32, the ribosomal housekeeping gene was used as the internal control. Data analysis was done on the 7500 Software v2.0.5 (Applied Biosystems). Primers specified below.

For microRNA (miRNA) – miRNA quantification assays were performed by using the TaqMan miR as per manufacturer protocol (Applied Biosystems). miR-16 was used as a reference control due to its stable endogenous expression.

For tumor RNA – Frozen tumors sections were homogenized. mRNA was extracted by using the mirVana mRNA kit as per manufacturer protocol (ThermoFisher, #AM1561).

Gene	Sequence	Purpose	Species
Impad1-F	CCGCAAGATGTTCTACCTGCTC	qPCR	Murine
Impad1-R	GGATGTCCTCAGGAATCTTCCG	qPCR	Murine
Kdelr2-F	CGATACCTTCCGAGTGGAGTTC	qPCR	Murine
Kdelr2-R	CCAGGTAGATGGAGAAGGTCCA	qPCR	Murine
Zeb1-F	ATGCTCTGAACGCGCAGC	qPCR	Murine
Zeb1-R	AATCGGCGATCTTTGAGAGCT	qPCR	Murine
E-cadherin-F	GGTCATCAGTGTGCTCACCTCT	qPCR	Murine
E-cadherin-R	GCTGTTGTGCTCAAGCCTTCAC	qPCR	Murine

Vimentin-F	CGGAAAGTGGAATCCTTGCAGG	qPCR	Murine
Vimentin-R	AGCAGTGAGGTCAGGCTTGGAA	qPCR	Murine
Syt11-F	CAATGCGTTTTCTGCCGTAGTAGA	qPCR	Murine
Syt11-R	CTGACCAGGGACATCATCAAGAG	qPCR	Murine
Impad1-F	AATGTGAAAGCCCGCTCTTC	qPCR	Human
Impad1-R	TGAAGAGCGACCTGTTTGAC	qPCR	Human
Kdelr2-F	ACCTTCCGAGTGGAGTTTCTGG	qPCR	Human
Kdelr2-R	ATAGCCACGGACTCCAGGTAGA	qPCR	Human
ZEB1-F	GGCATACACCTACTCAACTACGG	qPCR	Human
ZEB1-R	TGGGCGGTGTAGAATCAGAGTC	qPCR	Human
E-CADHERIN-F	GCCTCCTGAAAAGAGAGTGGAAG	qPCR	Human
E-CADHERIN-R	TGGCAGTGTCTCTCCAAATCCG	qPCR	Human
SYT11-F	GTGGTCCTCAAAGCCAGACACT	qPCR	Human
SYT11-R	GCAATGCGCTTTCTGCCGTAGT	qPCR	Human
5' miR200-Pr-2468-2630	GGAGCAATCGGTAGATTGTTG	Taqman	Hu/Ms
3' miR200-Pr-2468-2631	CACACTAAGAACATCCTGGC	Taqman	Hu/Ms

Table 2-5. List of primers for qPCR.

2.8 Immunoblotting

Cells and tumor tissues were lysed in RIPA buffer (Cell Signaling Technologies, USA). Protein lysates were run on 10% Bis-Acrylamide gels and transferred to nitrocellulose or PVDF membranes. 5% milk in TBST (10 mM Tris, 100 mM NaCl, and 0.1% Tween 20) was used as blocking buffer. Blocking was for 1 hour at RT, primary antibodies were incubated O/N at 4ºC, and secondary antibodies were incubated for 1 hour and RT in 2.5% milk/TBS-T. Blots were finally visualized using an ECL detection system (LF-Q0101, 27B09). β-actin was used as loading control. Densitometric analysis on blots for quantifying MMP levels were performed using ImageJ. Antibody details as follows.

Target	Dilution	Vendor	Cat#	Host Species
Impad1	1 to 1000	Abcam	ab69311	Mouse
Impad1	1 to 1000	R&D Systems	AF7028	Sheep
Kdelr2	1 to 500	Abcam	ab199689	Rabbit
GFP	1 to 1000	Abcam	ab290	Rabbit

Zeb1	1 to 500	Genetex	GTX105278	Rabbit
E-cadherin	1 to 1000	BD Transduction	610182	Mouse
Golgin97	1 to 1000	CST	13192	Rabbit
GM130	1 to 1000	CST	12480	Rabbit
Syt11	1 to 1000	Thermofisher	PA5-96970	Rabbit
Arf5	1 to 500	Proteintech	20227-1-AP	Rabbit
MMP-1	1 to 1000	Genetex	GTX100534	Rabbit
MMP-2	1 to 1000	CST	87809	Rabbit
MMP-9	1 to 1000	Invitrogen	MA5-32705	Rabbit
Integrin-α6	1 to 1000	CST	3750	Rabbit
β-Actin	1 to 10000	Proteintech	66009-1	Mouse
Anti-mouse	1 to 2000	CST	7076	Secondary
Anti-rabbit	1 to 2000	CST	7074	Secondary
Anti-sheep	1 to 2000	Abcam	ab6900	Secondary

Table 2-6. List of antibodies used for immunoblotting.

2.9 Cell fractionation

Cell fractionation was performed using a kit as per the manufacturer's protocol (Cell signaling technologies, #9038S). Fractions were analyzed by western blotting. α-tubulin – cytoplasmic fraction control, Integrinα6 – membrane fraction control, LaminA/C – nuclear fraction control. Antibody details as follows.

Target	Dilution	Vendor	Cat#	Host Species
α-Tubulin	1 to 1000	CST	2125	Rabbit
Integrinα6	1 to 1000	CST	3750	Rabbit
LaminA/C	1 to 1000	CST	2032	Rabbit

Table 2-7. List of antibodies used as fraction controls for cell fractionation assays.

2.10 Immunoprecipitation-mass spectrometry (IP-MS)

Cells were grown on 15-cm plates and induced with doxycycline for 48 hours. Agarose beads (Santa Cruz, #sc2003) were conjugated with anti-mouse IgG antibody (Santa Cruz, #sc2025) O/N at 4ºC. NET-N (125mM NaCl, 50mM Tris-Hcl pH 8.0, 0.5% NP-40) buffer was used to lyse the cells and lysate was pre-cleared with agarose beads (IgG antibody for 1 hr at 4ºC then beads for 30 mins at 4ºC). For Flag IP, lysate

was incubated with flag-tagged beads (Biotool, #B23101) for 2 hrs at 4ºC. Beads were then washed with 1X TBS (as per protocol) and sent for mass spectrometry analysis to the proteomics core at UTMB. Samples were prepared in 5% SDS, 50mM TEAB, pH =7.5. The agarose beads were incubated for 30minutes at 37ºC, after which the supernatant was processed as described in the LC/MS section below (Section 2.11).

2.10.1 Co-immunoprecipitation

Cells were grown, lysed, and pre-cleared as described above. Anti-rabbit Igg (Cell Signaling Technology, #2729) and anti-Syt11 or anti-Arf5 antibodies were conjugated to agarose beads. For IP, lysate was incubated with IgG, or Syt11-conjugated beads for 3 hrs at 4ºC. Beads were washed with NET-N buffer and lysate prepared for western blot. Antibody details as follows.

Target	Dilution	Experiment	Vendor	Cat#	Host Species
Syt11	2 µg	IP	Thermofisher	PA5-96970	Rabbit

Table 2-8. Antibody used for co-IP

2.11 Liquid chromatography-mass spectrometry (LC-MS)

Cells were grown in 15-cm plates in serum-free media and incubated with doxycycline for 48 hrs. Conditioned media was filtered and concentrated (Millipore Amicon, Cat# UFC901024) and sent for mass spectrometry analysis to proteomics core at UTMB. Samples were made with 5% SDS, 50 mM TEAB, pH 7.55, then reduced in 20 mM TCEP solution (Thermo Fisher Scientific, #77720) at 65°C for 30 minutes. The sample was treated with 0.5 M iodoacetamide acid at RT for 20 minutes. Next, 12% phosphoric acid was added to the solution, followed by binding buffer (90% methanol, 100 mM TEAB, final pH 7.1). The solution was spun using S-Trap spin columns (protifi.com) at 4,000xg for 30s, then washed with binding buffer (90%

methanol, 100mM TEAB, pH = 7.55) and treated with Trypsin (50 mM TEAB, pH 8) at 37°C for 4 hours. Peptides were eluted with 50 mM TEAB, followed by 0.2% formic acid, and finally 50% acetonitrile, 0.2% formic acid. The solution was then dried in a speed vac and resuspended in 2% acetonitrile, 0.1% formic acid, 97.9% water.

Nano LC MS/MS Analysis: Peptide mixtures were analyzed by nanoflow liquid chromatography-tandem mass spectrometry (nano LC-MS/MS) using a nano-LC chromatography system (UltiMate 3000 RSLCnano, Dionex), coupled on-line to a Thermo Orbitrap Eclipse mass spectrometer (Thermo Fisher Scientific, San Jose, CA) through a nanospray ion source coupled with a FAIMS Pro device (Thermo Fisher Scientific) with Instrument Control Software version 3.4. FAIMS separations were performed at Standard Resolution with the following settings: inner and outer electrode temperature = 100 °C; FAIMS gas flow = 0 L/min, Compensation Voltages (CV): -45, -60 and -70 with 2 second cycle times per CV. A trap-and-elute method was used: The trap column is a C18 PepMap100 (300um X 5mm, 5um particle size) from ThermoScientific. The analytical column is an Aurora (75um X 25 cm, 1.6 µm) from (Ionopticks). After equilibrating the column in 98% solvent A (0.1% formic acid in water) and 2% solvent B (0.1% formic acid in acetonitrile (ACN)), the samples (2 µL in solvent A) were injected onto the trap column and subsequently eluted (400 nL/min) by gradient elution onto the C18 column as follows: isocratic at 2% B, 0-5 min; 2% to 4% 5-6 min, 4% to 25% B, 6-70 min; 25% to 38% B, 70-97 min; 38% to 90% B, 97-100 min; isocratic at 90% B, 101-102 min; 90% to 5%, 102.5-103 min; 5% 102.5-103min; 90%-5% 104-105 min; and isocratic at 2% B, till 120 min.

Database Searching: Tandem mass spectra were extracted and charge state deconvoluted by Proteome Discoverer (Thermo Fisher, version 2.5). Deisotoping is not performed. All MS/MS spectra were searched against a Uniprot Mus Musculus and common contaminant database (version 03-29-2016) using Sequest. Searches were performed with a parent ion tolerance of 5 ppm and a fragment ion tolerance of 0.60 Da. Trypsin is specified as the enzyme, allowing for two missed cleavages. Fixed modification of carbamidomethyl (C) and variable modifications of oxidation (M) and deamidation were specified in Sequest.

2.12 3'-UTR Luciferase reporter assay

3'UTR Impad1 was PCR-amplified from the 344SQ WT genomic DNA and cloned downstream of Firefly Luciferin gene in the pMirGLO plasmid with the restriction sites XhoI-Sbf1. The Renilla Luciferin gene in the pMirGLO plasmid was used as an internal control. The QuikChange Lightning MULTI Site-Directed Mutagenesis Kit (Agilent, Santa Clara, CA, USA) was used to make mutations in the miR-200 or miR~96/183 binding sites in Impad1 3' UTR. 393P WT cells were plated in 24-well plates the previous day so that they were ~60% confluent at time of transfection. For 3' UTR luciferase reporter assays, cells were co-transfected with 1μg pMirGLO plasmid (Promega, # E1330) and 60 pmol miR-200a/b/c or miR-96/183 mimics (Ambion by Life Technologies, #4464066). Negative mimics were used as the negative control. Transfection was performed by using Lipofectamine 2000 (Life Technologies, #11668019). Assays were carried out as per manufacturer instructions with Dual-Luciferase Reporter Assay kit (Promega, #1910). Relative luciferin signal

was normalized to signal from the negative mimic controls. Primers used to clone and sequence Impad1 3'UTR, and miRNA mimic sequence as follows.

Gene	Sequence	Purpose	Species
F-UTRIMP-XhoI	TAGGTGTACTCGAGTCACTGTAACATGTCAACGC	Cloning	Murine
R-UTRIMP-SbfI	TTATACCTGCAGGCACAACGCCCTATGTAAGGC	Cloning	Murine
SDM_miR96/183-F	GTAACTCAGGCAGAAGTACAGTCAAGGTCAAACCATTTTAACTTTCTTGATCATAG	Cloning	Murine
SDM_miR96/183-R	CTATGATCAAGAAAGTTAAAATGGTTTGACCTTGACTGTACTTCTGCCTGAGTTAC	Cloning	Murine
SDM_miR200b/c/429-F	TTTGTTTCAAAGCCAATATACATTACAAGGAAAACAACGGTTATTTATATGAGGTATTATTGTGCCAGAACATATC	Cloning	Murine
SDM_miR200b/c/429-R	GATATGTTCTGGCACAATAATACCTCATATAAATAACCGTTGTTTTCCTTGTAATGTATATTGGCTTTGAAACAAA	Cloning	Murine
UTRIMP Seq-F1	AAAGATGCTGGCTGAGAGGT	Seq	Murine
UTRIMP seq-F2	AGAAATAGGTAGGGCCAAGG	Seq	Murine
UTRIMP seq-F3	TGCCTAAAGGACTGACCGGC	Seq	Murine
UTRIMP Seq-R1	TAAAACAATTTAACATTAAT	Seq	Murine
UTRIMP Seq-R2	GTTCATTTGCTTGCAGCGAG	Seq	Murine
miR-200a-3p	UAACACUGUCUGGUAACGAUGU	miRNA	Murine
miR-200b-3p	UAAUACUGCCUGGUAAUGAUGA	miRNA	Murine
miR-200c-3p	UAAUACUGCCGGGUAAUGAUGGA	miRNA	Murine
miR-96-5p	UUUGGCACUAGCACAUUUUUGCU	miRNA	Murine
miR-183-5p	UAUGGCACUGGUAGAAUUCACU	miRNA	Murine

Table 2-9. List of primers used for 3'UTR luciferase assay. *Primers used to clone and sequence the Impad1 3'UTR into pMirGLO plasmid. Sequence of miRNA mimics used to repress luciferase activity.*

2.13 Immunofluorescence

Cells were plated on 8-well glass slides treated with Poly-L-Lysine and fixed in 4% paraformaldehyde with 50 μM $CaCl_2$/PBS for 20 min at 37℃. Permeabilization was done with 0.1% Triton X-100/PBS for 10 min at RT. Cells were then blocked with 5% goat serum/PBS for 1 h at RT and then incubated with primary antibody detailed below. Next, cells were washed with 1X PBS and subsequently incubated with fluorophore-conjugated secondary antibodies detailed below. Finally, cells were counterstained with DAPI by mounting with VECTASHIELD Hard-Set Mounting Medium (Vector Laboratories, Burlingame, CA) and imaged by confocal microscopy.

For Impad1 and GM130 BFA treatment – Cells were incubated with human Impad1 primary antibody O/N at 4℃, and then sequentially incubated with fluorophore-conjugated secondary antibodies. First, Alexa 546-conjugated anti-mouse and then GM130. 1 μM BFA treatment for 4 hours at 37℃.

For Impad1 and Golgin97 – Experiment was done as described above. Primary antibodies used were human Impad1 and mouse Golgin97 O/N at 4ºC. Fluorophore-conjugated secondary antibodies Alexa 546-conjugated anti-mouse and Alexia 488-conjugated anti-rabbit were incubated for 1 hour at RT.

For Kdelr2 and Calnexin or GM130 staining – Cells were grown as described above. They were fixed in 4% paraformaldehyde in +Mg +Ca PBS (Corning #21-030-CV) for 10 min at RT, and permeabilized with 0.1% Triton X-100/PBS for 5 min at RT. Cells were then blocked with 2% goat serum + 2% BSA/PBS for 1.5 h at RT and incubated with primary antibody for FLAG for 1 h at RT. Cells were sequentially incubated with fluorophore-conjugated secondary antibodies. First, anti-mouse and

then for Calnexin or GM130. Each of the secondary antibodies were incubated for 1.5 h at RT and then counterstained and imaged as mentioned above. BFA treatment as mentioned above.

Target	Dilution	Vendor	Cat#	Host Species
Impad1	1 to 100	Abcam	ab69311	Mouse
Golgin97	1 to 1000	CST	13192	Rabbit
GM130	1 to 50	BD Pharminogen	56027	Mouse
Flag	1 to 1000	Sigma	F1804	Mouse
Calnexin	1 to 100	Invitrogen	MA3-027-A488	Rabbit
Alexa 546 anti-mouse	1 to 200	Thermofisher	A11030	Secondary
Alexa 488 anti-rabbit	1 to 200	Thermofisher	A11008	Secondary
Alexa 635 anti-rabbit	1 to 200	Thermofisher	A31576	Secondary

Table 2-10. List of antibodies used for immunofluorescence.

2.13.1 Confocal microscopy and analysis

For quantifying Golgi area – All analyses were done by using ImageJ, following the previously described protocol (Tan et al., 2017). Briefly, GM130-stained Golgi was quantified in volume projections with a limiting polygon. Golgi area was normalized by dividing by the nucleus area in the same cell (N=50 cells). Cells with a well-defined Golgi and nucleus were selected randomly for quantification.

For quantifying Golgi fragment size and number – Golgi fragment size and number were determined from maximum intensity projections of deconvolved, threshold (Otsu), and watershed-segmented 3D stacks (N=75 cells).

2.14 VSV-G transport assay

Followed previously described protocol (Tan et al., 2017). The EGFP-VSV-G (ts045) plasmid (Addgene 11912) was a gift from Dr. Jonathan Kurie (UT MD Anderson Cancer Center, Houston, Texas, USA). EGFP-VSV-G (ts045) was transiently transfected into cells using JetPRIME transfection reagent (Polyplus, #114-

07), which were then induced with doxycycline for 24 hrs. Cells were then transferred to a restrictive temperature of 40°C for 20 hours. They were then treated with cycloheximide (1 μM) and transferred to a permissive temperature of 32°C for 1 hr. Cells were then fixed with formaldehyde (Invitrogen, #FB002) at 32°C for 10 mins, blocked with 2% BSA/PBS, the exofacial VSV-G stained with anti–VSV-G primary antibody for 1 hr at RT, and stained with anti-mouse secondary antibody for 1 hr at RT. Cells were counterstained with DAPI by mounting with VECTASHIELD Hard-Set Mounting Medium (Vector Laboratories, Burlingame, CA) and imaged by confocal microscopy. Fluorescence intensity was quantified for exofacial (red) and total VSV-G (green), and that ratio was plotted. A total of 20 images per group were smoothed using a median filter and thresholded (Otsu). Pixel-by-pixel ratio images were generated using the following equation: (intA – bkgA)/(intB – bkgB) × MF, where intR, intA, and intB are the intensities of the ratio image, first-channel images, and second-channel images, respectively, bkgA and bkgB are the background values of the corresponding images, and MF is an arbitrary multiplication factor. Pseudocolored images were generated by a custom gradient lookup table. For visualization purposes, the pseudocolored images were intensity-calibrated. Antibody details as follows.

For VSV-G assay with siSyt11, transfection for both Syt11 siRNA (RNAiMAX) and VSV-G (JetPRIME) were done simultaneously. Assay was then performed as mentioned above.

Target	Dilution	Experiment	Vendor	Cat#
VSV-G	1 to 100	VSV-G/IF	Kerafast	EB0012
Alexa 568 anti-mouse	1 to 1000	VSV-G/IF	Thermofisher Scientific	A10037

Table 2-11. List of antibodies used for VSV-G assay.

2.15 Detecting ECM components

2.15.1 Masson's trichrome staining

Subcutaneous (SQ) tumor tissues that were stained for collagen as per manufacturer's protocol (Sigma-Aldrich, #HT15). Tissues were imaged at 20X magnification with 5 representative images per tumor. Quantification was by ImageJ analysis.

2.15.2 Second Harmonic Generation (SHG) microscopy

SQ tumor tissues that were stained by H&E were detected using a Zeiss LSM 7 MP Multiphoton Microscope at an excitation wavelength of 800 nm and collagen fiber signals were visualized at 380-430 nm using bandpass filters.

2.15.3 Alcian blue staining

SQ tumors were stained for sulfated GAGs as per manufacturer's protocol (Abcam, #ab150662). Imaging and quantification were similar to Masson's trichrome staining.

2.16 Flow cytometry analysis

Flow cytometry staining, gating, and analysis were performed as previously described (David H. Peng et al., 2021). Briefly, subcutaneous tumors were first mechanically dissociated and then enzymatically digested using digestion media [RPMI-1640 containing 2 U/mL dispase II (Roche) and 0.5% w/v collagenase type I (Thermo Fisher)] at 37°C for 45 min. Tumor cell suspensions were then filtered through a 70 μm Falcon Nylon cell strainer (Fisher Scientific). Like tumors, spleens were mechanically dissociated but filtered through a 40 μm Falcon Nylon cell strainer.

Cells were centrifuged at 800xg for 5 mins and resuspended in RBC lysis buffer (Biolegend) for 2 min at RT, after which lysis was inhibited using complete media. Cells were finally centrifuged and resuspended in FACS buffer (PBS + 2% FBS + 1 mM EDTA). 2×10^6 cells per sample were stained with fluorescently-labeled antibodies. For intracellular staining, cells were fixed in 1% PFA and permeabilized in permeabilization buffer (BD Biosciences) for 30 mins at RT. Cells were then stained with respective fluorescently-labeled antibodies. FlowJo 10.8.1 was used to analyze FACS. Antibody details as follows.

Target	Dilution	Vendor	Cat#
CD8 PE-Cy7 (53-6.7)	1 to 800	BioLegend	100721
CD3 PE-594 (17A2)	1 to 100	BioLegend	100246
CD62L FITC (MEL-14)	1 to 100	Tonbo	35-0621-U500
CD274 PE-594 (10F.9G2)	1 to 100	BioLegend	124323
CD44 APC (IM7)	1 to 100	BioLegend	103012
CD4 APC-Cy7 (RM4-5)	1 to 100	BioLegend	100526
FoxP3 PerCp-Cy5.5 (FJK-16s)	1 to 100	eBioscience	45-5773-82
CD86 APC-Cy7 (GL-1)	1 to 100	BioLegend	105030
CD68 PerCp-Cy5.5 (FA-11)	1 to 100	BioLegend	137009
CD69 BV650 (H1.2F3)	1 to 100	BioLegend	104541
CD45 Pacific Blue (30-F11)	1 to 100	BioLegend	103126
CD45 PerCp-Cy5.5	1 to 100	BioLegend	103132
CD25 BUV395 (PC61)	1 to 100	BD Biosciences	564022
CD11c BV786 (N418)	1 to 100	BioLegend	117335
CD44 BV711 (IM7)	1 to 100	BioLegend	103057
GR1 BV711 (RB6-8C5)	1 to 100	BioLegend	108443
CD278 PE (7E.17G9)	1 to 100	BioLegend	117406
CD278 BV785 (C398.4A)	1 to 100	BioLegend	313533
TIM3 APC (B8.2c12)	1 to 100	BioLegend	134007
PD1 BV605 (29F.1A12)	1 to 100	BioLegend	135220
PD-1 FITC(29F.1A12)	1 to 100	BioLegend	135214
F4/80 APC (BM8.1)	1 to 100	Tonbo	20-4801-U100
MHC II/PE-Cy (M5/114.15.2)	1 to 100	BioLegend	107629
CD11b BV650 (M1170)	1 to 100	BioLegend	101239
CD206-FITC	1 to 100	BioLegend	141703
CD36-PE	1 to 100	BioLegend	102605

Table 2-12. List of antibodies used for flow cytometry analysis

2.17 Analysis of human cancer datasets

Correlation with EMT. For mRNA correlation in NSCLC cell lines, published UTSW dataset was used (N=118) (McMillan et al., 2018). For mRNA correlation in LuAd tumors, TCGA Firehose legacy dataset was used (N=555 for dataset with mRNA only). EMT score was calculated using previously determined EMT signature (Byers et al., 2013). Correlations analysis were shown as Spearman's rank correlation with a p-value < 0.05.

miRNA correlations in NSCLC cell lines, Affymetrix microRNA 4.0 samples were processed by Affymetrix Expression Console (Kundu et al., 2016). For miRNA correlations in LuAd tumors, TCGA Firehose legacy dataset was used (N=414 for dataset with mRNA and miRNA). Correlations analysis were shown as Spearman's rank correlation with a p-value < 0.05.

Correlation of IMPAD1 and ZEB1 protein levels in lung cancer patient samples, IHC was performed on NSCLC whole sections with selected cases from a tissue microarray (TMA3) with ZEB1 expression. Protocol was followed as described in immunohistochemistry section except, antigen retrieval: pH-6, at 100℃ for 20 minutes, and primary antibody staining with IMPAD1 (1:200, Sigma, Cat# HPA009411). Signal was quantified using HALO (Indica Lab) software, and correlation analysis was shown as Spearman's rank correlation with a p-value < 0.05.

2.18 Statistics

Unless specified, all experiments were performed using technical triplicates. Data are represented as mean±SD and significance by Student's *t* test. Variance is unequal and hence I use a parametric *t*-test. *p < 0.05; **p < 0.002.

Chapter 3: High-throughput gain-of-function screen to identify novel drivers of lung cancer invasion and metastasis

Contents of this chapter including figures are derived from the publication Bajaj R, Kundu ST, Grzeskowiak CL, Fradette JJ, Scott KL, Creighton CJ, Gibbons DL. "Impad1 and Kdelr2 drive invasion and metastasis by enhancing Golgi-mediated secretion." *Oncogene*. 2020 Aug 04. PubMed PMID: 32753652 with approval from Nature Publishing Group.

3.1 Invasion screen

To study non-small cell lung cancer (NSCLC) metastasis in mice that recapitulate the disease phenotype of patients, we used the previously described *KRAS*^{G12D};*p53*$^{R172H\Delta G/+}$ (KP) mice, and the KP cell panel derived from them (Gibbons et al., 2014; Gibbons, Lin, Creighton, Rizvi, et al., 2009; Gibbons, Lin, Creighton, Zheng, et al., 2009). We mainly used the KP cell lines, 393P, which is representative of the non-invasive and non-metastatic characteristics, and 344SQ, which is invasive and metastatic. Transcriptomic profiles carried out on the Kras vs KP GEMMs, and the 393P vs 344SQ syngeneic tumors illuminated differential expression and phenotypic patterns between the metastatic and non-metastatic models. Thus, we hypothesized that there are genes in addition to the putative drivers, Kras and p53, that are responsible for driving the disease phenotype – lung cancer invasion and metastasis.

To identify the drivers of invasion and metastasis in NSCLC, we performed GOF *in vitro* and *in vivo* screens in conjunction. The 217 candidate genes for the screens were selected based on their increased expression in three independent datasets. First, in metastases compared to primary tumors in KP mice. Second, in syngeneic tumors formed by implantation of metastatic 344SQ cells compared to non-metastatic 393P cells, and third, in the human TCGA lung adenocarcinoma dataset with a 1.5-fold amplification in copy number (Grzeskowiak et al., 2018; S. T. Kundu et al., 2018). The *in vivo* screen yielded only the top metastasis drivers after a competitive selection pressure. Therefore, to identify additional drivers of invasion, independent of this *in vivo* selective pressure, we performed an *in vitro* invasion screen in parallel, by utilizing the same candidate genes **(Figure 3-1A)**. These cell lines were randomly grouped and were individually seeded in quadruplicates in 96-well invasion chambers. Cells that invaded were stained with calcein AM and the fluorescence quantified to determine their fold change invasion compared to mCherry within the respective groups (details in methods). To minimize variation, we analyzed the results in two different ways. First, we identified hits with a fold change invasion greater than 3X standard deviation (SD) of mCherry, across all the groups. To do this, we calculated fold change invasion for each gene compared to mCherry from the respective cohorts. We then calculated the SD of fold change values across genes from all groups. Finally, we identified the hits that had a fold change invasion significantly higher than 3X SD of mCherry across all groups (details in methods). The normalized invasion changes established the drivers of lung cancer invasion (p value < 0.05). Through this, we identified known oncogenes, such as SNAI2,

CCNE1, and MYC, and many potential novel drivers, including IMPAD1 and Kdelr2. IMPAD1 exhibited the highest invasive ability with a 32-fold increase in invasion, second to the positive control, SNAI2 (37-fold). Importantly, several of the hits were also identified as drivers of metastasis from the *in vivo* screen (TMEM106B and MBIP), demonstrating functional overlap between the two screening methodologies (Grzeskowiak et al., 2018; S. T. Kundu et al., 2018; Ochieng et al., 2020) **(Figure 3-1B)**. Additionally, we determined the top hits from each cohort by comparing the fold change invasion of the individual genes that were higher than 3X SD of the respective mCherry control within the same group. This avoided statistical variation across mCherry samples from different cohorts and ascertained the top hits within the respective groups (**Figure 3-10A-L**, details in methods). These hits were functionally validated by 2D migration and invasion, and 3D invasion assays where cells were plated in a collagen/Matrigel matrix and percent invasive structures were quantified based on organoids with invasive protrusions **(Figure 3-11A-F)**.

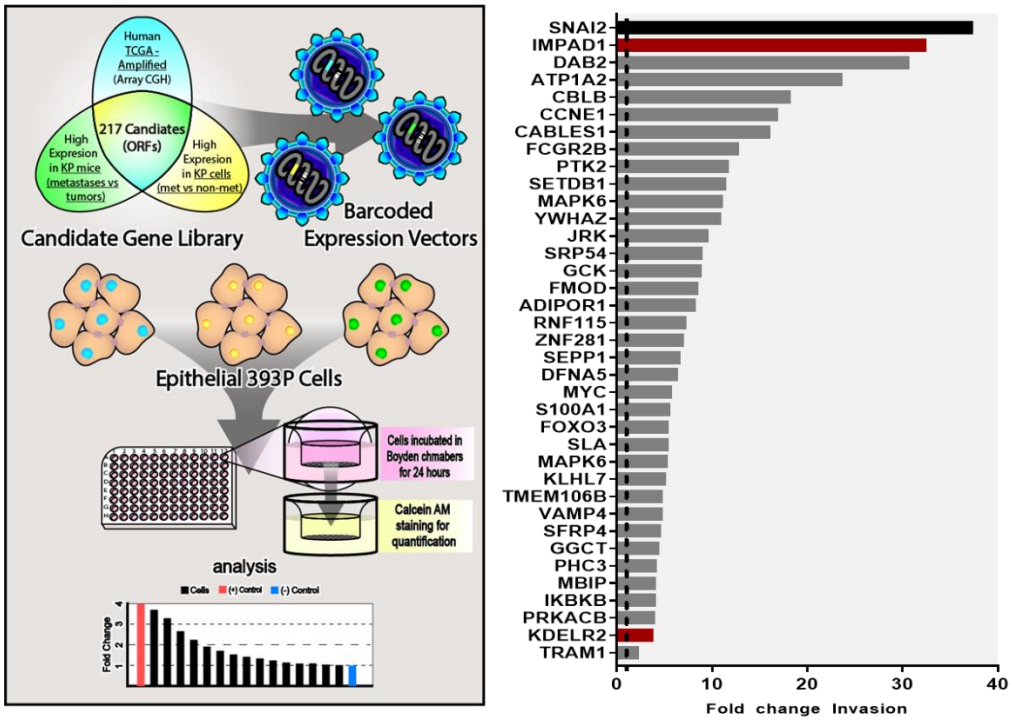

Figure 3-1. Novel screen identifies IMPAD1 and KDELR2 as drivers of lung cancer invasion and disease progression. A. *Schematic representation of workflow for the in vitro screen. DNA barcoded candidate genes were overexpressed in non-invasive & non-metastatic 393P murine tumor cell line using lentiviral infection. Individual ORF-barcoded cell lines were randomly grouped and individually seeded in quadruplicates in 96-well Boyden chambers. Invaded cells were quantified and plotted as shown in representative histogram.* ***B.*** *Waterfall plot demonstrates 37 hits that showed a significant increase in fold change invasion across all cohorts when compared to mCherry. SNAI2 (in black) used as a positive control and mCherry as a negative control, which is denoted as a dotted line (fold change of 1). IMPAD1 and KDELR2, the hits that also showed a significant change in invasion upon further validation (Figure 3-11A-F) with 3 different migration/invasion assays, are represented as red bars.*

3.2 Impad1 and Kdelr2 are novel drivers of lung cancer invasion and metastasis

Inositol monophosphatase domain containing 1 (Impad1) is a Golgi-resident phosphatase that drives the sulfation of glycosaminoglycans (GAGs), which are then

secreted from the Golgi and form the cartilaginous extracellular matrix (ECM) (Frederick et al., 2008; Sohaskey, Yu, Diaz, Plaas, & Harland, 2008). In humans, loss-of-function (LOF) of the enzyme is associated with diseases involving bone and cartilage deformities such as chondrodysplasia (Vissers et al., 2011). Furthermore, in the context of cancer, Impad1 is hypomethylated and co-amplified with oncogenes like *MYC* (Parris et al., 2014; Plasterer et al., 2019). However, nothing is known about the functional impact of Impad1 upregulation and its role in Golgi secretion or cancer metastasis. KDEL endoplasmic reticulum protein retention receptor 2 (Kdelr2) is a transmembrane-domain protein belonging to the KDEL receptor (Kdelr) family (Cancino, Jung, & Luini, 2013; Capitani & Sallese, 2009; Wiersma, Michalak, Abdullah, Bremer, & Eggleton, 2015a). Kdelr2 localizes to the ER–Golgi intermediary complex (ERGIC) and binds to chaperone proteins with a KDEL ligand and traffics them back to the ER via retrograde transport. In melanoma cells, increased Kdelr retrograde activity in turn promoted anterograde trafficking, invadopodia formation and ECM degradation (Ruggiero et al., 2015; Ruggiero et al., 2018). However, the function of Kdelr2, specifically, in driving Golgi exocytosis, and promoting lung cancer invasion and metastasis remains unstudied.

Impad1 and Kdelr2 showed as significant hits when quantified by both statistical methods 1 and 2. Moreover, they were the only two hits that significantly enhanced invasion compared to mCherry across the three validation platforms – 2D migration, 2D invasion, and 3D invasion **(Figure 3-11F)**. Thus, I further delved into the role of each of these genes in promoting lung cancer invasion and metastasis. To do this, I first determined the clinical relevance of IMPAD1 and KDELR2 expression in

NSCLC patients by mining the TCGA lung adenocarcinoma dataset containing 517 samples (Firehouse). 18% and 19% of the patients showed alterations in Impad1 and KDELR2, respectively (https://www.cbioportal.org) **(Figure 3-2A)**. 4% of patients showed an amplification in both IMPAD1 and KDELR2. Patients with IMPAD1 alterations had significantly worse disease-free survival compared to the patients with no alterations, with a median of 26.12 months for high expression and 41.23 months for low expression (log rank $P = 0.0391$) **(Figure 3-2B)**. Patients with alterations in KDELR2 with a median survival of 25.22 months also did significantly worse when compared to 41 months for patients with no alterations (log rank $P = 9.048e-3$) **(Figure 3-2C)**. The negative correlation between gene expression and patient survival was replicated in various other mRNA expression-based lung adenocarcinoma datasets **(Figure 3-12A, C)** (Gyorffy, Surowiak, Budczies, & Lanczky, 2013), as well as in the Human Protein Atlas dataset that uses protein expression **(Figure 3-12B, D)** (Uhlen et al., 2015; Uhlen et al., 2017). Increased IMPAD1 and KDELR2 co-expression worsened disease-free survival (median for cases with alterations 25.33 months) similarly to only IMPAD1 or KDELR2 amplification, indicating that a single gene alteration is sufficient to impact survival **(Figure 3-12E)**. Hence, I proceeded to study Impad1 and Kdelr2 as distinct drivers of NSCLC invasion and metastasis.

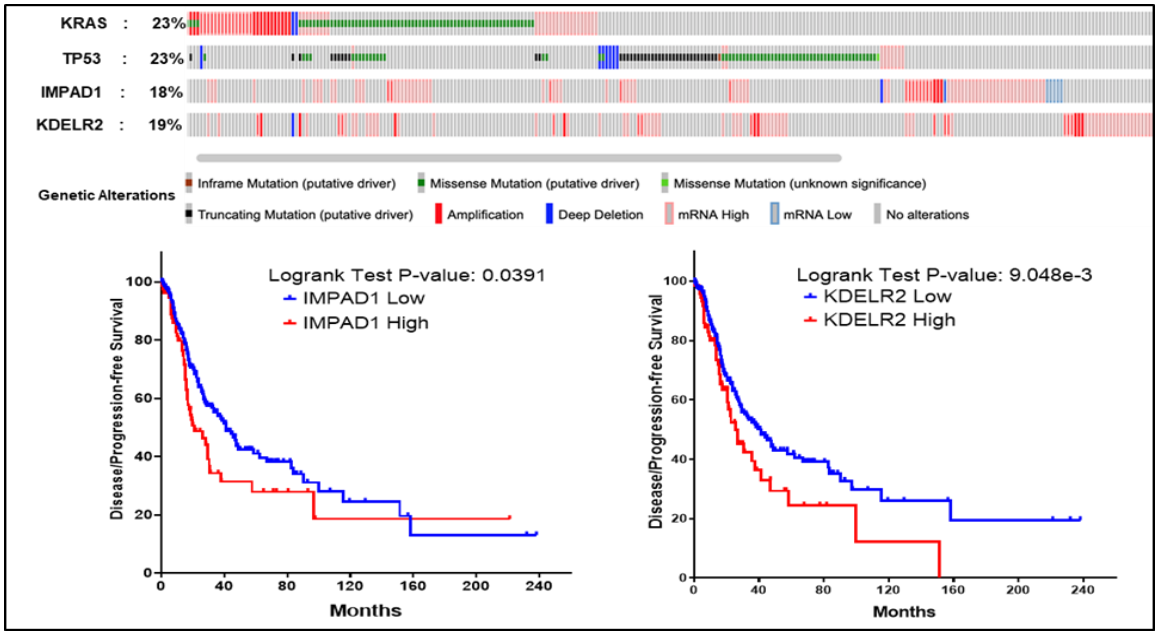

Figure 3-2. IMPAD1 and KDELR2 drive disease progression in lung cancer patients. A. *IMPAD1 and KDELR2 amplification and mutation frequency in lung adenocarcinoma (LuAd) in relation to putative LuAd drivers, Kras and Tp53, as reported by TCGA.* ***B-C.*** *Kaplan–Meier survival analysis shows significantly poor outcome in disease-free survival of LuAd patients with increased expression of (B) IMPAD1, and (C) KDELR2. See also Figure 3-12.*

To validate Impad1 as a driver of invasion and more importantly metastasis, the human IMPAD1 cDNA was overexpressed in murine 393P, 344SQ, and human HCC827 NSCLC cell lines either constitutively or via doxycycline induction **(Figure 3-3A, B,Figure 3-13A)**. Increased IMPAD1 expression made the cells more invasive in transwell assays, as well as enhanced their cellular motility in wound healing assays **(Figure 3-3C-H, Figure 3-13B)**. I recapitulated this phenotype in a 3D collagen/Matrigel matrix that resembles the tumor ECM, where heightened Impad1 levels prompted the formation of invasive spheroids **(Figure 3-3I, J, Figure 3-13C)**.

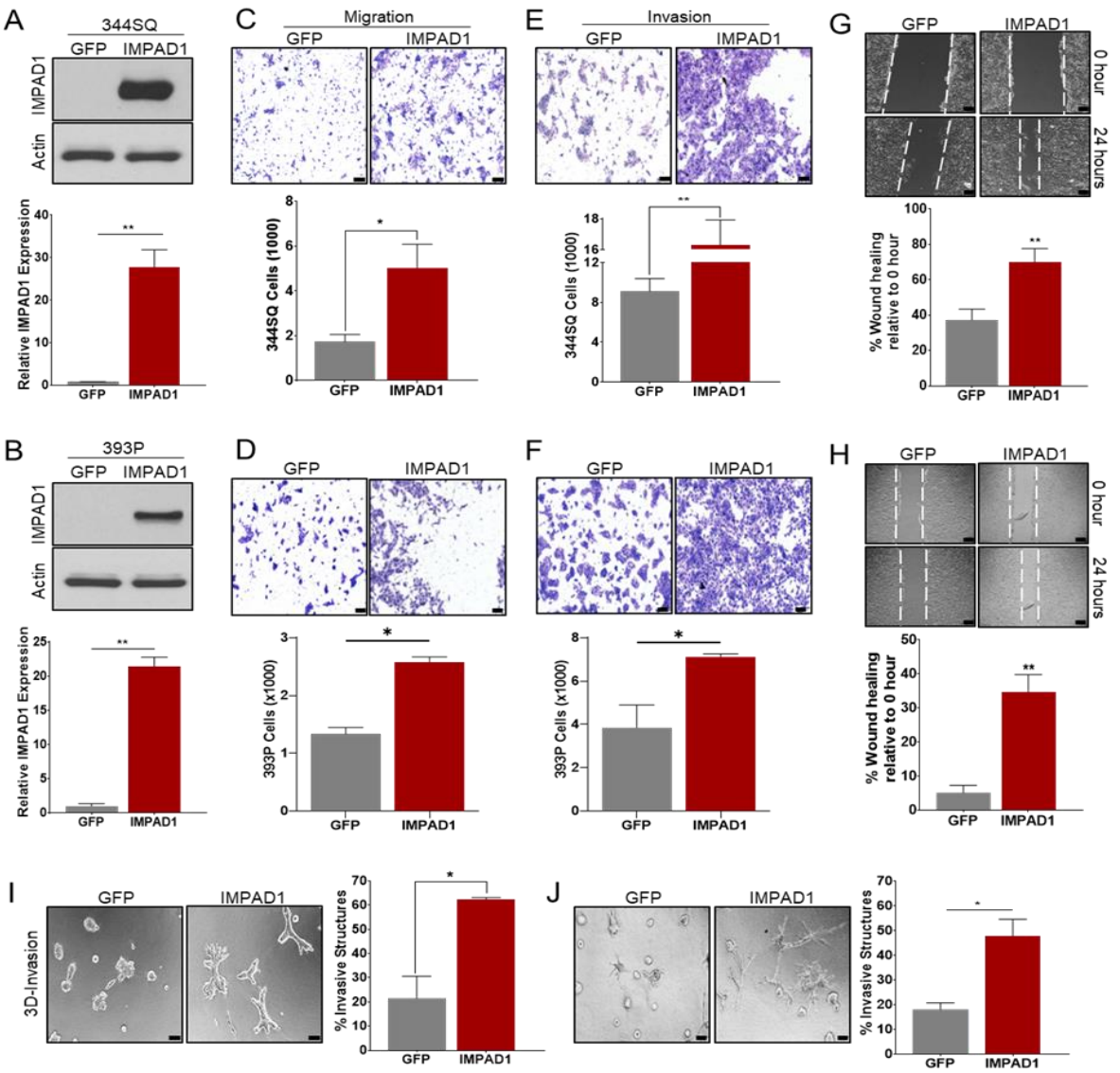

Figure 3-3. IMPAD1 expression is sufficient to drive lung cancer invasion. A, B. *RT-qPCR and western blot analysis for human IMPAD1 expression in 344SQ (A) and 393P (B) cells with stable overexpression.* ***C-H.*** *Cells overexpressing IMPAD1 show a significant increase in (C, D) migration, (E, F) invasion, and (G, H) wound healing at 24 hours (scale bar: 100uM, wound healing assay 200uM).* ***I, J.*** *IMPAD1 overexpressing cells form significantly more invasive structures compared to GFP in 3D matrix comprising of 1.5 mg/ml Collagen in Matrigel by day 6 (scale bar: 100uM). See also Figure 3-13.*

Next, I studied Impad1 as a driver of metastasis *in vivo*, by using the 344SQ-vector and -IMPAD1 constitutively overexpressing cells that were subcutaneously implanted into WT 129/Sv syngeneic mice. IMPAD1 expression had no effect on tumor

volume over 7 weeks, which was analogous to the phenotype observed *in vitro* where cellular proliferation was also not dependent on Impad1 **(Figure 3-4A, B, Figure 3-14A-C)**. Despite no change in tumor volume, IMPAD1 upregulation resulted in a significant increase in metastasis, determined by the number of macroscopic lung metastatic nodules **(Figure 3-4C, D)**. IMPAD1 overexpression was confirmed in the SQ tumors **(Figure 3-4E, F)**. I substantiated Impad1 as a potent driver of metastasis irrespective of the innate metastatic ability of the cells by using the non-metastatic 393P KP cell line **(Figure 3-4G-L)**.

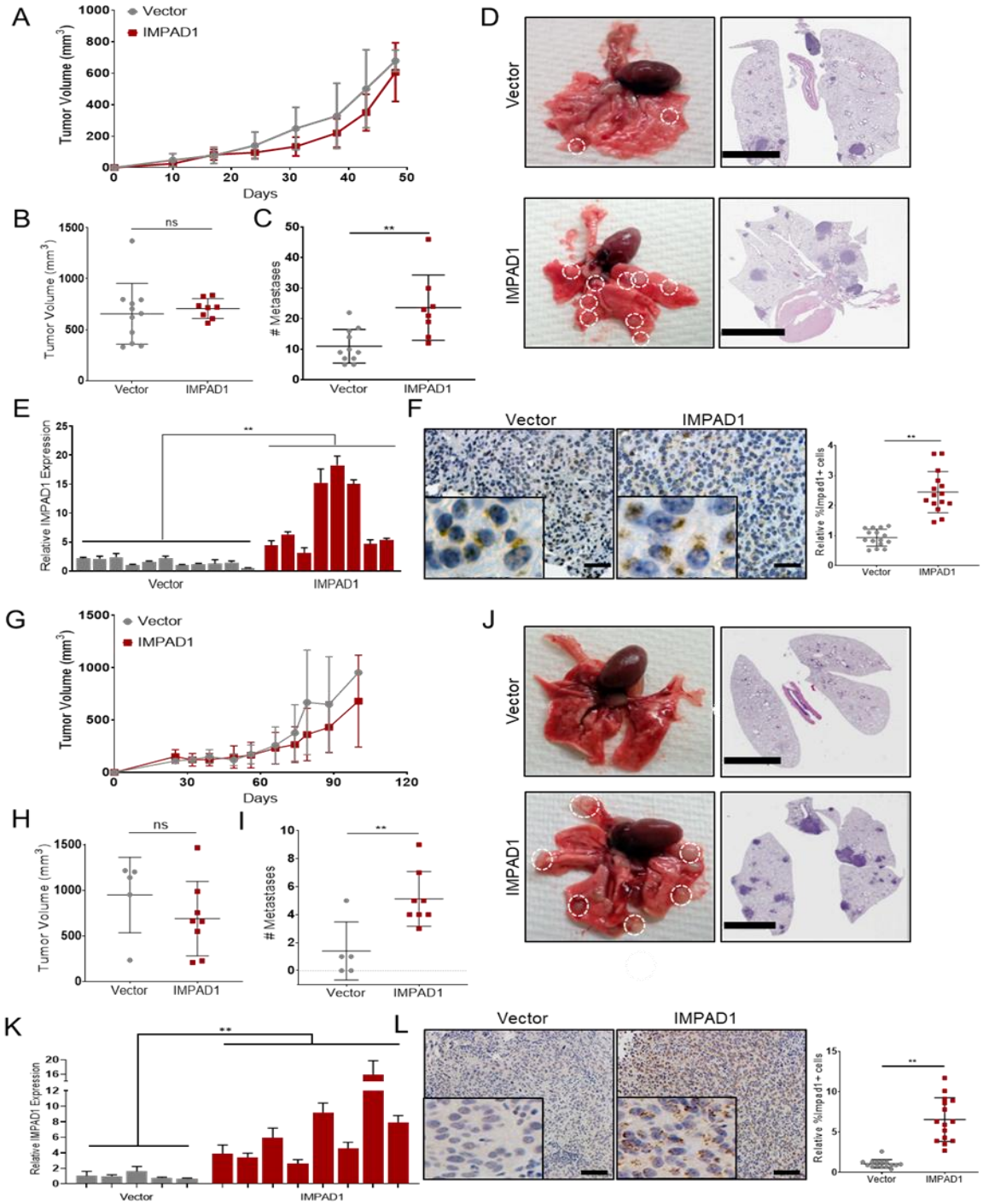

Figure 3-4. IMPAD1 expression is sufficient to drive lung cancer metastasis. A, B *Primary tumor growth for 344SQ Vector (n=11) and Impad1 (n=8) overexpressing cells implanted subcutaneously into syngeneic mice (A) over time, and (B) at time of euthanasia.* ***C****. IMPAD1 overexpressing cells form significantly more lung metastatic nodules compared to control.* ***D****. Representative lungs and their respective H&E stained sections (scale bar 5mM). Analysis to confirm overexpression of Impad1 in*

SQ tumors by (E) RT-qPCR for RNA, and (F) immunohistochemistry for protein, as quantified (scale bar: 20uM). ***G-L****. Same as above with 393P cells. See also Figure 3-14. Data are represented as mean ± SEM. Significance by Student's T-test. P-value<0.05 - *; <0.002 - **.*

Like Impad1, doxycycline-mediated Kdelr2 induction in the murine 393P, 344SQ, and human HCC827 models exacerbated the cellular invasiveness and motility of lung cancer cells *in vitro* **(Figure 3-5A-J, Figure 3-15A-C)**.

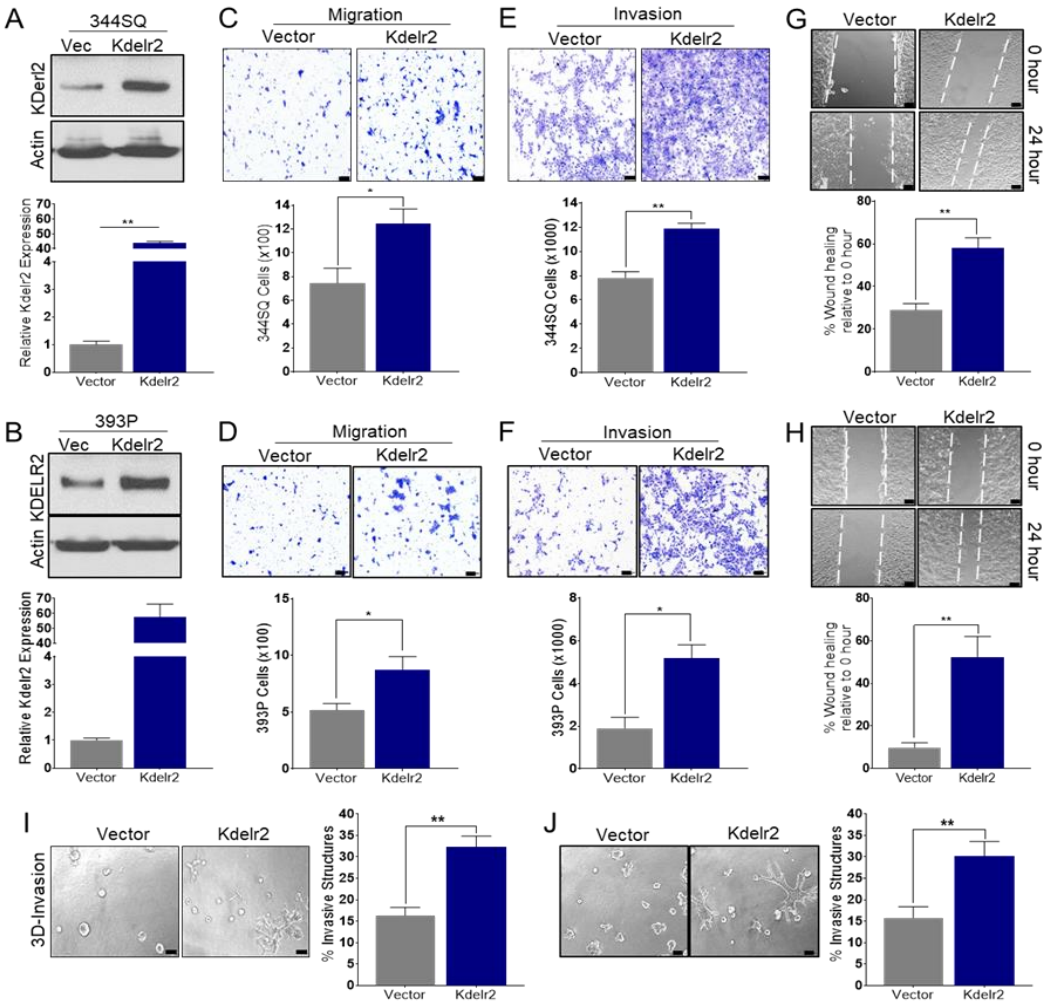

Figure 3-5. Kdelr2 expression is sufficient to drive lung cancer invasion. A, B. *RT-qPCR and western blot analysis for mouse Kdelr2 expression in 344SQ (A) and 393P (B) cells with doxycycline-inducible overexpression after 24-hour induction.* ***C-F.*** *Cells overexpressing Flag-tagged Kdelr2 show a significant increase in (C, D) migration, (E, F) invasion, and (G, H) wound healing after 24-hour induction (scale bar: 100uM).* ***I, J.*** *Kdelr2 overexpressing cells pre-induced for 24 hours before seeding*

form significantly more invasive structures in 3D matrix comprising of 1.5 mg/ml Collagen in Matrigel by day 6 (scale bar: 100uM). See also Figure 3-15

To study the effect of Kdelr2 upregulation *in vivo*, I implanted the 344SQ-vector or -Kdelr2 cells into mice. Kdelr2 significantly increased lung cancer metastases in mice without altering primary tumor growth **(Figure 3-6A, B)**. This was once again recapitulative of the *in vitro* data where Kdelr2 showed no significant effect on cellular proliferation **(Figure 3-16A-C)**. Kdelr2 induction was validated in the SQ tumors **(Figure 3-6C-F)**. Thus, the above *in vitro* and *in vivo* studies substantiate that upregulation of either of the genes, Impad1 or Kdelr2, is sufficient to independently drive lung cancer invasion and metastasis without altering cellular proliferation.

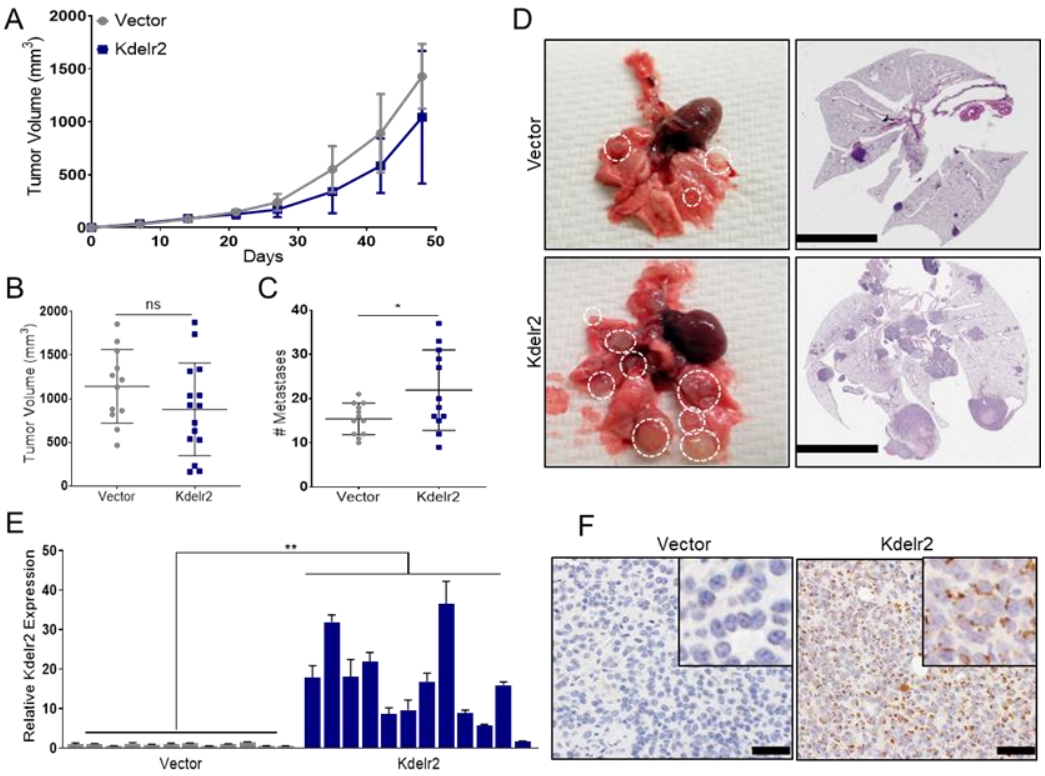

Figure 3-6. Kdelr2 expression is sufficient to drive lung cancer metastasis. A, B *Primary tumor growth for 344SQ control and Kdelr2 inducible cells implanted subcutaneously in syngeneic mice (A) over time, and (B) at time of euthanasia. N=12.* ***C.*** *Kdelr2 overexpressing cells form significantly more*

lung metastases compared to control. ***D.*** *Representative lungs and H&E stained sections showing increased metastases in lungs from mice implanted with Kdelr2 overexpressing cells compared to GFP control (scale bar: 5mM).* ***E, F.*** *Analysis to confirm overexpression of Flag-tagged KDELR2 in SQ tumors by (E) RT-qPCR for RNA, and (F) Flag IHC for protein (scale bar: 50uM). See also Figure 3-16. Data are represented as mean ± SD. Significance by Student's T-test. P-value<0.05 - *; <0.002 - **.*

Next, I ascertained if Impad1 and Kdelr2 are also necessary for promoting cancer malignancy. The genes were independently inhibited by using three distinct shRNAs in metastatic 344SQ and 344P murine cells **(Figure 3-7A, E, Figure 3-17A, D)**. Impad1 or Kdelr2 repression caused a significant decrease in their invasive abilities in 2D and 3D matrices indicating their essentiality for tumor cell invasion **(Figure 3-7B-D, F-G, Figure 3-17B, C, E, F)**.

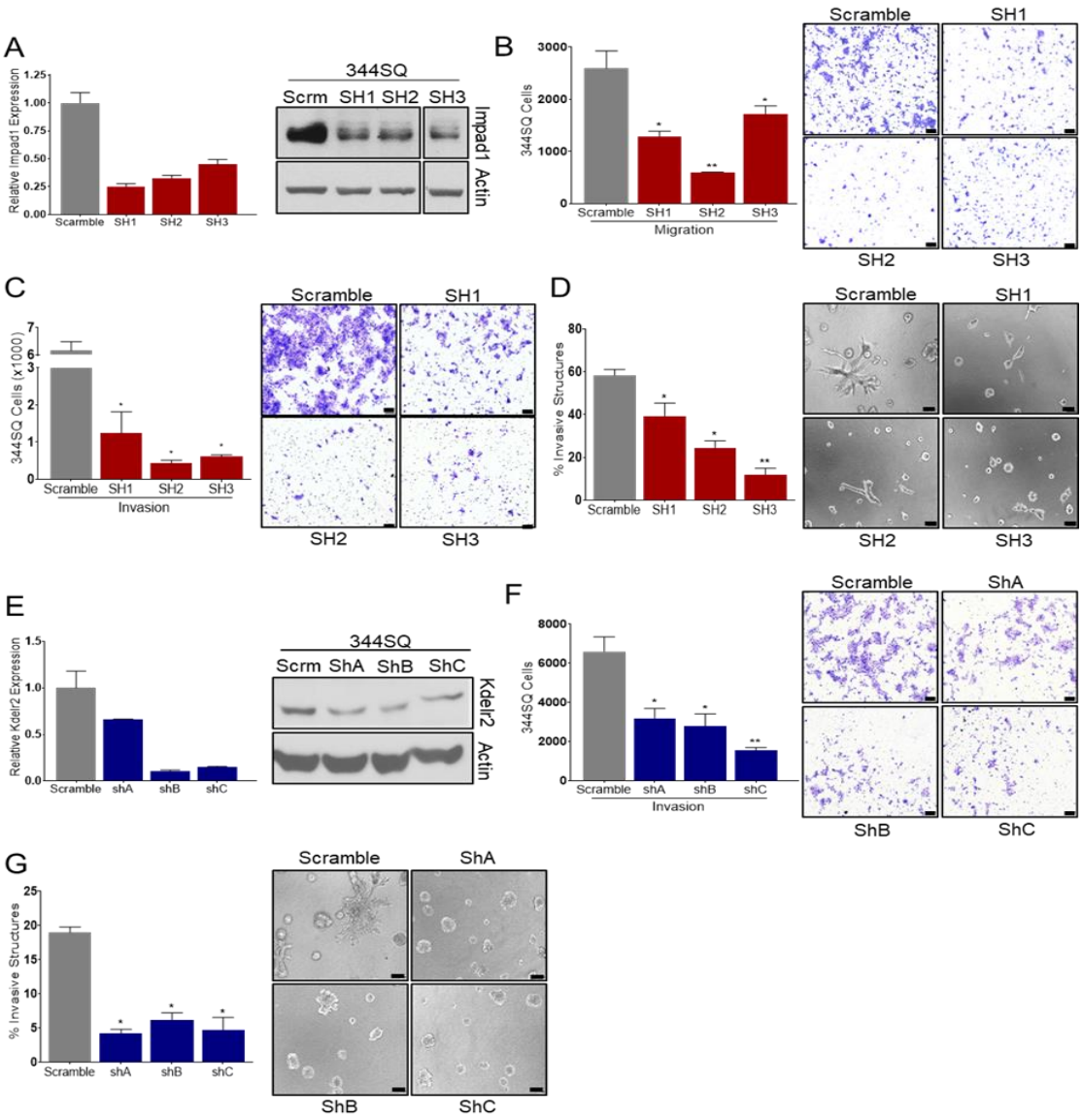

Figure 3-7. Impad1 or Kdelr2 expression is necessary for invasive ability of lung cancer cells. A. *RT-qPCR and western blot analysis for mouse Impad1 expression in 344SQ cells with stable knockdown compared to scramble control. B-D. Knockdown of Impad1 shows a significant decrease in 2D migration (B), 2D invasion (C), and 3D invasion (D) of 344SQ cells. (scale bar: 100uM).* ***E.*** *qPCR and western blot analysis for mouse Kdelr2 expression in 344SQ cells with stable knockdown compared to scramble control.* ***F, G.*** *Kdelr2 knockdown cells are less invasive in 2D (F) and 3D (G) matrix. (scale bar: 100uM) See also Figure 3-17.*

To study the effect of Impad1 suppression on metastasis, the 344SQ scramble control and knockdown cells were implanted into the syngeneic 129/Sv mice and their tumor growth observed over 6 weeks. Similar to the proliferation assays *in vitro* **(Figure 3-18E)**, there was no effect of Impad1 on the tumor volume **(Figure 3-8A, B)**. However, loss of Impad1, which was confirmed in the SQ tumors, significantly reduced the metastatic ability of the 344SQ cells **(Figure 3-8C-F)** Despite a significant repression of Impad1 levels that correlated with decreased invasiveness *in vitro*, there was no change in the metastases for the SH2-Impad1 and SH3-Impad1 tumor groups compared to control **(Figure 3-18A-C)**. The data indicated that the tumors from these two cohorts did not retain Impad1 suppression over time *in vivo*, explaining the absence of a change in the metastatic phenotype **(Figure 3-18D)**. Thus, the knockdown data suggests that Impad1 expression is required for NSCLC invasion and metastasis.

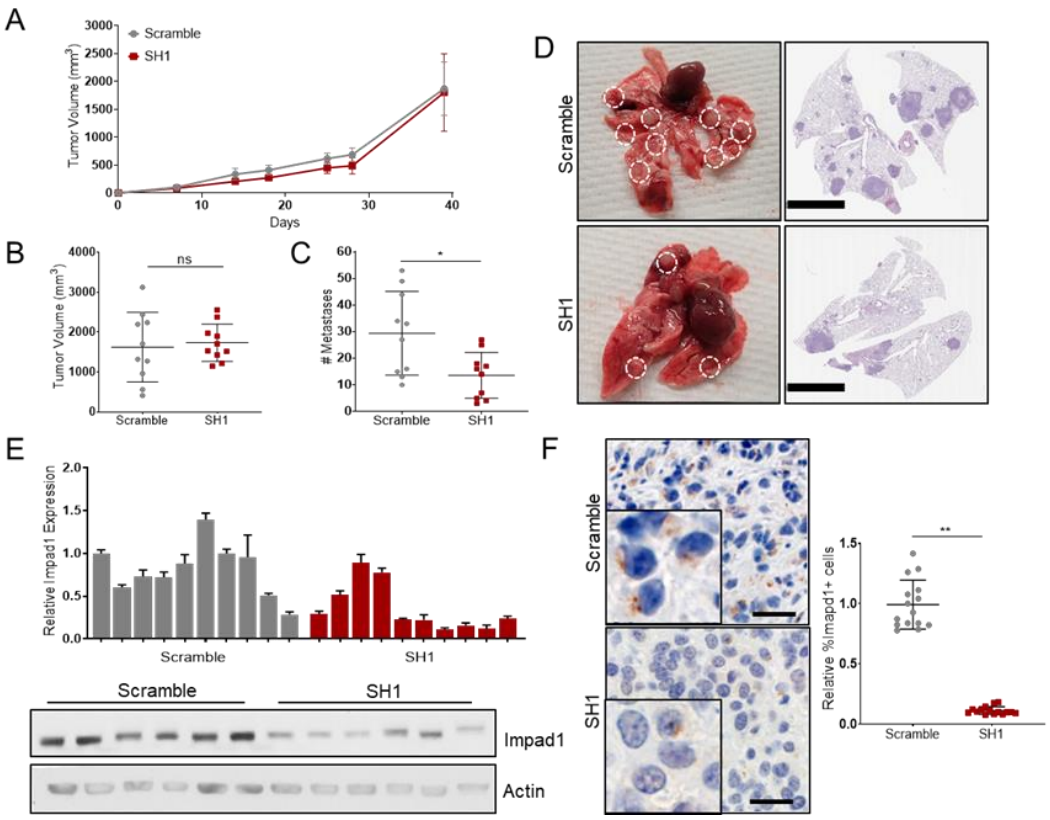

Figure 3-8. Impad1 expression is necessary for metastatic ability of lung cancer cells. A, B. *Primary tumor growth for 344SQ scramble and SH1 Impad1 knockdown cells implanted subcutaneously into syngeneic mice (A) over time, and (B) at time of euthanasia. N=10.* ***C.*** *Impad1 knockdown cells form significantly less lung metastatic nodules compared to scramble control.* ***D.*** *Representative lungs and their respective H&E stained sections (scale bar 5mM).* ***E, F*** *Confirmation of loss of Impad1 expression by qPCR (E), western blot (E), and IHC (F) (Scale bar: 20uM). See also Figure 3-18.*

To investigate the requirement of Kdelr2 in lung cancer metastasis, 344SQ scramble control and Kdelr2 knockdown cells (shA, shB, and shC) were similarly implanted into mice. Although the proliferation assays showed a significant reduction in cellular growth upon Kdelr2 repression *in vitro* **(Figure 3-19E)**, there was no significant change in tumor volume **(Figure 3-9A, B, Figure 3-19A)**. This difference in the outcome of cellular proliferation *in vitro* and tumor growth *in vivo* illuminates the

diverse factors required for one vs the other. Despite no change in tumor volume, a significant decrease in metastasis was observed upon Kdelr2 knockdown, which was validated by using the SQ tumors **(Figure 3-9C-F, Figure 3-19B-D)**.

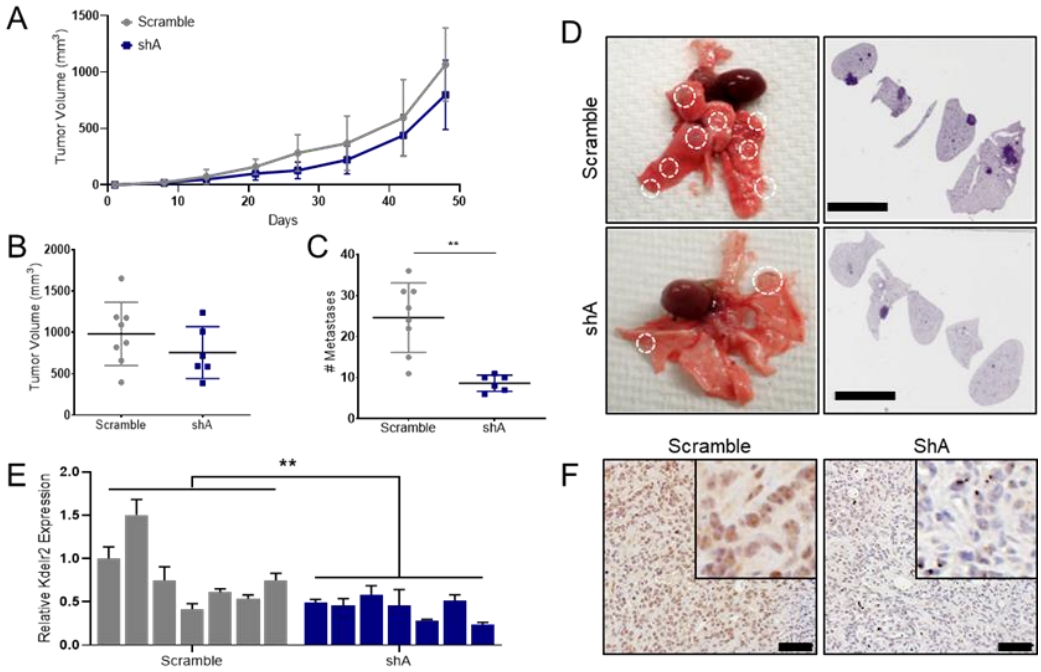

Figure 3-9. Kdelr2 expression is necessary for metastatic ability of lung cancer cells. A, B. *Primary tumor growth for 344SQ scramble and shA Kdelr2 knockdown cells implanted subcutaneously into syngeneic mice (A) over time, and (B) at time of euthanasia. N=10.* ***C.*** *Kdelr2 knockdown cells form significantly less lung metastatic nodules compared to scramble control.* ***D.*** *Representative lungs and their respective H&E stained sections (scale bar 5mM).* ***E, F.*** *Confirmation of loss of Impad1 expression by qPCR (E), and IHC (F) (Scale bar: 50uM). See also Figure 3-19*

3.3 Discussion and conclusions

Metastasis still accounts for 90% of all cancer-related mortality, and cancer cell invasion is an essential functional requirement for the disease (Friedl, Locker, Sahai, & Segall, 2012; Lambert, Pattabiraman, & Weinberg, 2017). Therefore, understanding regulators of these processes is important to therapeutically prevent lung cancer

metastasis (Steeg & Theodorescu, 2008). In parallel to the previously published *in vivo* screen (Grzeskowiak et al., 2018; S. T. Kundu et al., 2018) , we performed a GOF *in vitro* invasion screen, where we identified several known and novel drivers of invasion. Moreover, I further explored the two hits that promoted invasion in all the secondary validation assays, Impad1 and Kdelr2, which were also demonstrated as drivers of metastasis *in vivo*. This was an intriguing revelation as neither of these genes were hits in the *in vivo* screen. This could be explained as the *in vivo* metastasis screen used a competitive positive selection to identify hits based on a growth advantage; but our data show that neither Impad1 nor Kdelr2 can alter cellular proliferation or tumor growth, but robustly promote invasion and metastasis. Given that Imapd1 and Kdelr2 have no effect on cellular proliferation or tumor growth, targeting the protein holds potential to specifically treat metastasis without affecting normal cell growth.

The TCGA dataset showed that IMPAD1 (18%) and KDELR2 (19%) overlap with and are altered to almost the same extent as putative drivers of lung adenocarcinoma, KRAS (23%) and TP53 (23%). Therefore, I used the syngeneic *Kras* and *Tp53* mutant cell lines to study IMPAD1 and KDELR2 as drivers of NSCLC invasion and metastasis. Using the human non-invasive HCC827 cell line with an activating EGFR mutation, I demonstrated that the phenotypic effects of the two genes are independent of the species, mutational status, or baseline metastatic potential. Our study is the first to elucidate the individual roles of IMPAD1 and KDELR2 in driving tumorigenesis and metastasis.

Due to the stringent cut-offs applied, additional hits such as CBL-B, ADIPOR1, ATP1A2, and JRK were not explored. Casitas B-lineage lymphoma-b (CBL-B), an E3 ubiquitin ligase, drives degradation of TAM tyrosine kinase receptors, leading to repressed natural killer cells and increased metastasis (Paolino et al., 2014). However, it has also been established as a metastasis repressor in gastric and breast cancers (Xu et al., 2017). Adiponectin Receptor 1 (ADIPOR1) activates the AMPK pathway and acts as a tumor and metastasis suppressor through AMPK signaling (Tang & Lu, 2009; Wu, Yan, Zhang, Du, & Wan, 2012). However, ADIPOR1 was a hit in our oncogene invasion screen indicating a hitherto unidentified dual functionality of both ADIPOR1 and AMPK as oncogenes and tumor suppressors. ATPase Na+/K+ Transporting Subunit Alpha 2 (ATP1A2) is part of the Na+/K+ -ATPases (NKP) family which are altered in and play a role in invasion of endocrine resistant breast cancer cells (Bogdanov, Moiseenko, & Dubina, 2017; Khajah, Mathew, & Luqmani, 2018). Jrk Helix-Turn-Helix (JRK) protein promotes hyper-activation of β-catenin, thereby driving cellular proliferation and tumorigenesis (Pangon et al., 2016). Thus, our screen identified multiple genes which are potential metastasis drivers. Detailed mechanistic studies on these genes can help enhance our understanding of the complexities of metastasis and establish them as novel targets.

3.4 Supplemental data

Figure 3-10. Fold change invasion for candidate genes from individual groups relative to mCherry of the respective cohort. A-L. *Hits within individual groups were pooled and their fold change invasion was calculated relative to the negative control, mCherry, of the corresponding cohort.*

Standard deviation (SD) (green dashed line), 2X SD (red dashed line), and 3X SD (purple dashed line) was obtained across hits within each group. We identified hits that showed a fold-change invasion significantly higher than 3X SD of mCherry within the corresponding group.

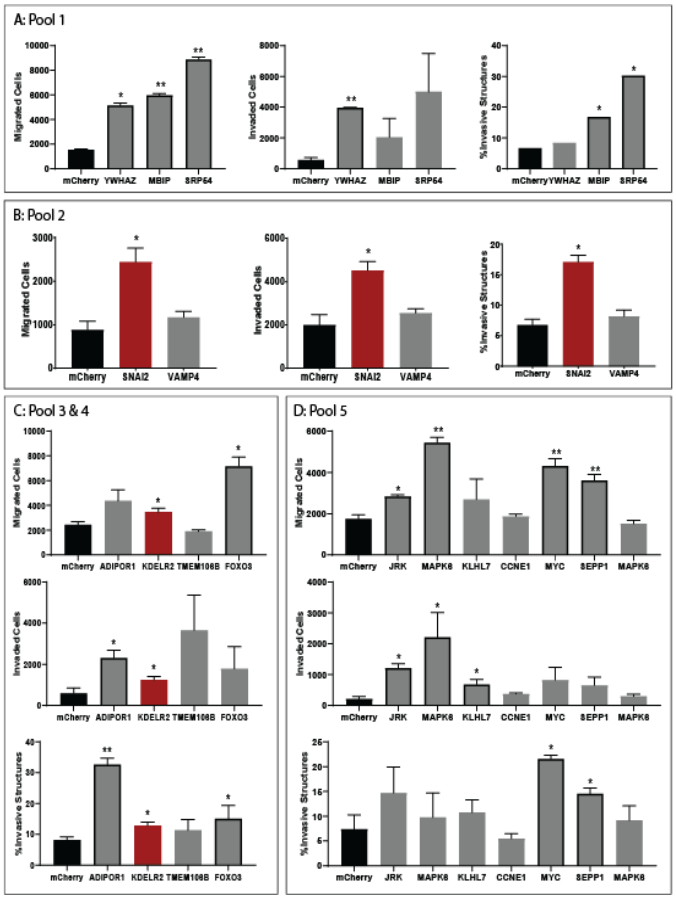

F

HITS	MIGRATION	INVASION	3D-INVASION	HITS	MIGRATION	INVASION	3D-INVASION
YWHAZ	0.007	0.0007	0.468	KLHL7	0.239	0.022	0.193
MBIP	0.001	0.167	0.0447	CCNE1	0.421	0.050	0.277
SRP54	0.0007	0.089	----	MYC	0.001	0.117	0.001
SNAI2	0.0036	0.002	0.00001	SEPP1	0.001	0.093	0.011
VAMP4	0.117	0.173	0.146	MAPK6	0.195	0.243	0.421
ADIPOR1	0.056	0.005	0.0007	IMPAD1	0.001	0.048	0.0000006
KDELR2	0.011	0.028	0.004	DAB2	0.075	0.832	0.330
TMEM108B	0.043	0.086	0.232	ATP1A2	0.279	0.009	0.002
FOXO3	0.0048	0.187	0.039	CBLB	0.210	0.059	0.008
JRK	0.005	0.002	0.062	CABLES1	0.074	0.085	0.540
MAPK6	0.0001	0.048	0.449	DFNA5	0.0002	0.669	0.010

Figure 3-11. Validation of hits from individual groups by using 2D migration and invasion, and 3D invasion identifies Snai2, Impad1, and Kdelr2 as drivers of invasion. A-E. *The hits that showed a fold-change invasion significantly higher than 3X SD in Fig S1 were validated by using 2D migration and invasion, and 3D invasion assays. In addition to the positive control SNAI2, I identified Impad1 and Kdelr2 as the only hits that showed a significant increase in invasion across all three assays (red bars).* ***F.*** *P-values for all experiments in A-E was calculated by Student's T-test by using three experimental replicates. Snai2, Impad1, and Kdelr2 are the only three hits showing p-value<0.05 across all three platforms (shown in red).*

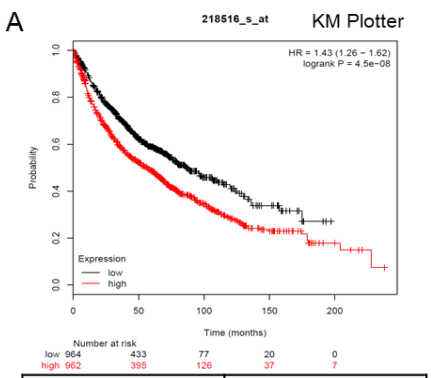

Low Expression (months)	High Expression (months)
86.27	56.8

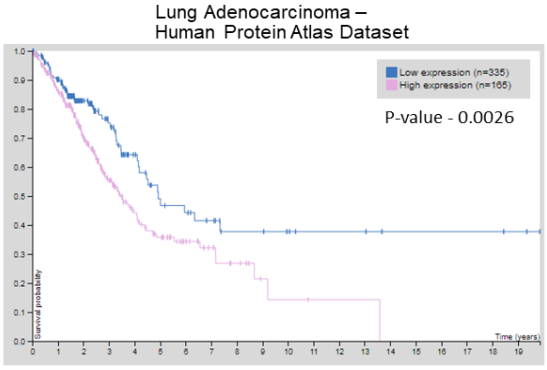

5-year survival low	5-year survival high
49%	36%

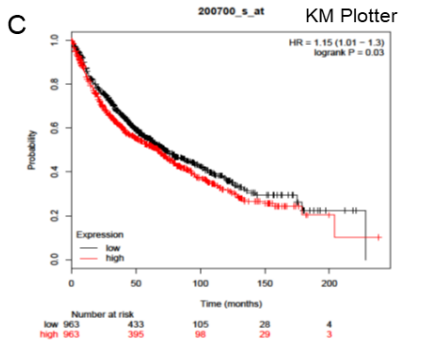

Low Expression (months)	High Expression (months)
72.33	67

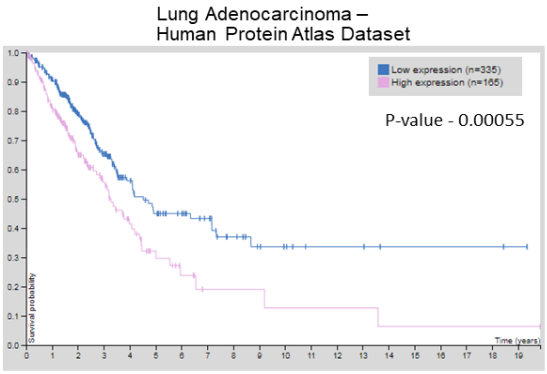

5-year survival low	5-year survival high
45%	32%

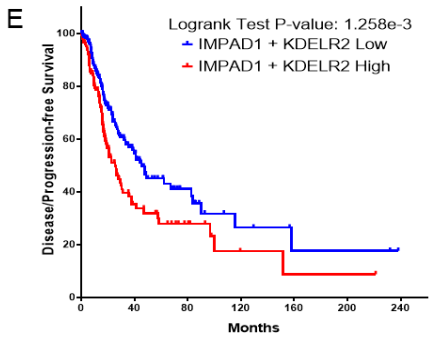

cBioportal

Low Expression (months)	High Expression (months)
45.27	25.33

Figure 3-12. IMPAD1 and KDELR2 amplification correlates with significantly worse disease-free survival. A, B. *High IMPAD1 mRNA (A – KM Plotter) and protein (B – Human Protein Atlas Dataset) expression shows a worse disease-free survival compared to low IMPAD1 expression.* ***C, D.*** *High KDELR2 mRNA (C – KM Plotter) and protein (D – Human Protein Atlas Dataset) expression shows a worse disease-free survival compared to low KDELR2 expression.* ***E.*** *IMPAD1 and KDELR2 mRNA alterations demonstrate worse disease-free survival as compared to samples with no alterations. Median survival is mentioned in the tables below each graph.*

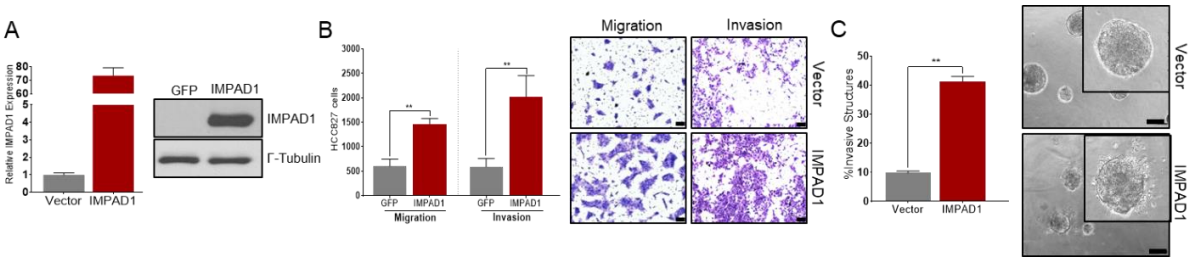

Figure 3-13. IMPAD1 is sufficient to drive lung cancer invasion in human NSCLC models. A *Constitutive overexpression of human IMPAD1 in non-invasive HCC827 cells measured by RNA and protein.* ***B, C.*** *IMPAD1 overexpression promotes 2D migration and invasion by transwell assays (B), as well as 3D invasion in collagen and matrigel (1.5 mg/ml) measured as % invasive structures (C) (scale bar: 100uM).*

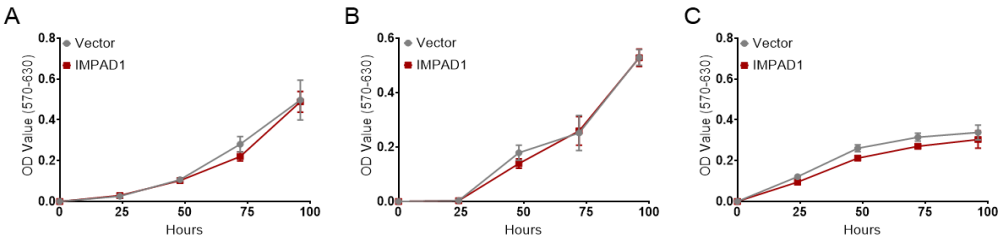

Figure 3-14. Impad1 does not regulate cellular proliferation. *No change in proliferation in vitro as demonstrated by MTT assay and measured by the OD value in 344SQ (A), 393P (B), and HCC827 (C) cells.*

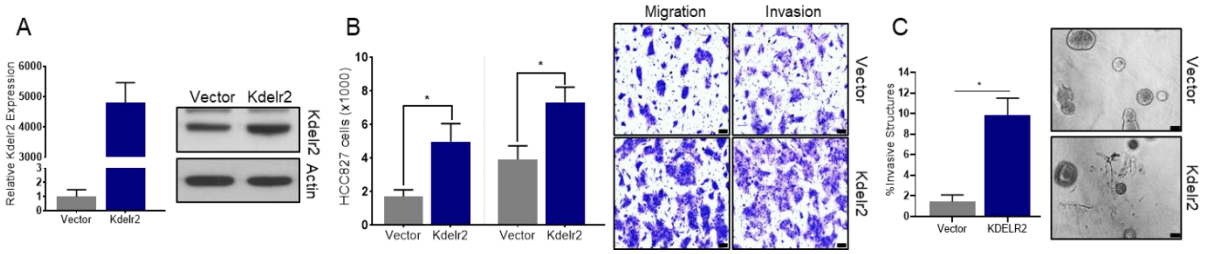

Figure 3-15. Kdelr2 is sufficient to drive lung cancer invasion in human NSCLC models. A *Doxycycline-inducible overexpression of mouse Kdelr2 in non-invasive HCC827 cells measured by RNA and protein.* ***B, C*** *Kdelr2 promotes 2D migration and invasion by transwell assays (B), as well as 3D invasion in collagen and matrigel (1.5 mg/ml) measured as % invasive structures (C).*

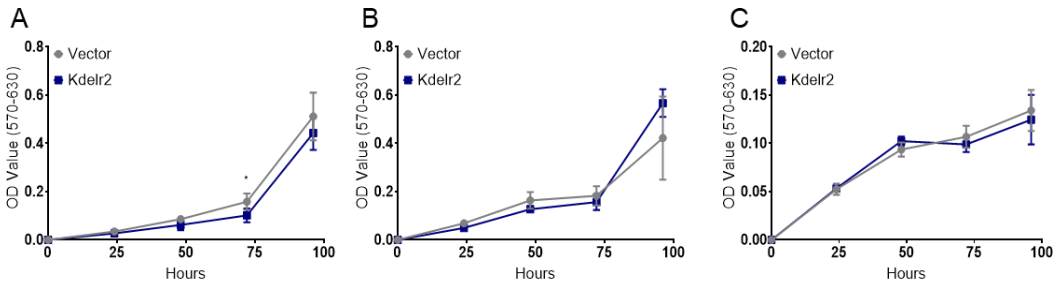

Figure 3-16. Kdelr2 does not regulate cellular proliferation. *No change in proliferation in vitro as demonstrated by MTT assay and measured by the OD value in 344SQ (A), 393P (B), and HCC827 (C) cells.*

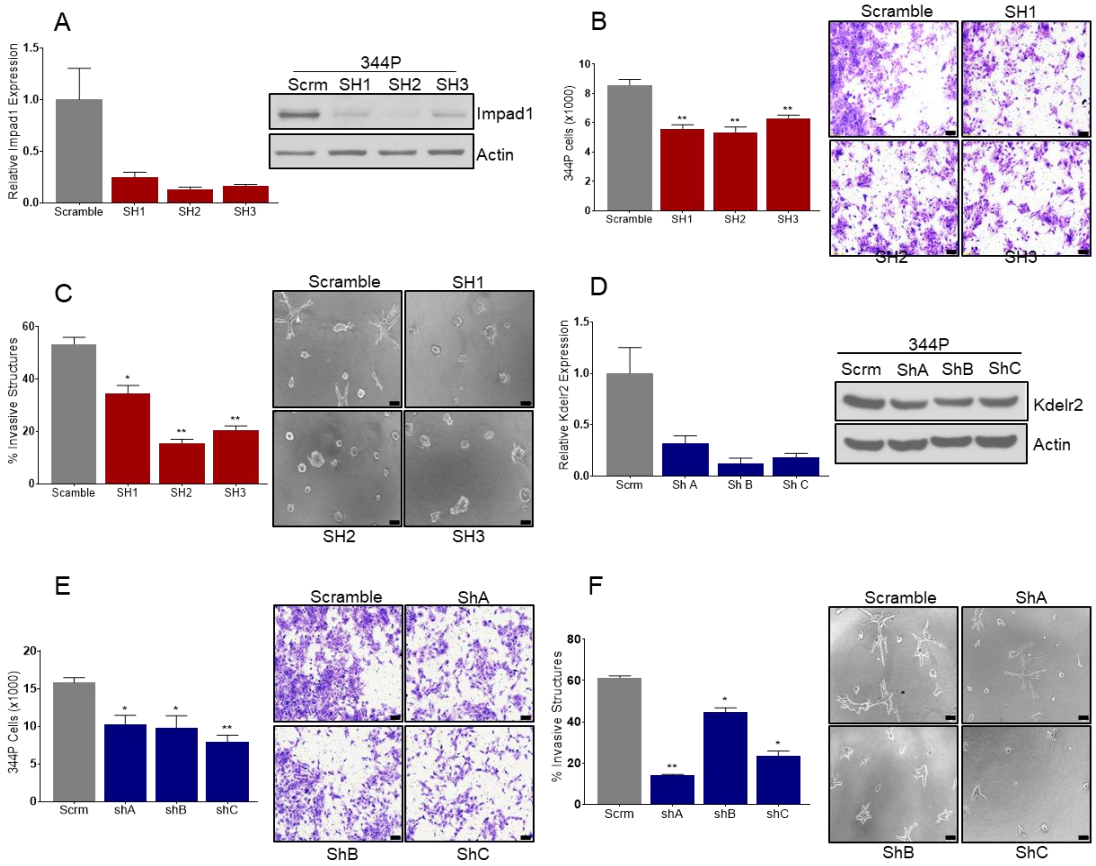

Figure 3-17. Impad1 or Kdelr2 expression is necessary for invasive ability of lung cancer cells. ***A.*** *RT-qPCR and western blot analysis for mouse Impad1 expression in 344P cells with stable knockdown.* ***B, C.*** *Knockdown of Impad1 shows a significant decrease in 2D (B) and 3D invasion (C) of 344P cells. (scale bar: 100uM).* ***D.*** *qPCR and western blot analysis for mouse Kdelr2 expression in 344P cells with stable knockdown.* ***E, F.*** *Kdelr2 knockdown cells are less invasive in 2D (E) and 3D (F) matrices. (scale bar: 100uM)*

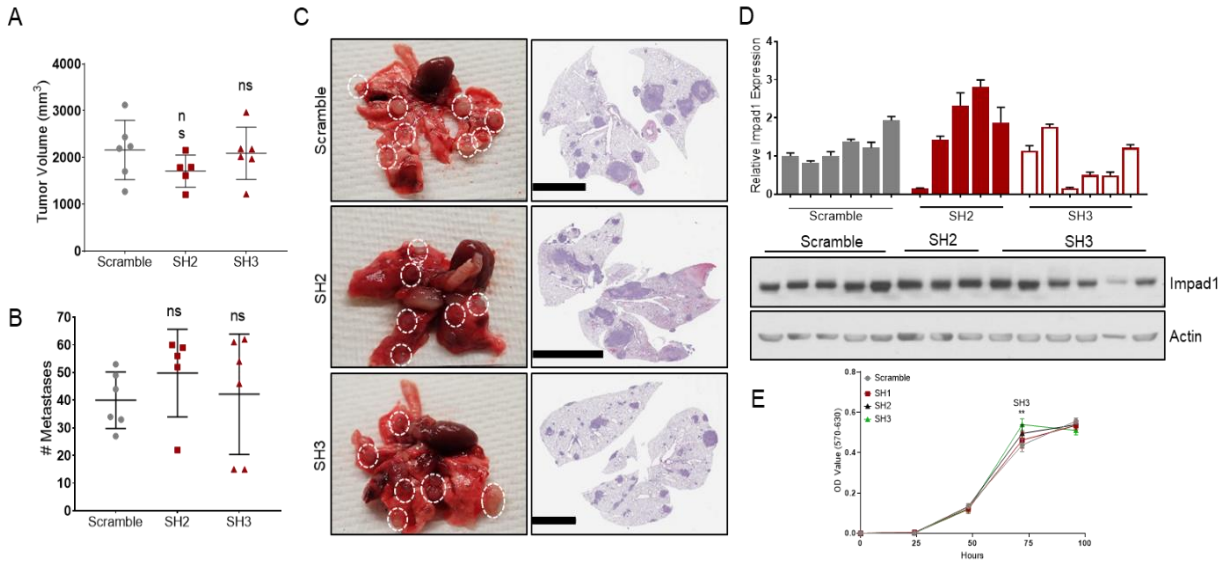

Figure 3-18. Impad1 is necessary for metastatic ability of lung cancer cells. A. *Primary tumor volume for 344SQ scramble, SH2 Impad1, and SH3 Impad1.* ***B.*** *Impad1 knockdown cells show no change in lung metastases.* ***C.*** *Representative lungs and their respective H&E stained sections showing metastases in lungs for SH2, and SH3 cells (Scale bar: 5mM).* ***D.*** *Analysis of primary tumors to ascertain knockdown of Impad1 by RNA (upper), and protein (lower).* ***E.*** *Impad1 knockdown does not alter cellular proliferation in vitro in 344SQ cells as demonstrated by the MTT assay.*

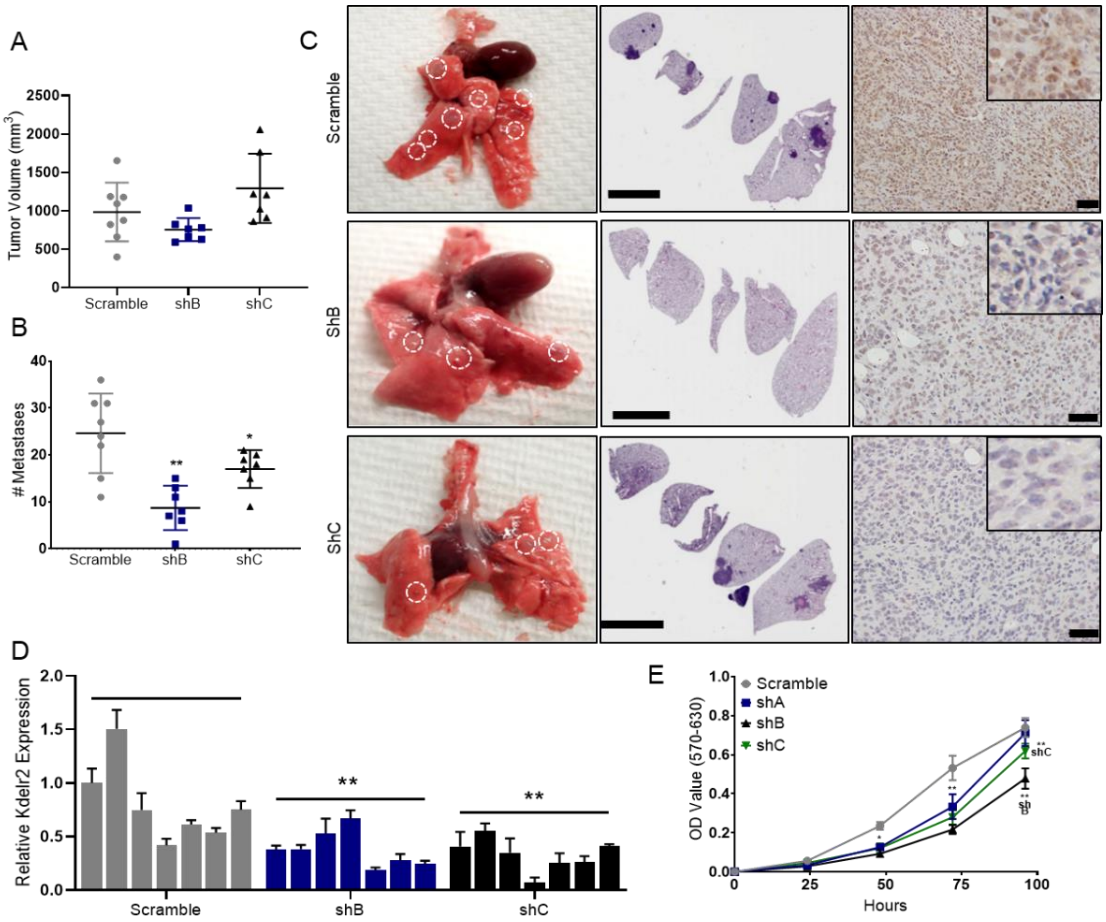

Figure 3-19. Kdelr2 is necessary for metastatic ability of lung cancer cells. A. *Primary tumor growth at time of euthanasia for 344SQ scramble, and the other two shRNA knockdown cells (ShB Kdelr2 and ShC Kdelr2).* ***B.*** *Kdelr2 knockdown cells show decreased lung metastases.* ***C.*** *Representative lungs and their respective H&E stained sections showing metastases in lungs for ShB and ShC cells (Scale bar: 5mM).* ***D.*** *Analysis of primary tumors to ascertain knockdown of Kdelr2 by RNA.* ***E.*** *Kdelr2 knockdown alters cellular proliferation in vitro in 344SQ cells by MTT assay.*

Chapter 4: Oncogenes are upregulated during EMT to drive cancer metastasis

4.1 Impad1 is upregulated during EMT to promote tumorigenesis

Epithelial-to-mesenchymal transition (EMT) is an epigenetically regulated process that has been demonstrated to promote tumorigenesis and metastasis (Kalluri & Weinberg, 2009; Thiery et al., 2009). Previously, our lab and others have established that human and mouse lung cancer cell lines and tumors can be distinguished based on their EMT status (Ahn et al., 2012; Gibbons, Lin, Creighton, Rizvi, et al., 2009; Gibbons, Lin, Creighton, Zheng, et al., 2009). Additionally, these mesenchymal-like (mesenchymal) cells and tumors are more metastatic as compared to their epithelial counterparts. According to the TCGA lung adenocarcinoma dataset, Impad1 is altered in 18% of the patients, similar to *Kras* and *Tp53* mutations **(Figure 3-2A)**. These patients primarily demonstrate mRNA upregulation of the gene, indicating that Impad1 potentially undergoes an epigenetic modulation. To study this, I used the human and mouse NSCLC cell line panels that were stratified based on the inherent EMT status. Impad1 was upregulated in the mesenchymal, malignant cells, correlating with the EMT markers, i.e., increased Zeb1 and reduced E-cadherin expression **(Figure 4-1A, B, Figure 4-3A)**. Impad1 mRNA levels also positively associated with a previously established 76-gene EMT signature (Byers et al., 2013) in 118 human NSCLC lines (McMillan et al., 2018) **(Figure 4-1C)**. Moreover, IHC staining for Impad1 and Zeb1 in NSCLC patient tumor tissues further confirmed this

correlation at the protein level **(Figure 4-1D, Figure 4-3B)**. To investigate if this phenomenon can be mediated by other inducers of EMT, I treated the murine KP (393P and 344SQ), as well as the murine mammary epithelial (NMuMG) cell lines with TGFβ, a cytokine that induces Zeb1 expression and EMT (Gibbons, Lin, Creighton, Rizvi, et al., 2009). Regardless of the species, tissue of origin, baseline EMT status of the cells, and type of induction, Impad1 was upregulated during EMT **(Figure 4-1E-G, Figure 4-3C)**.

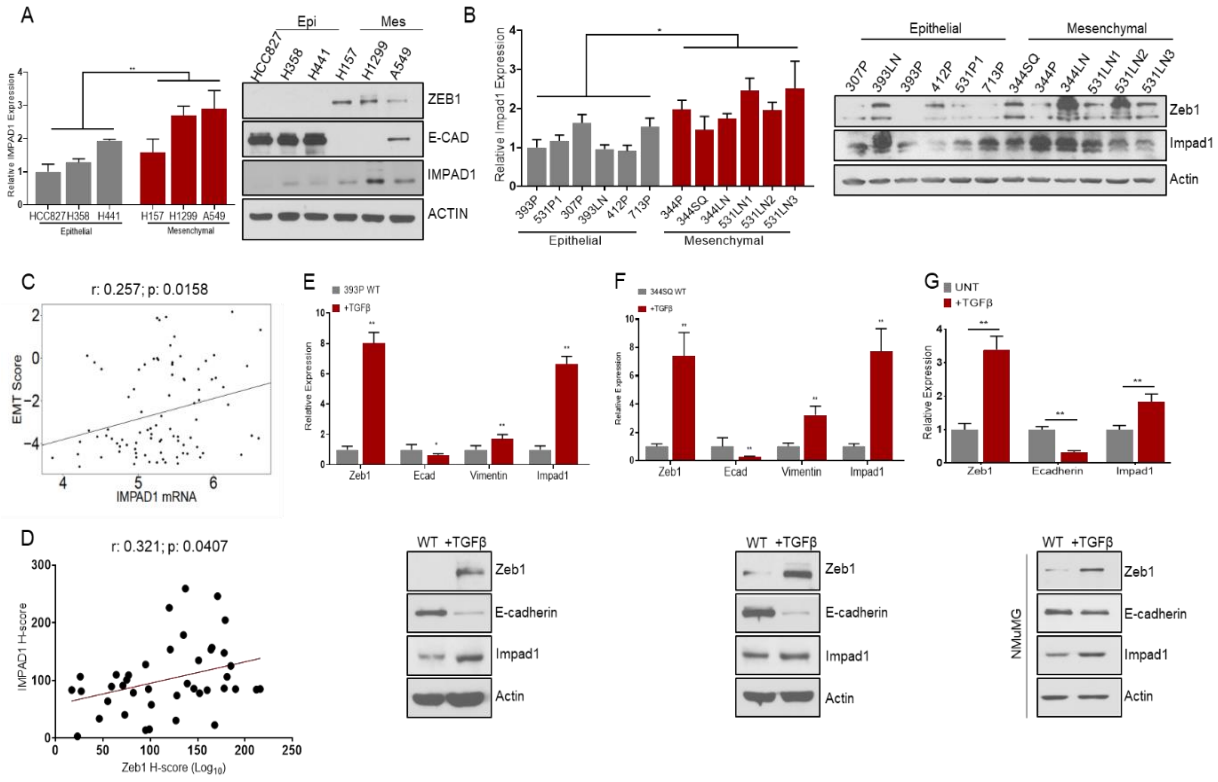

Figure 4-1. Impad1 is upregulated during EMT to promote tumorigenesis. A, B. *qPCR (left) and western blot (right) analysis for Impad1 mRNA and protein in human (A) and mouse (B) NSCLC models stratified based on their EMT status.* ***C.*** *Correlation of IMPAD1 mRNA with EMT status of NSCLC cell lines (Spearman Rho: 0.257; P-value: 0.0158).* ***D.*** *Correlation of IMPAD1 protein staining with ZEB1 protein levels in human NSCLC whole tissue sections (Spearman Rho: 0.321; P-value: 0.0407).* ***E-G.*** *Impad1 mRNA (above) and protein (below) expression during TGFβ-induced (5ng/mL, day 6) EMT in*

*murine KP 393P (E) and 344SQ (F), and mammary epithelial NMuMG (G) cells. Zeb1 and E-cadherin levels are included as markers for EMT. Actin was used as loading control. Data represented as mean of triplicates ± SD. Significance by Student's T-test. P-value<0.05 - *; <0.002 - **. See also Figure 4-3.*

4.2 Impad1 is a novel target of epithelial miRNAs miR-200 and miR~96

Our group and others have shown that Zeb1, and epithelial miRNAs such as the miRNA-200 family (miR-200) and the miR182~96~182 cluster (miR~96) are part of a double-negative feedback loop that regulates EMT in cancer (P. A. Gregory et al., 2008; Kundu et al., 2016). I have also demonstrated that Zeb1 positively correlates with EMT in the previously described murine and human cancer models, whereas miR-200 and miR~96 show a negative association. Oncogenes such as Zeb1 and Foxf2, which are targets of the epithelial miRNAs, are de-repressed upon loss of these miRNAs during EMT, thus driving invasion and metastasis (Gibbons, Lin, Creighton, Rizvi, et al., 2009; Kundu et al., 2016; Larsen et al., 2016). Hence, I questioned a similar modulation of Impad1 in our system during EMT. An *in silico* analysis identified multiple well-conserved miR-200 and miR~96 seed sequences in the Impad1 3'UTR **(Figure 4-4A)**. Additionally, Bracken et al. discovered Impad1 as a direct target of miR-200b using an Ago-HITS-CLIP pulldown in breast cancer cells (Bracken et al., 2014). To investigate this in lung cancer, I used doxycycline-inducible models where Zeb1 drives EMT in epithelial 393P (murine) and H441 (human) lung cancer cells, and miR-200 or miR~96 individually induce mesenchymal-to-epithelial transition (MET) in mesenchymal 344SQ (murine) and H157 (human) cells (D. H. Peng et al., 2019). Like Zeb1, Impad1 was repressed during miR-200- or miR~96-mediated MET and

enhanced upon Zeb1-mediated EMT **(Figure 4-2A-D, Figure 4-4B-D)**. Next, I studied this mode of regulation of Impad1 in genetically-engineered mouse models (GEMMs) of lung adenocarcinoma that closely resemble disease progression in humans. We developed conditional miR-200 or miR~96 floxed mice and crossed them with a conditional activating mutation in KRAS ($KRAS^{G12D/+}$) to produce $KRAS^{G12D/+}$;miR-$200c^{-/-}$ (KM200), $KRAS^{G12D/+}$;$p53^{-/}$;miR-$200c^{-/-}$ (KPM200), and $KRAS^{G12D/+}$;miR~$96^{-/-}$ (KM96) animals with lung tumors that undergo EMT as indicated by high Zeb1 and low E-cadherin levels **(Figure 4-4E)** (D. H. Peng et al., 2019). Impad1 was upregulated in KM200, KM96, and KPM200 tumors compared to the KRAS ($KRAS^{G12D/+}$) and KP ($KRAS^{G12D/+}$;$p53^{-/-}$) tumors as quantified by IHC **(Figure 4-2E, Figure 4-4E)**. Additionally, cell lines derived from KPM200 tumors that are more mesenchymal compared to the KP epithelial cells also showed higher Impad1 expression **(Figure 4-4F-H)**. Next, I also investigated this miRNA-mediated suppression of Impad1 in the previously mentioned human NSCLC cell line (McMillan et al., 2018) and tumor (TCGA-Firehose legacy) datasets. Impad1 negatively correlated with miR-200 family members and miR-96 **(Figure 4-2F, G, Figure 4-4I-N)**.

Lastly, to ascertain whether Impad1 is directly targeted by miR-200 and miR~96, I performed a 3'UTR luciferase reporter assay with the Impad1 3'UTR containing the wild-type or mutant miRNA seed sequences. Both miR-200b/c and miR-96/183 significantly repressed luciferase activity, which was rescued when the miRNA binding sites were mutated **(Figure 4-2H, I, Figure 4-4O, P)**; indicating that Impad1 is a direct target of miR-200b/c and of miR-96/183. Thus, our data established that Impad1 is upregulated during EMT upon loss of epithelial miRNAs miR-200 and

miR~96. However, no change was observed in the EMT status of the cells upon Impad1 overexpression or knockdown; hence signifying that it does not mediate EMT **(Figure 4-5)**.

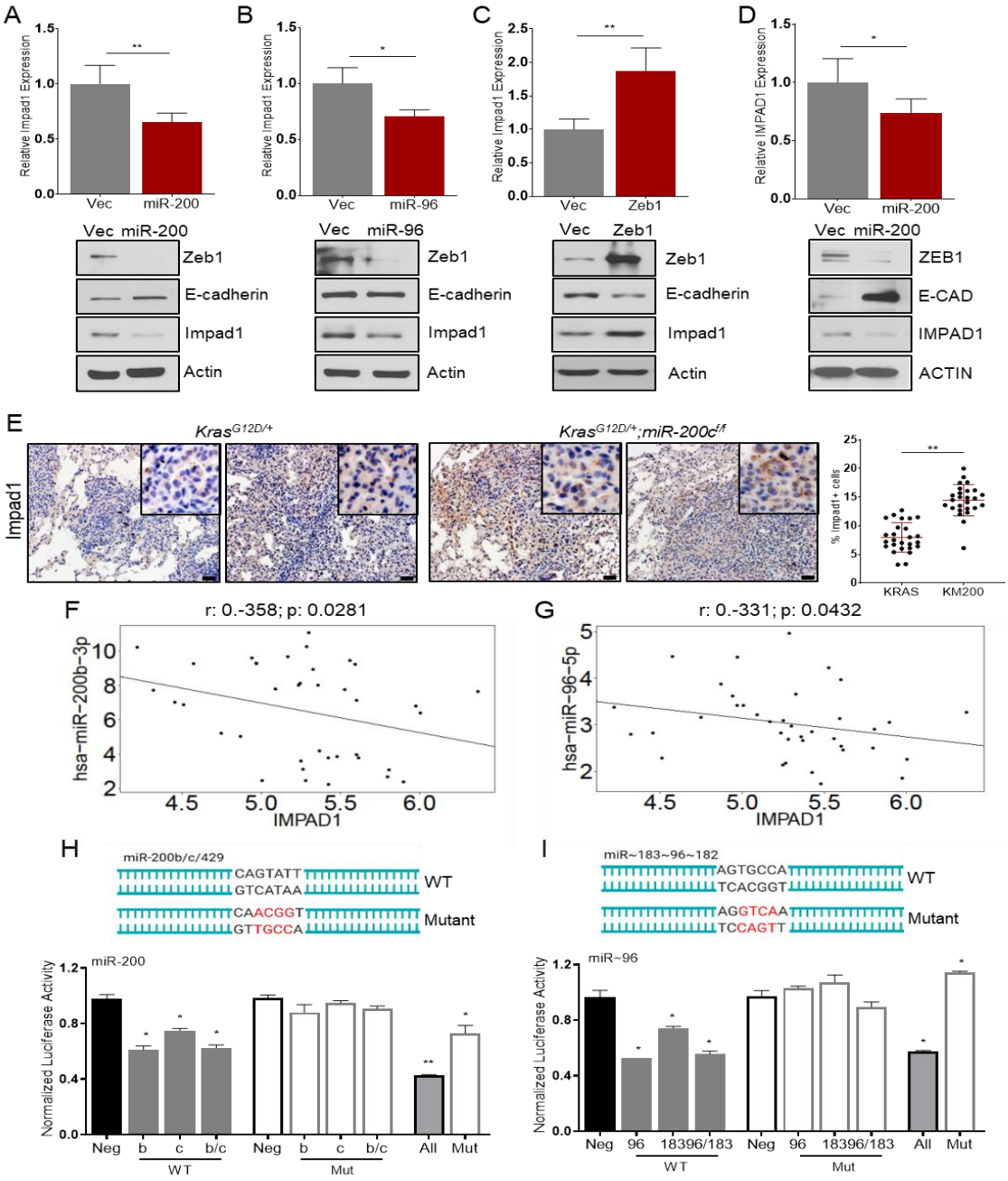

Figure 4-2. Impad1 is a novel target of epithelial miRNAs miR-200 and miR~96. A-D. *Impad1 mRNA (top) and protein (bottom) expression upon miR-200 (A) or miR~96-induced (B) MET in 344SQ,*

Zeb1-induced EMT in 393P (C), and miR-200-induced MET in human mesenchymal lung cancer cells (H157 – D) (Doxycycline - 2μM, 96 hrs). ***E.*** *IHC staining and quantification for %Impad1+ cells in GEMM lung tumors (KRAS vs. KM200). N=27 (9 images/tumor). (scale bar: 20uM)* ***F, G.*** *Correlation of Impad1 with miR-200b (F – Spearman Rho: -0.358; P-value: 0.0281) or miR-96 (G – Spearman Rho: -0.331; P-value: 0.0432) in human NSCLC cell lines.* ***H, I.*** *Schematic representation of the wildtype or mutant miRNA target sites in Impad1 3'UTR (Top). Normalized luciferase reporter activity upon co-expression of either mouse control miRNA mimic or mimics for miR-200b, and miR-200c (H), or mimics for miR-96, and miR-183 (I) in 393P WT cells. 60 pmol mimics were used individually or in combination. Data are represented as mean ± SD. Significance by Student's T-test. P-value<0.05 - *; <0.002 - **. See also Figure 4-4.*

4.3 Discussion and conclusions

EMT is an initiating step in the metastatic cascade that regulates downstream cellular processes to drive malignancy (Kalluri & Weinberg, 2009; Thiery et al., 2009). Zeb1 and epithelial miRNAs like miR-200 and miR~96 are key mediators of EMT during cancer (Gibbons, Lin, Creighton, Rizvi, et al., 2009; P. A. Gregory et al., 2008). However, inhibiting EMT and metastasis by disrupting Zeb1, or introducing epithelial miRNAs into the cells has been challenging due to the pervasive roles of these drivers in cellular pathways (Nieto et al., 2016). Thus, identifying key oncogenes that are de-repressed upon loss of the miRNAs during EMT and cancer progression holds therapeutic potential.

In this chapter I identified one such oncogene, Impad1, which is a direct target of both miR-200 and miR~96, and is upregulated in mesenchymal, malignant lung cancer cells due to loss of the miRNAs. Interestingly, although Impad1 was regulated during EMT, overexpression or knockdown of the gene had no effect on the process,

indicating a linear epistatic pathway. Thus, unlike targeting Zeb1, inhibiting Impad1 would not have off-target effects that alter other EMT-mediated processes, which are essential for cell survival. In breast cancer, Parris et al. have shown that Impad1 is syntenic and co-amplified with Myc (Parris et al., 2014). Moreover, they also ascertained that the 8q12.1-q24.22 genomic region, which includes Impad1, is hypomethylated and associates with aggressive breast cancers. This signifies another mechanism-of-regulation of Imapd1, which was not explored by us, and could give further insight into the role of Impad1 in cancer progression.

The other hit from the invasion screen that I followed up on was Kdelr2. Chapter 3 determines that like Impad1, Kdelr2 is sufficient and necessary to drive lung cancer invasion and metastasis. However, unlike Impad1, Kdelr2 was not a target of the epithelial miRNAs, miR-200 and miR~96, and showed no association with EMT **(Figure 5-11, Figure 5-12)**. Previous work has demonstrated that Kdelr2 can be auto-activated upon upregulation (Ruggiero et al., 2015; Ruggiero et al., 2018). Thus, I posit that increased expression of Kdelr2 during cancer is sufficient to drive the feedback mechanism that upregulates and activates Kdelr2 function. However, detailed studies investigating the mode-of-regulation of Kdelr2 might help further unravel the intricacies of metastasis.

4.4 Supplement data

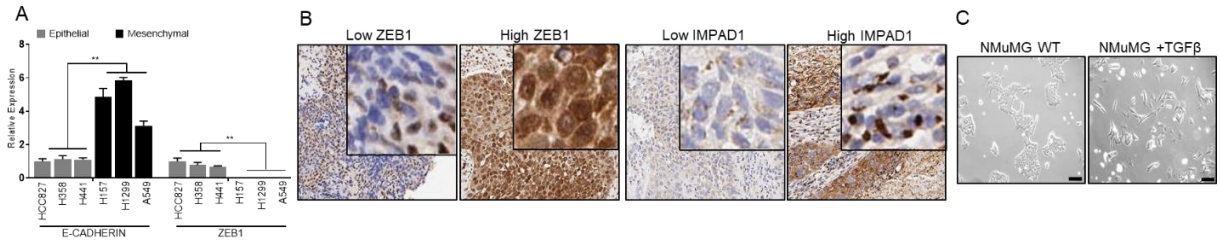

Figure 4-3. Impad1 is upregulated during EMT to promote tumorigenesis. A. *mRNA levels for Zeb1 and E-cadherin in human NSCLC cell lines stratified based on their EMT status.* ***B.*** *IHC staining for ZEB1 or IMPAD1 in NSCLC whole sections from TMA3.* ***C.*** *Representative images of TGFβ-treated NMuMG cells undergoing EMT (5ng/mL, day 11). (scale bar: 100uM). Data are represented as mean ± SD. Significance by Student's T-test. P-value<0.05 - *; <0.002 - ***

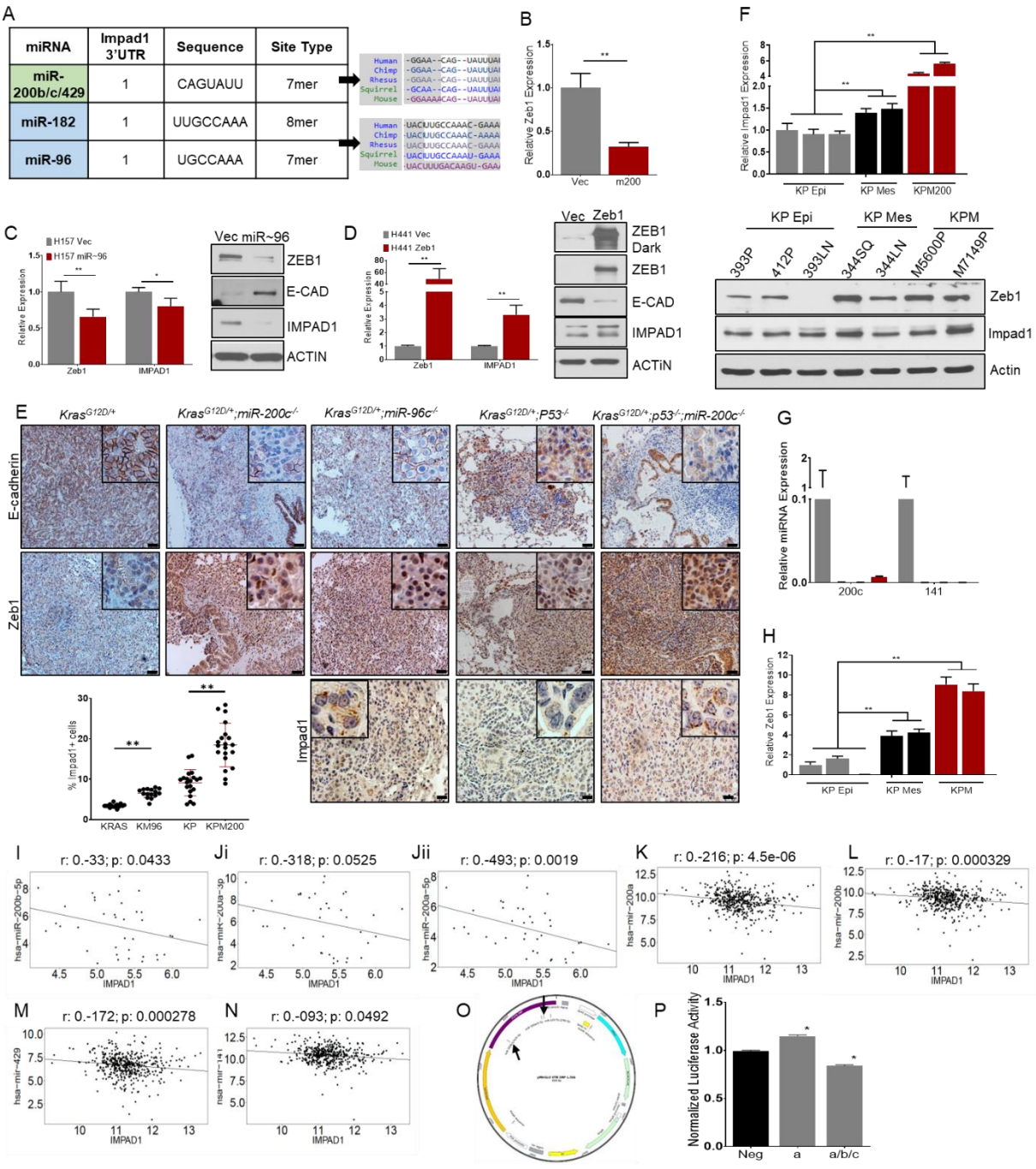

Figure 4-4. Impad1 is a novel target of epithelial miRNAs miR-200 and miR~96. A. *In silico analysis using TargetScan shows number of, type of, and conservation level of target sites for miR-200 and miR~96 in Impad1 3'UTR.* ***B.*** *Zeb1 mRNA expression upon miR-200 induction in human mesenchymal lung cancer cells (H157) (Doxycycline - 2μM, 96 hrs).* ***C, D.*** *Impad1 mRNA (left) and protein (right) levels during miR~96-mediated MET (C) and Zeb1-induced EMT (D) (Doxycycline - 2μM, 96 hrs).* ***E.*** *IHC staining for Zeb1, E-cadherin, and Impad1 in GEMMs for EMT (KRAS, KP, KM200, KM96,*

KPM200). N=15 (KRAS, KM96) N=20 (KP, KPM2000). Quantification for percent Impad1+ cells in lung tumors shown below. (Zeb1/E-cadherin scale bar: 50uM) (Impad1 scale bar: 20uM) ***F-H.*** *Impad1 in (F), miR-200 (G), and Zeb1 (H) in cell lines derived from KP epithelial (KP epi), KP mesenchymal (KP mes), and KPM200 tumors. High Zeb1 and low E-cadherin levels were used as markers for EMT. Actin was used as loading control.* ***I-N.*** *Correlation of Impad1 with respective miRNA family/cluster members in human NSCLC cell lines (UTSW dataset, I-Jii) and tumors (TCGA-LuAd, K-N). Spearman's correlation was used for analysis.* ***O.*** *Map for pMirGlo plasmid used for 3'UTR luciferase reporter assay.* ***P.*** *Normalized luciferase reporter activity upon expression of either mouse control miRNA precursor (60 pmol), only miR-200a precursor (60 pmol), or precursors for miR-200a/b/c (20/20/20 pmol) in 393P WT cells. Data represented as mean ± SD. Significance by Student's T-test. P-value<0.05 - *; <0.002 - ***

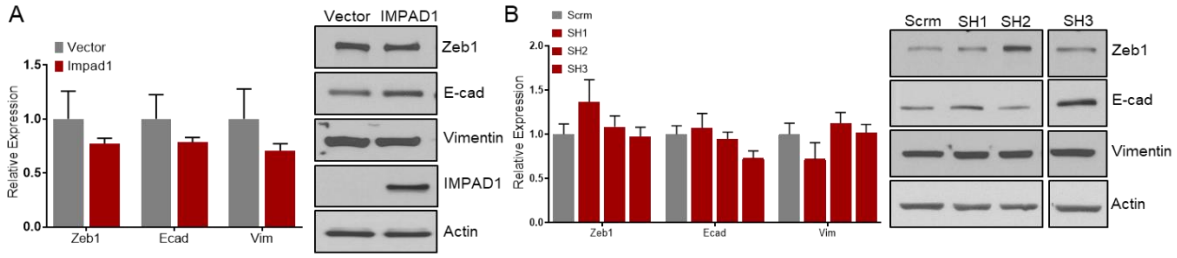

Figure 4-5. Impad1 does not regulate EMT. A, B. *Impad1 overexpression (A) or knockdown (B) does not alter EMT status of cancer cells. Zeb1, E-cadherin, and Vimentin used as EMT markers. Actin used as loading control.*

Chapter 5: Enhanced Golgi exocytosis alters the TME to drive metastasis

Contents of this chapter including figures are derived from the publication Bajaj R, Kundu ST, Grzeskowiak CL, Fradette JJ, Scott KL, Creighton CJ, Gibbons DL. "Impad1 and Kdelr2 drive invasion and metastasis by enhancing Golgi-mediated secretion." *Oncogene*. 2020 Aug 04. PubMed PMID: 32753652 with approval from Nature Publishing Group.

5.1 Impad1 regulates Golgi-mediated exocytosis to drive lung cancer invasion

Impad1 is amplified in lung adenocarcinoma, and literature suggests that its loss disrupts GAG deposition in the bone and cartilage ECM (Frederick et al., 2008; Parris et al., 2014; Plasterer et al., 2019; Sohaskey et al., 2008; Vissers et al., 2011). However, little is known about the role of Impad1 upregulation in Golgi-mediated secretion, as well as in lung cancer invasion and metastasis.

First, I ascertained the localization of Impad1 to the specific Golgi compartment in our murine and human models by fractionation, and co-immunofluorescence (co-IF) assays with a *cis*-Golgi marker (GM130) or a *trans*-Golgi marker (Golgin97) **(Figure 5-1A, Bi, Figure 5-17)** (Frederick et al., 2008; Halberg et al., 2016; Nakamura et al., 1995; Tan et al., 2017). Co-localization analysis (the COLOC2 analysis in ImageJ) concluded that Impad1 resides in both the *cis* and the *trans* Golgi compartments **(Figure 5-1Bii)**. This specified the spatially dynamic role of Impad1 as

it shuttles between the compartments during vesicular trafficking. Furthermore, Brefeldin A (BFA – 1μM, 6 hours) treatment, which disrupts Golgi stacking (Bershadsky & Futerman, 1994), also abrogated Impad1 signal indicating that its localization to the Golgi is dependent on appropriate organelle formation **(Figure 5-1C, Figure 5-17)**. Hence, I hypothesized that Impad1 drives invasion and metastasis by altering Golgi functions and the exocytosis of components that form the TME.

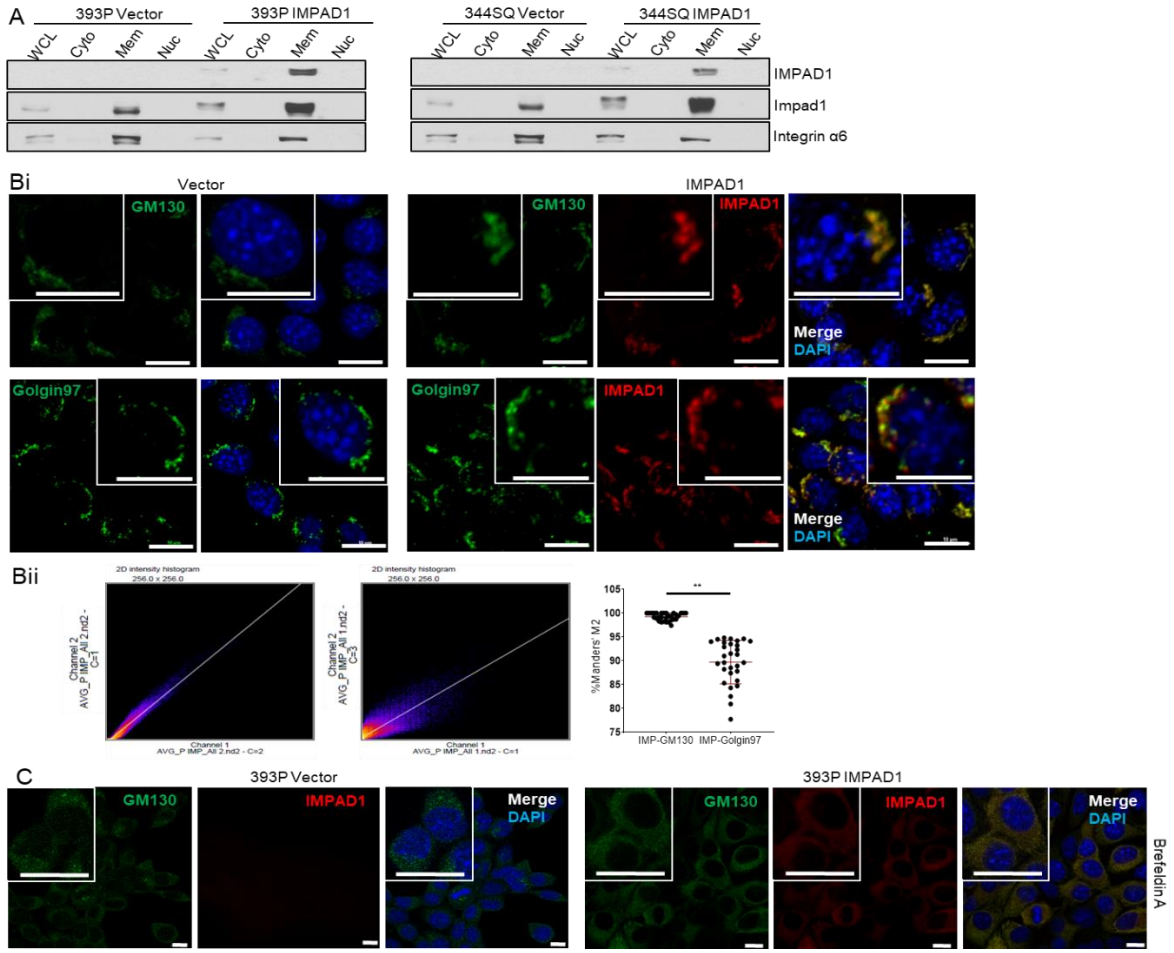

Figure 5-1. Impad1 localizes to the cis- and trans-Golgi compartments. A. *Fractionation assay with 393P and 344SQ IMPAD1 overexpressing cells demonstrate that endogenous and exogenous Impad1 is primarily in the membrane fraction. Integrin α6 was used as the loading control for the membrane fraction. WCL – whole cell lysate, Cyto – cytoplasmic fraction, Mem – membrane fraction, Nuc – nuclear and cytoskeletal fraction.* ***Bi, ii.*** *Co-IF staining for GM130 (above) or Golgin97 (below) (green) and*

IMPAD1 (red) in 393P vector or IMPAD1 overexpressing cells (i). Nucleus counter-stained with DAPI. ImageJ COLOC2 analysis for co-localization of Impad1 with GM130 (cis-Golgi) or Golgin97 (trans-Golgi). %Mander's M2 co-localization shown below (ii). ***C.*** *Co-IF staining for GM130 and IMPAD1 upon Brefeldin-A (1μM 6 hours) treatment. See also Figure 5-17.*

To test the hypothesis, I performed a secretome-mediated invasion assay by seeding non-invasive 393P parental cells in conditioned media collected from the vector- or IMPAD1-inducible cells with or without BFA treatment **(Figure 5-2A)**. Conditioned media (CM) from IMPAD1 overexpressing cells significantly increased the invasiveness of the 393P cells, which was reversed upon BFA treatment. This indicated that Impad1 enhances Golgi-regulated exocytosis of invasive components. **(Figure 5-2C, Figure 5-18A)**. As proof-of-principle, I probed for MMPs in the conditioned media collected from IMPAD1 overexpressing and knockdown cells. Secretion of MMP1, 2, and 9 was regulated by Impad1 levels, which were confirmed in the whole cell lysate **(Figure 5-2F, Figure 5-18E)**. However, MMP transcription was not consistently altered by Impad1, indicating that MMP secretion is regulated by the protein at the post-translational level **(Figure 5-18F, G)**. Next, I investigated whether the secreted MMPs were responsible for Impad1-mediated invasion. I performed a similar secretome invasion assay but treated the CM with a pan-MMP inhibitor, Ilomastat **(Figure 5-2B)**. Once again, CM from IMPAD1 -overexpressing cells was sufficient to promote invasion, which was suppressed upon Ilomastat treatment **(Figure 5-2D, Figure 5-18B)**. I then recapitulated this phenotype in a 3D Matrigel/collagen matrix, where cells overexpressing IMPAD1 lost their invasive ability upon MMP inhibition **(Figure 5-2E, Figure 5-18C, D)**. Thus, I have established that Impad1 modulates Golgi-mediated secretion of proteases such as MMPs into the

extracellular space to promote lung cancer migration and invasion. Interestingly, the 3D invasion assay demonstrated only a partial suppression of Impad1-mediated invasive structures upon MMP inhibition **(Figure 5-2E)**. Thus, I hypothesized that Impad1 also secretes other factors that can make the ECM and TME conducive for cancer cell invasion and metastasis.

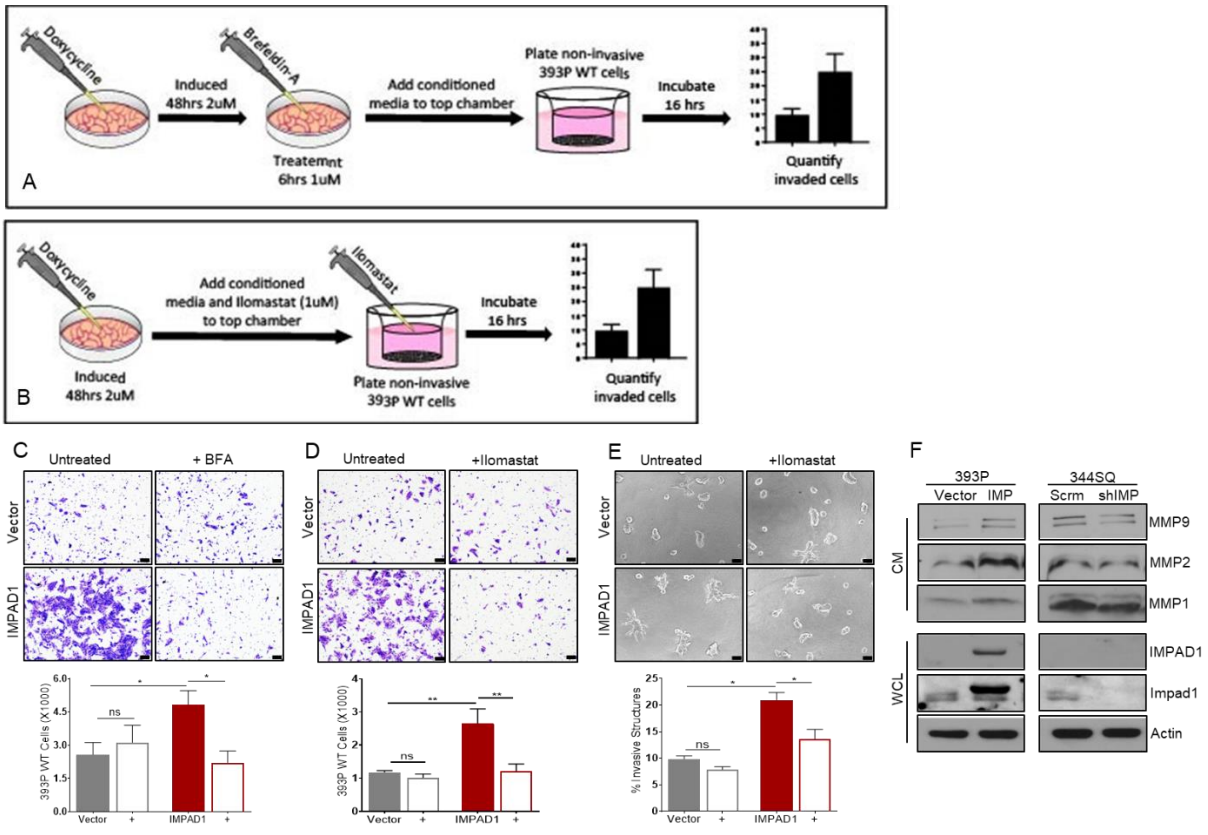

Figure 5-2. Impad1 regulates Golgi-mediated exocytosis of MMPs to drive lung cancer cell invasion. A, B. *Schematic workflow for secretome-mediated invasion assay – 24 hour-conditioned media (CM) was collected from cells that were doxycycline-induced for 48 hours. This CM with or without BFA (A) or Ilomastat (B) treatment was used to replenish the non-invasive parental 393P WT cells that were plated in Boyden chambers. After 16 hours of incubation, cells that invaded through the chambers were quantified to determine effect of the secretome on invasiveness of cells.* ***C, D.*** *Secretome-mediated invasion assay quantifying invasiveness of 393P WT cells replenished with CM from 393P vector or IMPAD1 overexpressing cells upon treatment with BFA, a Golgi secretion inhibitor*

(1uM 6 hours) (C), or Ilomastat, an MMP inhibitor (1uM) (D) (scale bar: 100 μM). ***E.*** *Invasive structures formed upon IMPAD1 overexpression in 3D collagen/Matrigel matrix (1.5mg/ml) with Ilomastat treatment (1uM).* ***F.*** *Western blot analysis for MMPs 1, 2, and 9 in CM from IMPAD1 overexpressing and knockdown cells. Whole cell lysate (WCL) confirms IMPAD1 overexpression and knockdown. Data are represented as mean ± SEM. Significance by Student's T-test. P-value<0.05 - *; <0.002 - **. See also Figure 5-18.*

5.2 Impad1 alters the secretome of lung cancer cells undergoing EMT

Mesenchymal cancer cells differentially secrete proteins compared to epithelial cells; hence, EMT may drive malignancy by orchestrating the secretome changes that regulate the ECM and the TME. Reka et al. performed GeLC-tandem mass spectrometry and identified the secretome signature for cancer cells undergoing TGFβ-induced EMT, which predicted for patient survival (Reka et al., 2014). Additionally, our lab has shown that Zeb1-mediated EMT enhances collagen deposition, which is associated with cancer metastasis and poor patient survival (D. H. Peng et al., 2017; Ungewiss et al., 2016). However, there is still a gap in understanding the comprehensive secretome of lung cancer cells undergoing EMT or how Golgi-resident proteins like Impad1 affect these changes in the secretome.

Hence, I investigated if Impad1 plays a role in altering the secretome of lung cancer cells during EMT. I performed liquid chromatography-mass spectrometry (LC-MS/MS) analysis on the CM collected from the epithelial 393P vector and Impad1 overexpressing, as well as the mesenchymal 344SQ scramble control and Impad1 knockdown cells. I triangulated hits that were higher in Impad1 overexpressing cells

compared to the vector control, lower in Impad1 knockdown cells compared to the scramble control, and higher in mesenchymal 344SQ scramble control compared to the epithelial 393P vector control **(Figure 5-3A**, **Table 5-1**). This unbiased approach identified approximately 150 proteins (≥2 peptides per protein, 1% false discovery rate) that were enhanced in the secretome of Impad1 overexpressing cells. Of these candidates, 43 (B+D) were decreased upon Impad1 knockdown, and 130 (A+D) were upregulated during EMT. This high level of overlap of the extracellular components between the Impad1 overexpressing and the mesenchymal cells suggested a role of Impad1 in regulating the enhanced secretion observed during EMT. However, I focused on the 32 (D) proteins that were common across all three comparisons, which included extracellular factors that have key roles in promoting cancer: collagen (Col12α1), heparanase (Hpse), Sortilin receptor (Sorl1), Keratin (Krt5), Glycohydrolases (Parg), etc. Of these, I further studied collagen because loss of Impad1 has been associated with decreased bone and cartilage ECM formation during diseases such as chondrodysplasia (Frederick et al., 2008; Sohaskey et al., 2008; Vissers et al., 2011). Additionally, I have previously shown that EMT enhances collagen deposition in the ECM, thereby driving lung cancer metastasis (D. H. Peng et al., 2017; Ungewiss et al., 2016). Hence, I investigated if Impad1 upregulation during EMT is responsible for promoting collagen deposition in the TME. I probed for collagen in the syngeneic metastatic tumors overexpressing or the non-metastatic tumors with suppression of Impad1, by using Masson's Trichrome and second harmonic generation (SHG) microscopy **(Figure 5-3B, C)**. The data indicated that Impad1 regulates the exocytosis and deposition of collagen proteins both *in vitro* and

in vivo, to alter the ECM and drive invasion and metastasis. Lastly, Impad1 was also posited to alter another component of the bone and cartilage ECM, the GAGs (Frederick et al., 2008; Sohaskey et al., 2008; Vissers et al., 2011). Given the role of heparanase in regulating glycoproteins, I determined the modulation of GAGs by Impad1. Using Alcian blue staining, I ascertained that GAG deposition in tumors significantly correlated with Impad1 expression **(Figure 5-19)**. Thus, the data demonstrates that Impad1 alters the tumor ECM to promote metastasis.

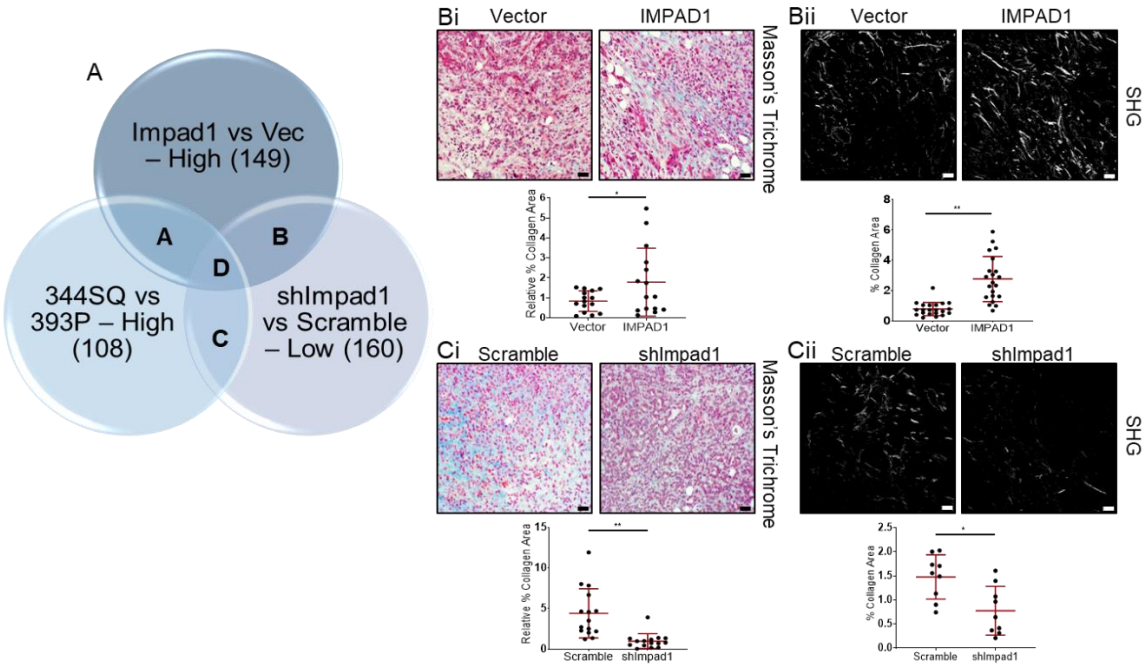

Figure 5-3. Impad1 alters the secretome of lung cancer cells undergoing EMT. A. *Venn diagram depicting comparison of LC-M/MS hits from conditioned media collected from 393P IMPAD1 overexpressing cells, mesenchymal 344SQ cells, and 344SQ shImpad1 cells.* ***B, C.*** *Masson's trichrome staining (i) and Second Harmonic Generation microscopy (SHG) (ii) detecting collagen in 344SQ vector or IMPAD1 overexpressing (B), and 344SQ scramble or shImpad1 knockdown (C) syngeneic tumors (scale bar: 50uM). Data are represented as mean ± SD. Significance by Student's T-test. P-value<0.05 - *; <0.002 - **. See also Table 5-1.*

Our group has previously shown that collagen suppresses the immune microenvironment to drive metastasis and therapy resistance (D. H. Peng et al., 2020). Therefore, I wanted to study if Impad1 could also modify the immune landscape of the TME. I performed multiparameter flow cytometry analysis for the CD4+, CD8+ T cells, as well as the antigen-presenting cells (APCs) in the syngeneic tumors with IMPAD1 overexpression or knockdown. Despite no consistent change in the APC populations **(Figure 5-20A, B)**, Impad1 expression mediated an immunosuppressive microenvironment as depicted by decreased CD4+ and CD8+ effector T cells **(Figure 5-4A, Figure 5-20C)**. Interestingly, I found that this phenotype could be reversed by Impad1 knockdown, which led to a significant increase in the effector T cell populations **(Figure 5-4B, Figure 5-20D)**. Hence, the data establishes Impad1 as a key regulator of the cancer cell secretome, producing changes in the ECM and the immune microenvironment.

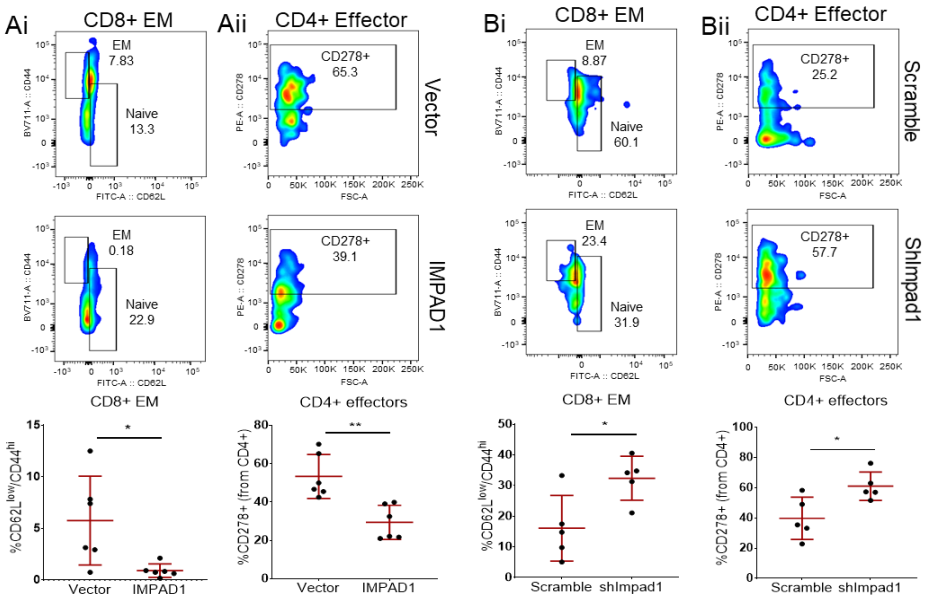

Figure 5-4. Impad1 promotes immunosuppression by repressing anti-tumor immune population to drive metastasis. A, B. *Dot plots and representative FACS plots for CD8+ (i), CD4+ (ii) effector T*

*cells in 344SQ vector and IMPAD1 overexpressing (A), as well as 344SQ scramble and shImpad1 knockdown (B) syngeneic tumors. Data are represented as mean ± SD. Significance by Student's T-test. P-value<0.05 - *; <0.002 - **. See also Figure 5-20.*

5.3 Impad1 alters Golgi morphology and trafficking

Next, I ascertained the mechanism by which Impad1 regulates the cancer cell secretome and the TME. Given that Impad1 has been established as a Golgi-resident protein (Bajaj et al., 2020; Frederick et al., 2008; Vissers et al., 2011), I investigated its role in controlling Golgi dynamics. Zeb1-mediated EMT drives a more compact Golgi organelle, which is disrupted in the epithelial state (Tan et al., 2017). Hence, I determined whether the EMT-driven alterations in Golgi morphology can be regulated by Impad1. I probed for the Golgi using GM130 and Golgin97 in epithelial 393P cells overexpressing Impad1, and mesenchymal 344SQ cells with Impad1 knockdown. Impad1 expression produced an organized and stacked Golgi in 393P and 344SQ cells, as shown by fewer and larger individual Golgi fragments **(Figure 5-5Ai-iii, Bi-iii, Figure 5-21Ai-iii, Bi-iii)**. Despite no change in the expression of the Golgi proteins, GM130 and Golgin97 **(Figure 5-21C)**, Impad1 upregulation also increased the fluorescence staining intensity of the organelle **(Figure 5-5Aiv, Biv, Figure 5-21Aiv, Biv)**. Conversely, Impad1 was necessary to maintain Golgi integrity, where loss of the protein caused Golgi fragmentation demonstrated by scattered, smaller, and more Golgi elements **(Figure 5-6)**. I also confirmed this phenotype in other murine KP NSCLC models: 344P and 344LN with Impad1 knockdown **(Figure 5-22)**.

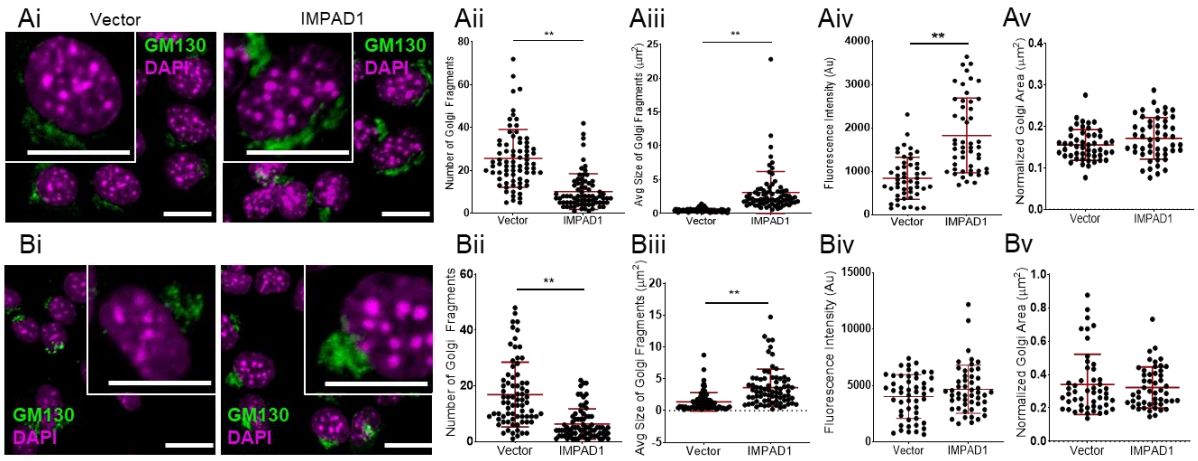

Figure 5-5. Impad1 upregulation promotes Golgi stacking and organization. A, B. *Confocal images of Golgi (GM130, green) and nuclei (DAPI, magenta) in 393P (A) and 344SQ (B) vector or Impad1 overexpressing cells. Scatter plots show number of Golgi fragments/cell N=75 (Aii, Bii), average size of Golgi fragments/cell N=75 (Aiii, Biii), fluorescence intensity of Golgi N=50 (Aiv, Biv), and normalized Golgi area N=50 (Av, Bv). All scale bars: 10uM. Data are represented as mean ± SD. Significance by Student's T-test. P-value<0.05 - *; <0.002 - **. See also Figure 5-21.*

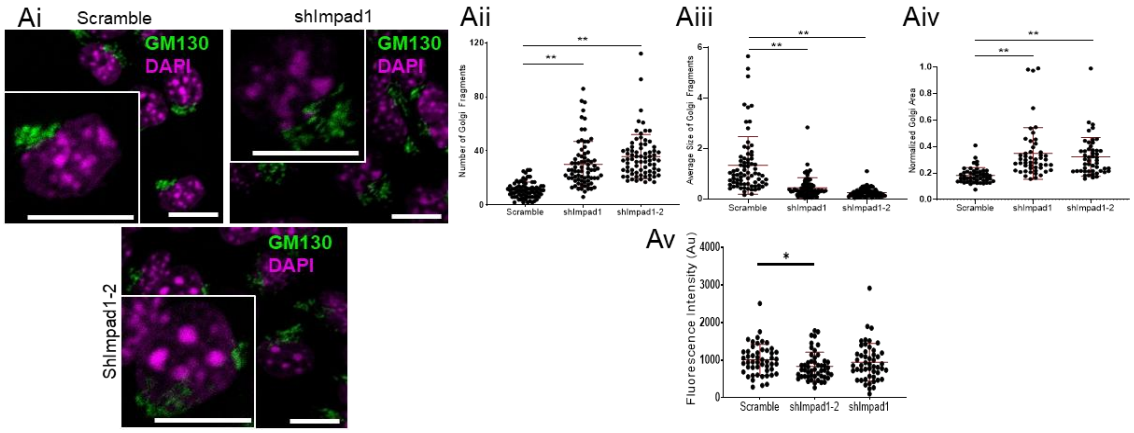

Figure 5-6. Loss of Impad1 disrupts Golgi morphology. A. *Confocal images of Golgi (GM130, green) and nuclei (DAPI, magenta) in 344SQ scramble or Impad1 knockdown cells. Scatter plots show number of Golgi fragments/cell N=75 (Aii), average size of Golgi fragments/cell N=75 (Aiii), fluorescence intensity of Golgi N=50 (Aiv), and normalized Golgi area N=50 (Av). All scale bars: 10uM. Data are represented as mean ± SD. Significance by Student's T-test. P-value<0.05 - *; <0.002 - **. See also Figure 5-22.*

Another aspect of the Golgi that is altered during EMT is vesicular trafficking, which leads to enhanced and polarized exocytosis of factors that can modify the TME and drive metastasis (Tan et al., 2017). To determine if Impad1 can regulate vesicular trafficking, I performed vesicular stomatitis virus-G (VSV-G) trafficking assays on Impad1 overexpressing and knockdown cells **(Figure 5-7)**. Impad1 was necessary and sufficient to promote anterograde trafficking to the plasma membrane in lung cancer cells. These data demonstrate that Impad1 is a functional link between EMT, changes in Golgi secretory dynamics, and the altered metastatic cell secretome.

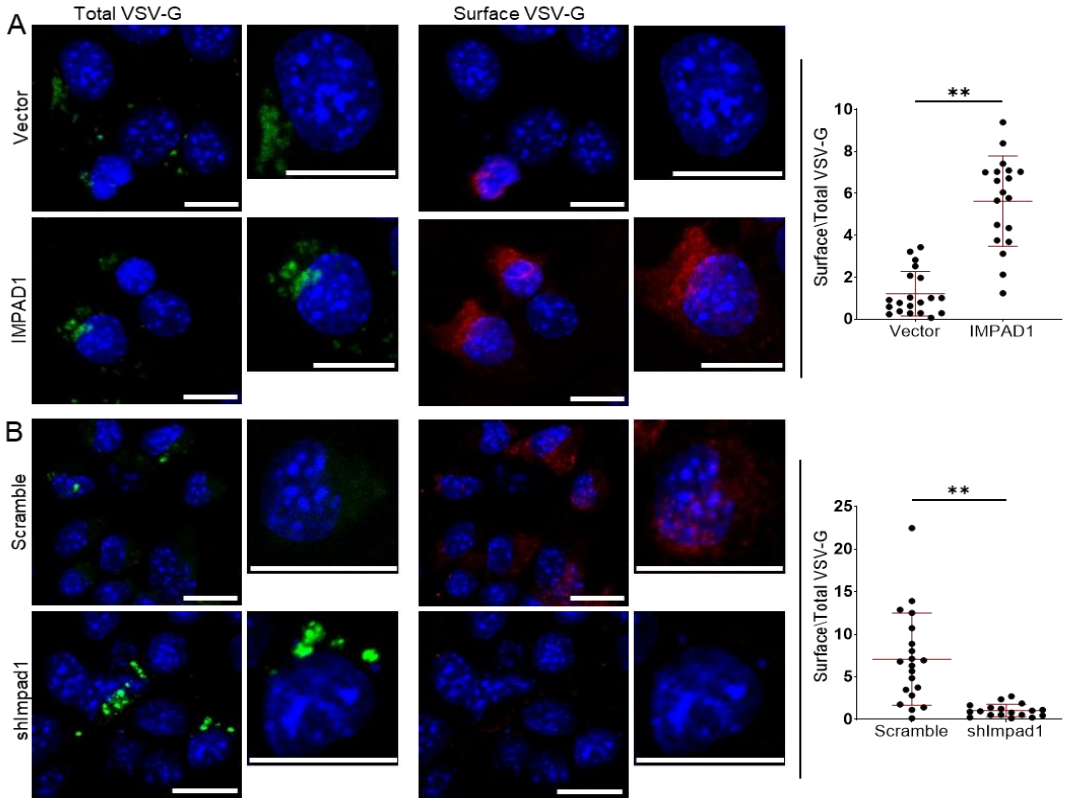

Figure 5-7. Impad1 regulates vesicular trafficking. A, B. *Confocal images of EGFP-VSV-G-transfected 393P vector and Impad1 cells (A), and 344SQ scramble and shImpad1 cells (B) after incubation at the permissive temperature. Total VSVG (green) quantified using EGFP signal intensity, and surface VSV-G (red) was detected by staining non-permeabilized cells with anti-VSV-G antibody. Scatter plots (right) show the ratio of surface to total VSV-G signal intensity/cell. N=20, with statistical*

*outliers removed. All scale bars: 10 μM. Data are represented as mean ± SD. Significance by Student's T-test. P-value<0.05 - *; <0.002 - ***

5.4 Impad1 interacts with another trafficking protein, Syt11, to drive exocytosis and cancer

To understand how Impad1 regulates Golgi functions, I identified the interactome of the protein by using immunoprecipitation-mass spectrometry (IP-MS) in the 393P IMPAD1-Flag overexpressing cells. Using anti-Flag beads, I immunoprecipitated Impad1 and performed MS to detect the interacting proteins. Of the 43 significant hits (p-value<0.05) upregulated upon Impad1 overexpression, I filtered those that showed a >1.5-fold amplification in lung adenocarcinoma (TCGA Firehose Legacy) **(Figure 5-8A, Figure 5-23A, Table 5-2)**. I identified various proteins that are usually exocytosed and function in the extracellular space such as apolipoproteins and the complement pathway factors **(Table 5-2)**. However, to identify the intracellular machinery working with Impad1 to regulate Golgi function, I investigated the two hits annotated to be associated with the Golgi, Syt11 and Arf5. Using co-IP, I first corroborated the interaction between Impad1 and Syt11 or Arf5, individually. Syt11 and Arf5 both validated as Impad1 interacting partners upon an anti-Flag IP in 393P Impad1-Flag overexpressing cells **(Figure 5-8B)**. However, their expression was not dependent on Impad1 levels **(Figure 5-23B)**. Conversely, Syt11 pull down showed an interaction with Impad1 **(Figure 5-8C)**, but not with Arf5 **(Figure 5-23C)**, indicating that Impad1 forms separate bi-partite complexes with the two proteins.

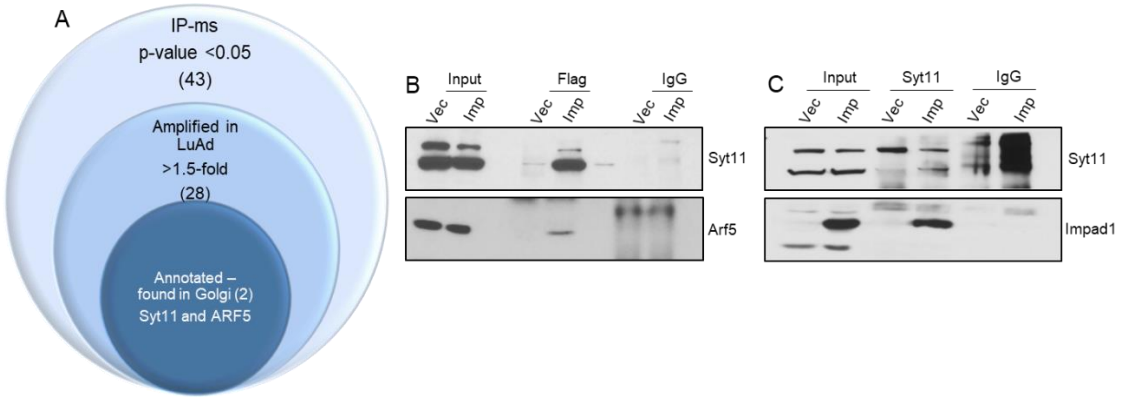

Figure 5-8. Impad1 interacts with trafficking proteins, Syt11 and Arf5. A. *Venn diagram depicting Impad1 interactome identified by IP-MS analysis.* ***B.*** *Probing for Syt11 and Arf5 upon immunoprecipitation of Flag-Impad1 in 393P vector and Impad1 overexpressing cells.* ***C.*** *Co-IP of Syt11 and Impad1 in 393P vector and Impad1 overexpressing cells. See also Table 5-2..*

As part of the Synaptotagmin family, Synaptotagmin XI (Syt11), meditates Ca^{2+}-independent vesicular and membrane trafficking (Mikoshiba, Fukuda, Ibata, Kabayama, & Mizutani, 1999). Previous literature demonstrates that Syt11 plays a critical role in dopamine release by regulating late endocytosis and the vesicle-recycling process (Shimojo et al., 2019). It has also been shown to regulate lysosomal exocytosis and cytokine release primarily in neural cells (Arango Duque, Fukuda, & Descoteaux, 2013; Bento, Ashkenazi, Jimenez-Sanchez, & Rubinsztein, 2016; Du et al., 2017; Wang et al., 2016). However, a role for Syt11 in mediating Golgi exocytosis and promoting cancer metastasis has not been studied. Moving forward, I focused on the Impad1-Syt11 interaction and its function in modulating exocytosis. This is because: (1) In parallel with the *in vitro* screen that first identified Impad1 for its role in promoting lung cancer invasion, I also performed an *in vivo* GOF screen for novel drivers of metastasis (Samrat T. Kundu et al., 2018). Syt11 was identified as an independent driver of NSCLC metastasis in the *in vivo* screen **(Figure 5-9A)**. (2)

Based on the TCGA samples, Syt11 is dysregulated in 19% of lung adenocarcinoma patients, similar to Impad1 (18%) **(Figure 5-24A)**. Furthermore, survival data indicates that co-amplification of Syt11 with Impad1 significantly worsens disease-free survival in patients **(Figure 5-9B)**. No significant change was observed when Syt11 was independently amplified **(Figure 5-24B)**. (3) Similar to Impad1, Syt11 positively correlated with the EMT gene signature and negatively correlated with miR-200 and miR~96 expression in human and murine lung cancer cell lines and tumors **(Figure 5-9C-I, Figure 5-24C-P)**. This indicated that Impad1 and Syt11 are abundant in the mesenchymal cells and may be acting synergistically to alter Golgi dynamics. (4) Lastly, ADP-ribosylation factor 5 (Arf5), the other hit from the IP-MS, helps maintain Golgi integrity upon treatment with drugs that enhance Golgi fragmentation (Ignashkova et al., 2017). I demonstrated that the Impad1-Arf5 interaction was necessary for Impad1-mediated Golgi organization and invasion **(Figure 5-25A, B)**. However, loss of Arf5 did not have any significant effect on the secretome-mediated invasion driven by Impad1 **(Figure 5-25C)**. Thus, going forward I studied the relation between Impad1 and Syt11 to determine the role of Impad1 in regulating exocytosis and the cancer cell secretome.

A

Syt11 hit in *in vivo* gain-of-function metastasis screen	
Gene	SYT11
#Mice	3
#Lungs	6
Avg lung fold change	2.7
#Mice w/ lung fold change	1
%Mice w/ lung fold change	33%

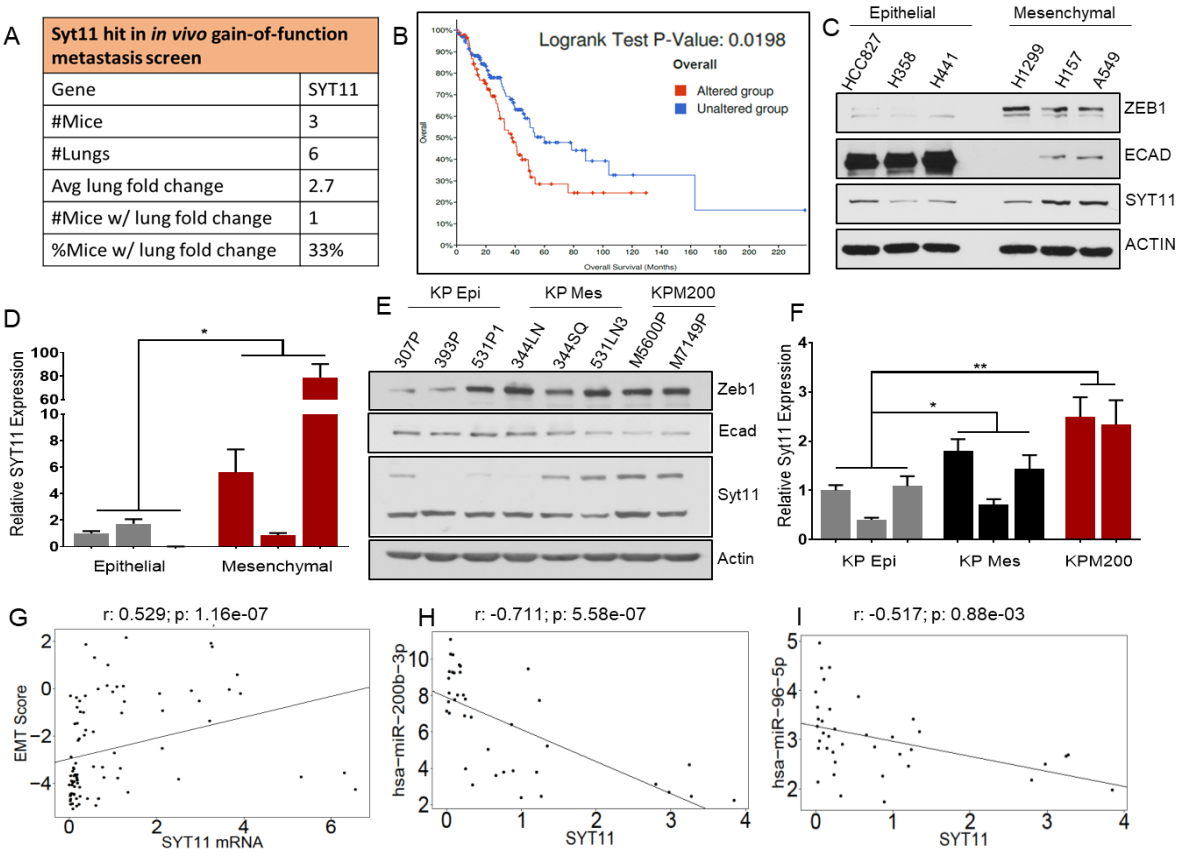

Figure 5-9. Syt11 is upregulated during EMT and worsens lung cancer metastasis and patient survival. A. In vivo *GOF screen identifies Syt11 as a driver of metastasis.* ***B.*** *Kaplan-meier survival plots with or without alterations in Impad1 and Syt11 (cBioPortal – Firehose legacy dataset).* ***C, D.*** *Western blot (C, E) and qPCR (D, F) analysis for Syt11 in human (C, D) and murine (E, F) NSCLC cell lines distinguished on EMT status.* ***G-I.*** *Correlation of Syt11 with EMT score (G – Spearman Rho: 0.529; P-value: 1.16e-07), miR-200b levels (H – Spearman Rho: -0.711; P-value: 5.58e-07), and miR-96 levels (I – Spearman Rho: -0.517; P-value: 0.88e-03) in human NSCLC cell lines. Data are represented as mean ± SD. Significance by Student's T-test. P-value<0.05 - *; <0.002 - **. See also Figure 5-24.*

I first showed that Syt11, like Impad1, is a membrane protein by using a cell fractionation assay **(Figure 5-26A)**. To investigate how the Impad1-Syt11 interaction alters Golgi dynamics, I performed the previously described Golgi morphology and VSV-G vesicular trafficking assays in Impad1 overexpressing cells with or without

transient Syt11 knockdown. Although loss of Syt11 did not affect the ability of Impad1 to regulate Golgi morphology **(Figure 5-26B)**, vesicular trafficking was significantly hampered upon suppression of the gene **(Figure 5-10A)**. Thus, I concluded that the Impad1-Syt11 interaction is necessary for enhanced vesicular trafficking in lung cancer cells. Next, I studied if this loss in trafficking has a functional relevance in inhibiting cancer cell invasion. Using the Boyden chamber invasion assay, I showed that Impad1-mediated invasion was disrupted upon depletion of Syt11 in 393P and 344SQ cells **(Figure 5-10B, C, Figure 5-26C)**. Subsequently, I performed the secretome-mediated invasion assay **(Figure 5-2A)**, by using vector- or Impad1 overexpressing cells with or without Syt11. The invasiveness of the secretome driven by Impad1 was significantly repressed upon loss of Syt11 **(Figure 5-10D)**. I further confirmed these changes by probing for MMP1 and MMP2 in the same CM. Enhanced secretion of MMPs that was observed upon Impad1 overexpression was lost with Syt11 knockdown, as quantified by densitometric analysis using ImageJ **(Figure 5-10E, Figure 5-26D)**. These data specified that Impad1 interacts with Syt11 to enhance vesicular trafficking at the Golgi, thereby secreting invasive components that alter the ECM and the TME.

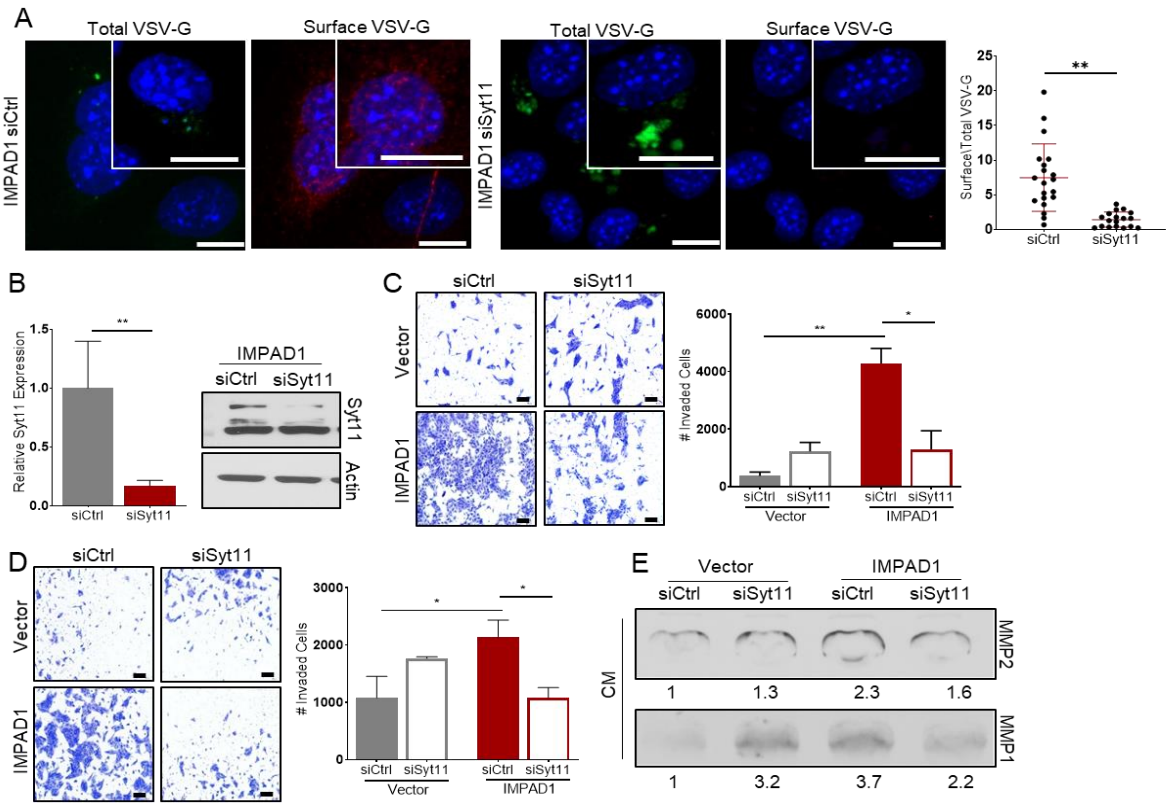

Figure 5-10. Impad1 interaction with Syt11 is necessary to drive exocytosis and invasion in lung cancer. A. *Confocal images of 393P Impad1 overexpressing cells co-transfected with EGFP-VSV-G and siControl or siSyt11 after incubation at the permissive temperature. Total VSVG (green) quantified using EGFP signal intensity, and surface VSV-G (red) was detected by staining non-permeabilized cells with anti-VSV-G antibody. Scatter plots (right) show the ratio of surface to total VSV-G signal intensity/cell. N=20, statistical outliers removed. (scale bar: 10 μM)* ***B, C.*** *mRNA and protein confirmation of siRNA-mediated knockdown of Syt11 in 393P Impad1 overexpressing cells (B). Boyden chamber assay quantifying cell invasion upon siSyt11 in 393P vector or Impad1 overexpressing cells (C). (scale bar: 100 μM)* ***D.*** *Secretome-mediated invasion assay quantifying invasiveness of 393P WT cells replenished with CM from 393P vector or Impad1 overexpressing cells with or without siSyt11. (scale bar: 100 μM)* ***E.*** *Western blot analysis for MMPs 1 and 2 in CM collected from 393P vector or Impad1 overexpressing cells with siControl or siSyt11. Densitometric analysis on the blots was performed using ImageJ. siSyt11 transfections were performed at final concentration 30 nM for ~40*

*hours. Data are represented as mean ± SD. Significance by Student's T-test. P-value<0.05 - *; <0.002 - **. See also Figure 5-26.*

5.5 EMT-independent regulation of Golgi dynamics

As previously mentioned, the other hit from the invasion screen, Kdelr2, is not regulated during EMT in the KP murine cell lines that are distinguished based on their EMT status **(Figure 5-11A)**. Additionally, there was no difference in Kdelr2 expression during Zeb1-mediated EMT, and miR-200- or miR~96-mediated MET **(Figure 5-11B-D)**. Moreover, Kdelr2 did not regulate EMT as no changes were observed in the EMT markers upon Kdelr2 overexpression or knockdown **(Figure 5-12)**.

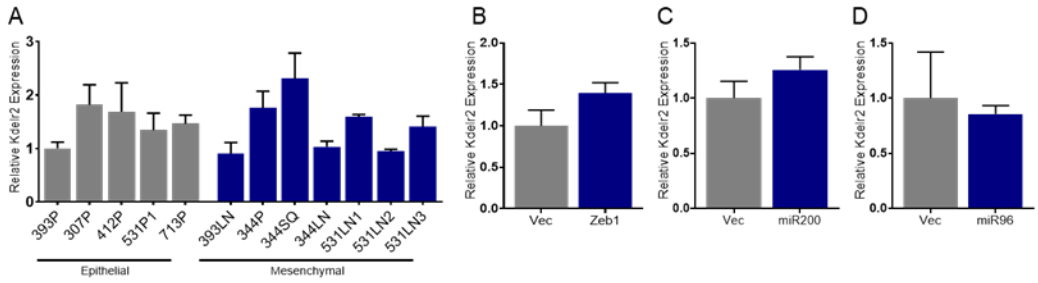

Figure 5-11. Kdelr2 is not regulated during EMT. A. *qPCR analysis for Kdelr2 in murine KP cells stratified based on the EMT status.* ***B-D.*** *Kdelr2 expression upon Zeb1-induced EMT in 393P (B), and miR-200 (C) or miR~96-induced (D) MET in 344SQ murine KP cells (Doxycycline - 2μM, 96 hrs).*

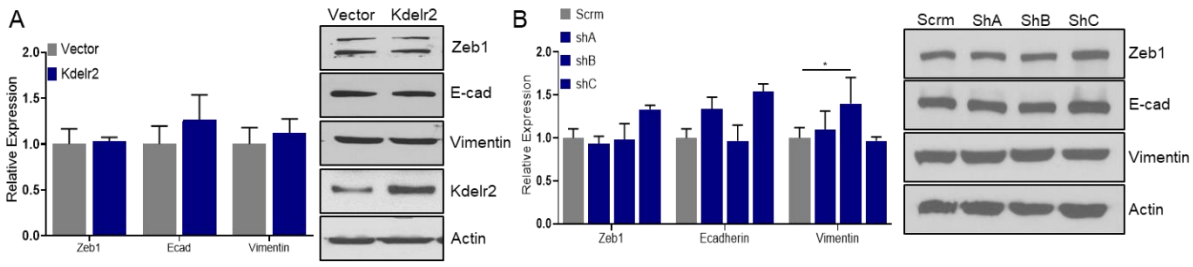

Figure 5-12. Kdelr2 does not regulate EMT. A, B. *Kdelr2 overexpression (A) or knockdown (B) does not alter EMT status of cancer cells. Zeb1, E-cadherin, and Vimentin used as EMT markers. Actin used as loading control.*

However, I demonstrated that Kdelr2 has a similar mechanism-of-action to Impad1, where it regulates Golgi secretion and invasion. In addition to showing that Kdelr2 is a membrane-bound protein **(Figure 5-13A)**, I validated its localization to the ER by using the ER marker, Calnexin **(Figure 5-13Bi, Figure 5-27Ai)**, and to the Golgi by using GM130 **(Figure 5-13Bii, Figure 5-27Aii)** (Taylor et al., 2016). Previous literature indicates that Kdelr2 overexpression auto-activates the protein that then localizes to the ER (Capitani & Sallese, 2009; Wiersma et al., 2015a), which is confirmed by co-IF assays. Furthermore, BFA-mediated disruption of Kdelr2 signal validated that proper Golgi and ER assembly is necessary for accurate protein localization **(Figure 5-13B, Figure 5-27A)**. Therefore, I posited that like Impad1, Kdelr2 is also a part of the ER-Golgi pathway that drives invasion by altering Golgi function and secretion.

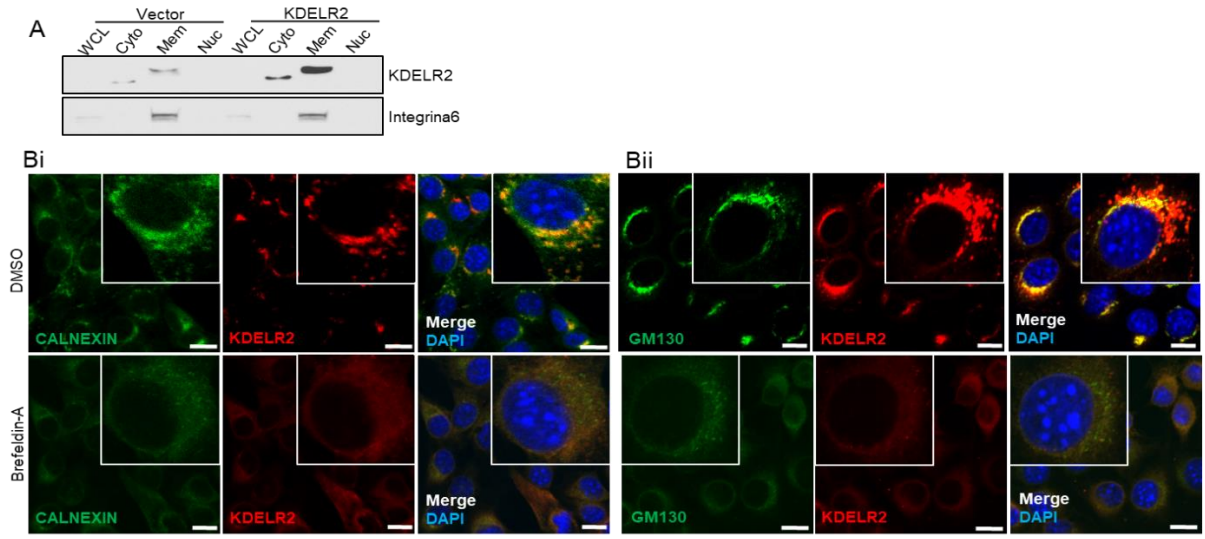

Figure 5-13. Kdelr2 localizes to the ER-Golgi pathway. A *Fractionation assay with 344SQ Kdelr2 overexpressing cells demonstrate protein localization is primarily in the membrane fraction. Integrin α6 was used as the loading control for the membrane fraction. WCL – whole cell lysate, Cyto – cytoplasmic fraction, Mem – membrane fraction, Nuc – nuclear and cytoskeletal fraction.* ***Bi-ii.*** *Co-IF for FLAG-*

KDELR2 (red) and Calnexin (green-i), or GM130 (green-ii) in 393P cells with Kdelr2 overexpression. Cells were treated with DMSO or Brefeldin-A (1uM 4 hours). Nucleus was stained with DAPI. Scale bar for all images:10uM. See also Figure 5-27.

To test this, I performed the previously described secretome-mediated invasion assay **(Figure 5-2A, B)**, which indicated that Kdelr2 enhanced Golgi-mediated secretion of components that make cancer cells more invasive **(Figure 5-14A, Figure 5-28A)**. To identify these components, I probed for MMPs in the CM collected from Kdelr2 overexpressing and knockdown cells, which suggested that Kdelr2 modulated MMP secretion **(Figure 5-14D)**. Furthermore, 2D and 3D invasion assays determined that this MMP secretion was responsible for Kdelr2-mediated invasion **(Figure 5-14B, C, Figure 5-28B-D)**. Previous literature has shown Kdelr2 as a mediator of Src signaling (Ruggiero et al., 2015; Ruggiero et al., 2018), an oncogenic pathway that regulates secretion and alters the ECM to drive lung cancer invasion and metastasis (Padhye et al., 2019). Hence, I also analyzed the Src signaling pathway in the Kdelr2- and Impad1-inducible cells. Increased Src phosphorylation was observed until 2 hours post Kdelr2 induction, after which the pathway was inhibited, possibly by compensatory cellular mechanisms **(Figure 5-14E)**. However, the phenotypic changes observed in Impad1-overexpressing cells could not be attributed to changes in the Src pathway **(Figure 5-28E)**. Hence, the two hits from our invasion screen, Impad1 and Kdelr2, utilized different modes-of-regulation to secrete proteases such as MMPs into the ECM, to promote lung cancer migration and invasion.

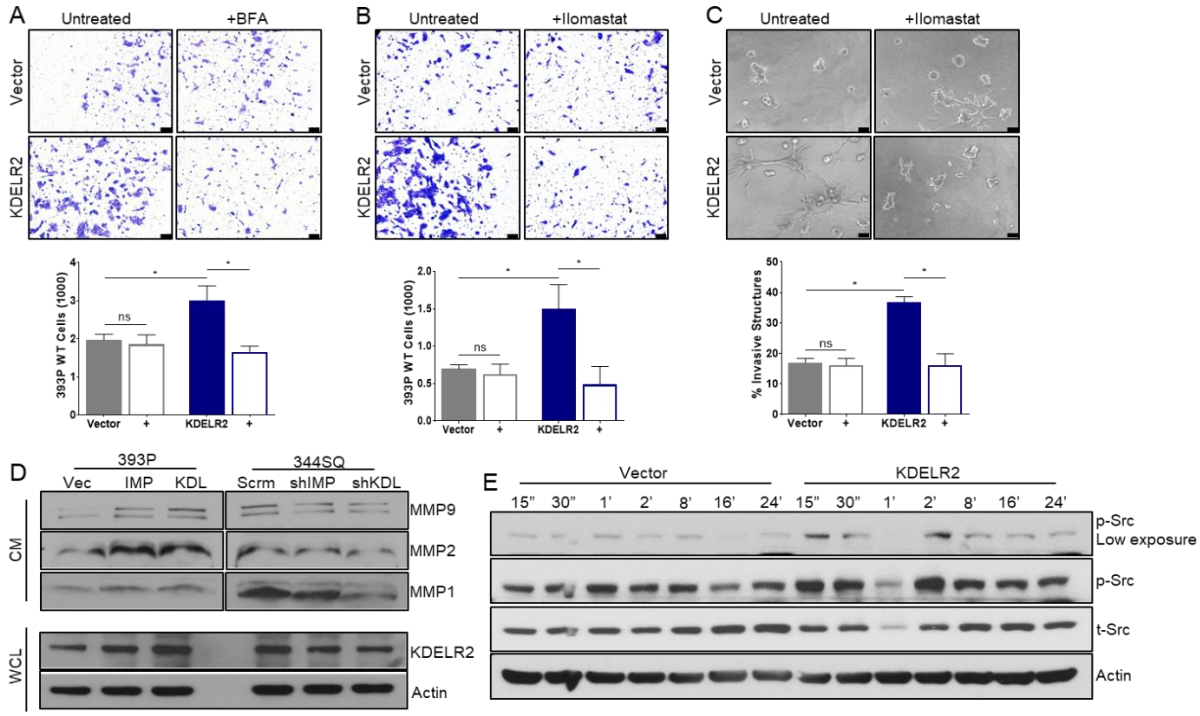

Figure 5-14. KDELR2 induces Golgi-mediated secretion of MMPs via the Src pathway to drive invasion. A-B. *CM from 393P KDELR2 overexpressing cells is sufficient to promote invasiveness of non-invasive 393P WT cells. This phenotype is rescued, when using CM from KDELR2 overexpressing cells after treatment with BFA (1uM 6 hours) (**A**), or Ilomastat (1uM) (**B**). **C.** Invasive structures formed upon KDELR2 overexpression, in a 1.5mg/ml collagen/matrigel, upon Ilomastat treatment (1uM) (day 5). (Scale bar:100uM). **D.** Western blot analysis of CM collected from KDELR2 overexpressing and knockdown cells shows KDELR2-regulated secretion of MMPs 1, 2, and 9. Whole cell lysate (WCL) collected from the same cells confirms KDELR2 overexpression and knockdown. **E.** Increased Src phosphorylation within two hours of KDELR2 induction. Data are represented as mean ± SEM. Significance by Student's T-test. P-value<0.05 - *; <0.002 - **. See also Figure 5-28.*

5.6 Discussions and conclusions

Metastasis causes 90% of cancer-related deaths, and targeted therapies may help reduce this mortality (Fidler, 2003). However, this requires a deeper understanding of the underlying processes regulating the metastatic cascade. EMT,

and enhanced Golgi kinetics during EMT are key features of this cascade, but the relation between these processes and their impact on tumorigenesis is understudied. Tan et al. ascertained that a Golgi protein, PI4KIIIβ, was genomically amplified in lung cancer and responsible for secretion of pro-survival factors such as semaphorin-3C (SEMA3C), lysyl hydroxylase-3 (PLOD3), tissue inhibitor of metalloproteinase-1 (TIMP1), etc. (Tan et al., 2020). Additionally, Reka et al. showed that the secretome from mesenchymal cells can be used to predict patient survival. Hence, it is crucial to gain a better understanding of the factors that mediate EMT-driven Golgi exocytosis.

I demonstrated that Impad1, our topmost hit from the invasion screen, resides in the *cis*- and *trans*-Golgi compartments. Moreover, I showed that Impad1 is a novel target of miR-200 and miR~96, and is de-repressed during EMT upon loss of these epithelial miRNAs. EMT is a key regulator of Golgi dynamics, which contribute to the altered cancer cell secretome. However, the epistatic pathway that connects EMT, Golgi function and secretion, and metastasis remains unclear. The LC-MS/MS data herein demonstrated that basal mesenchymal lung cancer cells have a distinct secretome signature. They secreted factors such as Cohesin SA-1 (Stag), Advillin (Avil), Fibroblast growth factor 21 (Fgf21), Matrilin-3 (Matn3), and Insulin-like growth factor 2 (Igf2b) that are known drivers and prognostic markers for various cancers. The high degree of overlap between the secretome components of mesenchymal cells and Impad1 overexpressing cells **(Figure 5-3A (A+D), Table 5-1)** specified that Impad1 might play a central role in the EMT-mediated exocytosis in cancer cells. Apart from collagen there were various secreted components with known roles in cancer that were not explored, such as Hpse, Sorl1, Krt5, and Lims1. Heparanase (Hpse)

cleaves heparin sulfate proteoglycan permitting invasion of cancer cells through the ECM. It is a widely studied protein in cancer metastasis and is involved in regulating all hallmarks of cancer (Jayatilleke & Hulett, 2020). Sortilin-related receptor 1 (Sorl1) is a Golgi-endosome protein that sorts proteins to their rightful destination. Sorl1 was shown to recycle Her2 back to the plasma membrane and its inhibition targets Her2 for lysosomal degradation and improved anti-Her2 therapy (Pietilä et al., 2019). Keratin-5 (Krt5) is a cytokeratin that is associated with ovarian cancer and chemotherapy resistance (Ricciardelli et al., 2017). The protein is also known to confer susceptibility in basal cell carcinoma and is involved in promoting breast and uterine cancers (Karantza, 2011). LIM Zinc Finger Domain Containing 1 (Lims1) is a LIM-domain protein regulating integrin signaling with kinases and in focal adhesion plaques. It is also known to play a role in integrin-mediated cell adhesion or spreading (Huang et al., 2019). Detailed studies on these components could further help unearth the role of EMT in exocytosis and metastasis.

Our group has previously shown that Collagen promotes immunesuppression by enhancing exhaustion of CD8+ T cells (D. H. Peng et al., 2020). Conversely, I determined that Impad1 suppresses the immune microenvironment by inhibiting effecter CD4+ and CD8+ T cell populations. Hence, Impad1 might be suppressing the TIME independent of the effects of Collagen. A cytokine array analysis might give some insight into the cytokines secreted by Impad1 in order to regulate the TIME.

I then established that Impad1 regulates the secretome by altering Golgi dynamics, more specifically the functional morphology and vesicular trafficking. Furthermore, Impad1 interacts with another trafficking protein, Syt11, to determine

vesicular trafficking, and exocytosis of invasive components during lung cancer. In addition to Syt11, I also elucidated that Impad1 interacts with another trafficking protein, Arf5, to maintain Golgi integrity and drive invasion **(Figure 5-25A, B)**. Surprisingly, this interaction was not necessary for promoting secretion and secretome-mediated invasion **(Figure 5-25C)**. Hence, my data indicate that aspects of lung cancer invasion might also be driven independent of changes in the Golgi-driven secretion. Moreover, it also specifies that Impad1 may have additional functions in the cells that affect Golgi dynamics but do not alter the secretome. The Golgi is also involved in post-translational modifications of proteins such as glycosylation, sulfation, ubiquitination, and lipidation (Pinho & Reis, 2015). Impad1 has been shown to regulate sulfated GAGs in the bone and cartilage ECM (Frederick et al., 2008; Sohaskey et al., 2008; Vissers et al., 2011). Additionally, I also determined that GAG deposition is dependent on Impad1 in lung cancer tumors **(Figure 5-19)**. Hence, investigating how and which PTMs are modulated by Impad1 at the Golgi will give a deeper insight into the glycobiology and glycocalyx of metastatic cancer cells undergoing EMT.

The Golgi can also be regulated independent of EMT by stimuli such as cellular stress, calcium signaling, cellular and environmental pH, etc. This was apparent from our work with Kdler2, where I ascertained that the protein shuttles between the Golgi and the ER. Although Kdelr2 has transient effects on the Src pathway; the function of the ER-Golgi pathway in regulating cellular secretion (Brandizzi & Barlowe, 2013; Viotti, 2016) helped establish that Kdelr2 drives invasion through enhanced Golgi-mediated secretion of proteases such as MMPs. Given that Kdelr2 was not regulated during and did not mediate EMT, I concluded that it is part of an EMT-independent

machinery that orchestrates exocytosis during metastasis. Further studies in this area might help in better understanding and targeting secretion to inhibit metastasis.

Based on our overall findings we propose a model where Impad1 is directly targeted by miRNAs, miR-200 and miR~96, and is repressed in epithelial cells. During EMT, loss of the epithelial miRNAs allows for de-repression of Impad1 in cancer progression. Impad1 then promotes Golgi organization and stacking, as well as vesicular trafficking to enhance exocytosis of MMPs, Collagens, GAGs, etc. Additionally, Impad1 also suppresses the TIME. These changes eventually make alter the TME to drive NSCLC invasion and metastasis. Thus, Impad1 acts as an epistatic link that connects EMT, Golgi function and secretome changes, and metastasis **(Figure 5-15)**. Lastly, we also propose an EMT-independent model of secretion, where Kdelr2 is auto-activated upon upregulation and enhances Golgi-mediated exocytosis of MMPs to drive lung cancer invasion and metastasis **(Figure 5-16)**.

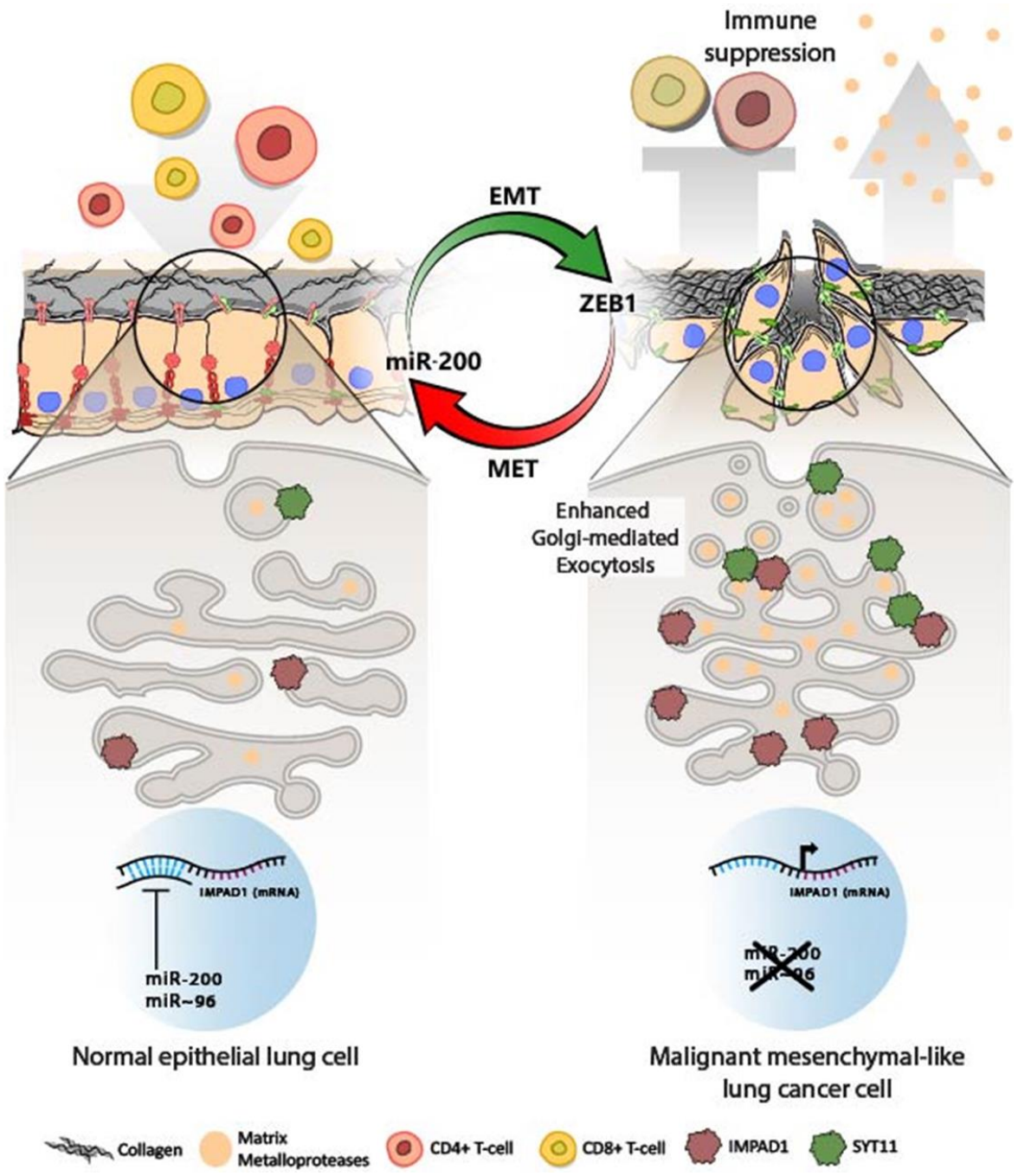

Figure 5-15. Working model for Impad1 modulation of Golgi morphology and vesicular trafficking to drive invasion and metastasis. *Loss of epithelial miRNAs, miR-200 and miR~96, de-repress Impad1, a Golgi-resident protein, during EMT. In mesenchymal cells, Impad1 promotes Golgi stacking and condensation, as well as vesicular trafficking by interaction with Syt11 to enhance exocytosis of extracellular components such as MMPs, collagen, GAGs, etc. This increased secretion alters the ECM and the immune landscape to drive lung cancer invasion and metastasis.*

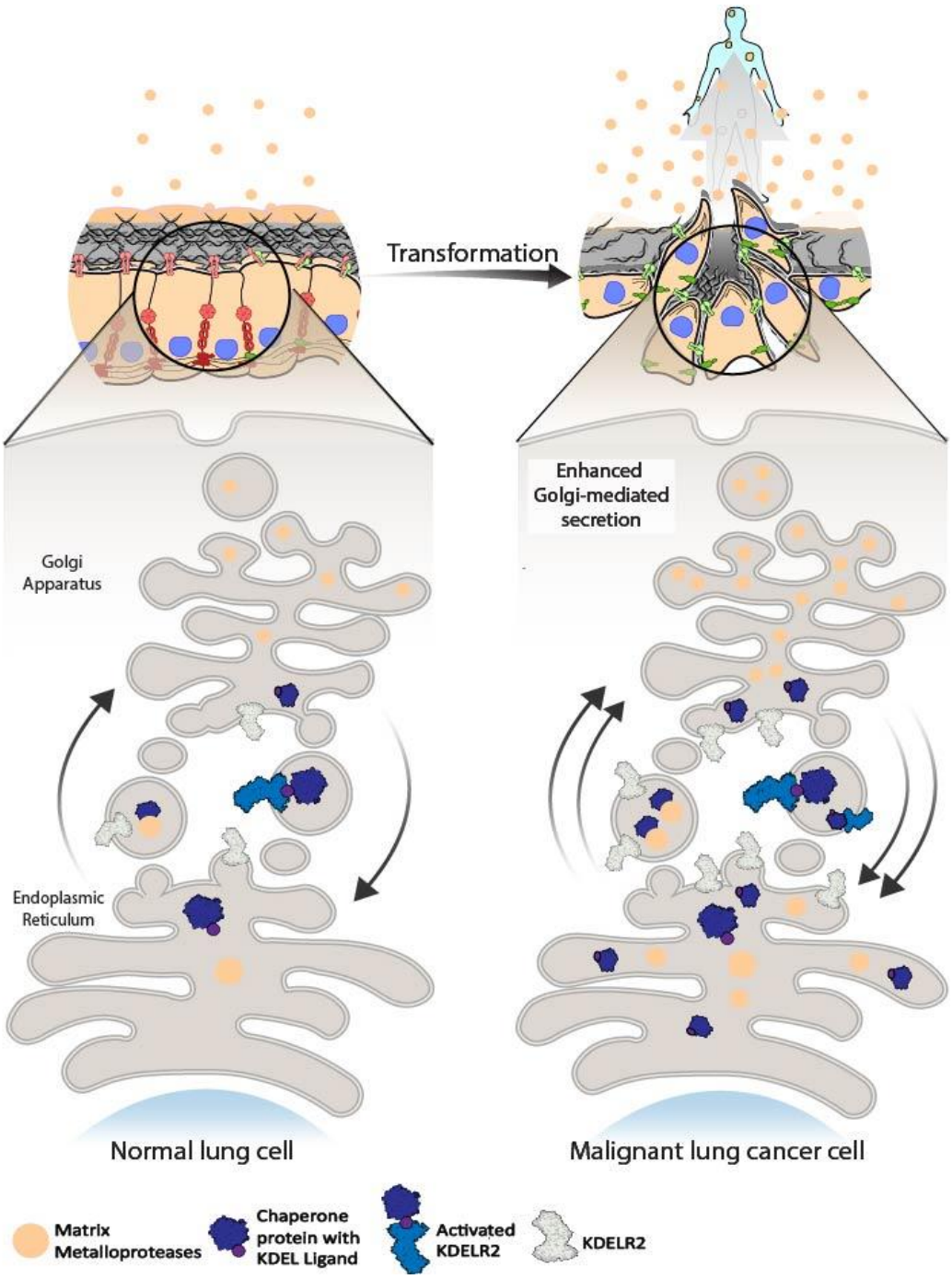

Figure 5-16. Working model for Kdelr2 as part of the ER-Golgi secretory cascade that regulates MMP secretion to drive NSCLC invasion and metastasis*. Cargo (secretory) proteins such as MMPs in the ER bind to chaperone proteins with a KDEL ligand. Once in the Golgi, MMPs dissociate from the chaperone protein and are secreted into the ECM, whereas chaperone proteins bind to Kdelr2 thus activating it during retrograde transport. Increased Kdelr2 expression in lung cancer cells lead to enhanced Golgi-mediated secretion of MMPs, thereby promoting NSCLC invasion and metastasis.*

5.7 Supplement data

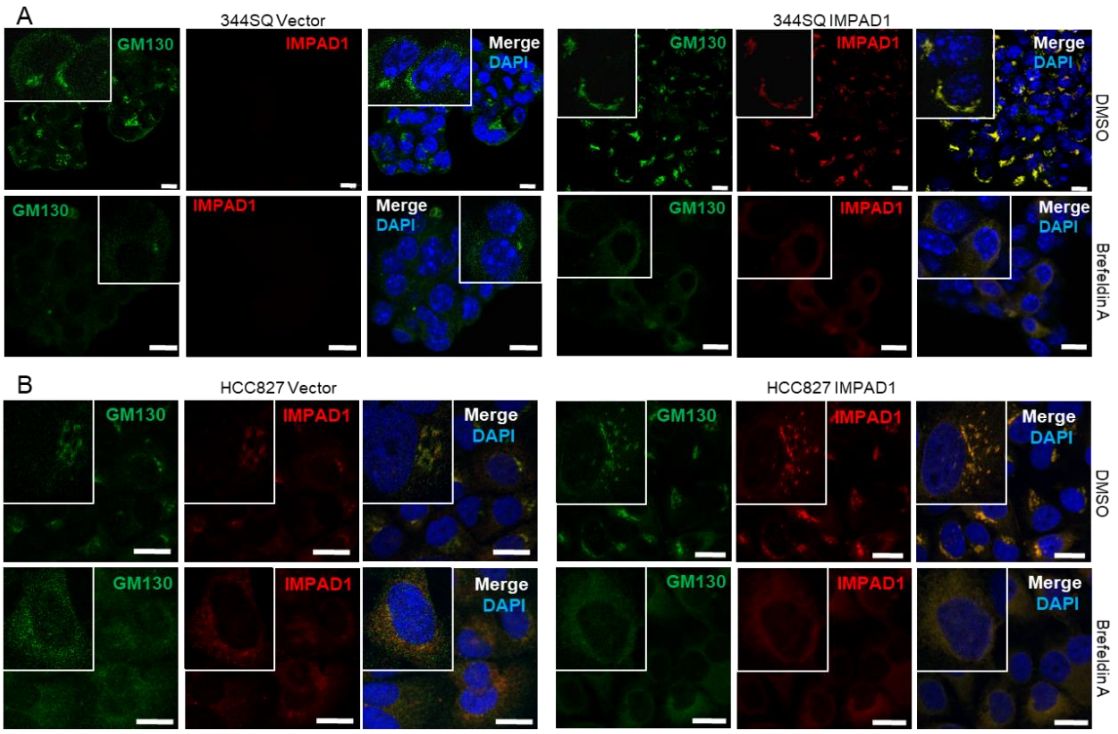

Figure 5-17. Impad1 localizes to the cis- and trans-Golgi compartments. A, B. *Co-IF staining for GM130 (green) and Impad1 (red) in 344SQ (A) or HCC827 (B) vector or IMPAD1 overexpressing cells. Nucleus counter-stained with DAPI.*

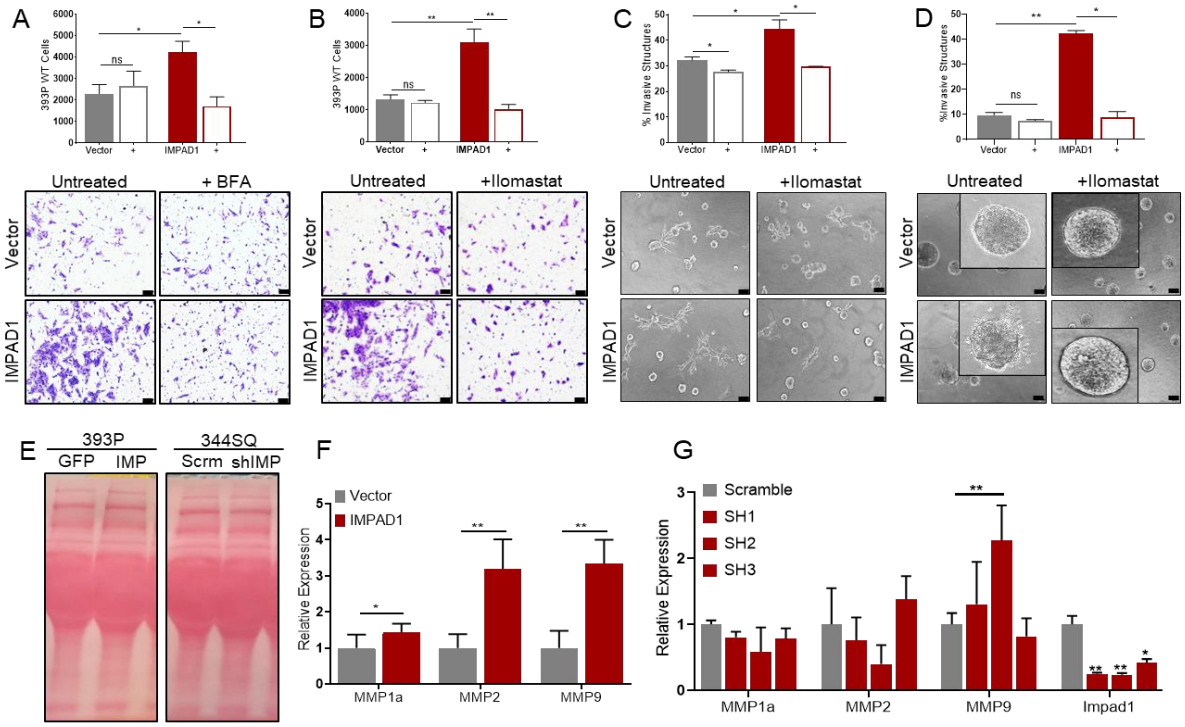

Figure 5-18. Impad1 regulates Golgi-mediated exocytosis of MMPs to drive lung cancer cell invasion. A, B. *Secretome-mediated invasion assay quantifying invasiveness of 393P WT cells replenished with CM from 344SQ vector or IMPAD1 overexpressing cells upon treatment with BFA, a Golgi secretion inhibitor (1uM 6 hours) (A), or Ilomastat, an MMP inhibitor (1uM) (B) (scale bar: 100 μM).* ***C, D.*** *Invasive structures formed upon IMPAD1 overexpression in 3D collagen/Matrigel matrix (1.5mg/ml) with Ilomastat treatment (1uM) in 344SQ (C) and HCC827 (D).* ***E.*** *Ponceau staining for blot for CM from IMPAD1 overexpressing and knockdown cells shows equal loading of the proteins.* ***F, G.*** *MMPs 1a, 2, and 9 mRNA expression in 393P IMPAD1 overexpressing (F) and 344SQ knockdown (G) cells. Data represented as mean ± SEM. Significance by Student's T-test. P-value<0.05 - *; <0.002 - ***

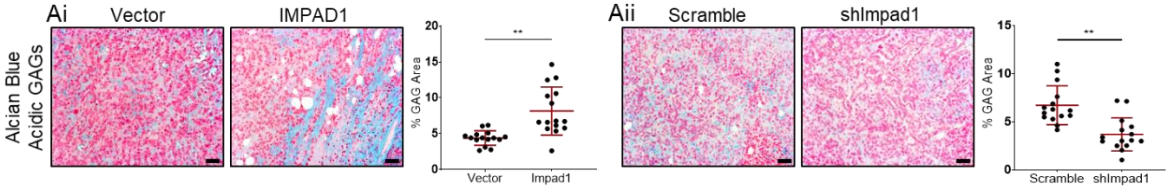

Figure 5-19. Impad1 regulates GAG deposition in the ECM. A. *Representative images for Alcian blue staining for GAGs (left). Quantification for %GAG area in 344SQ vector and Impad1*

overexpressing (Ai), as well as Scramble control and shImpad1 knockdown (Aii) syngeneic tumors. N=15 (scale bar: 50uM).

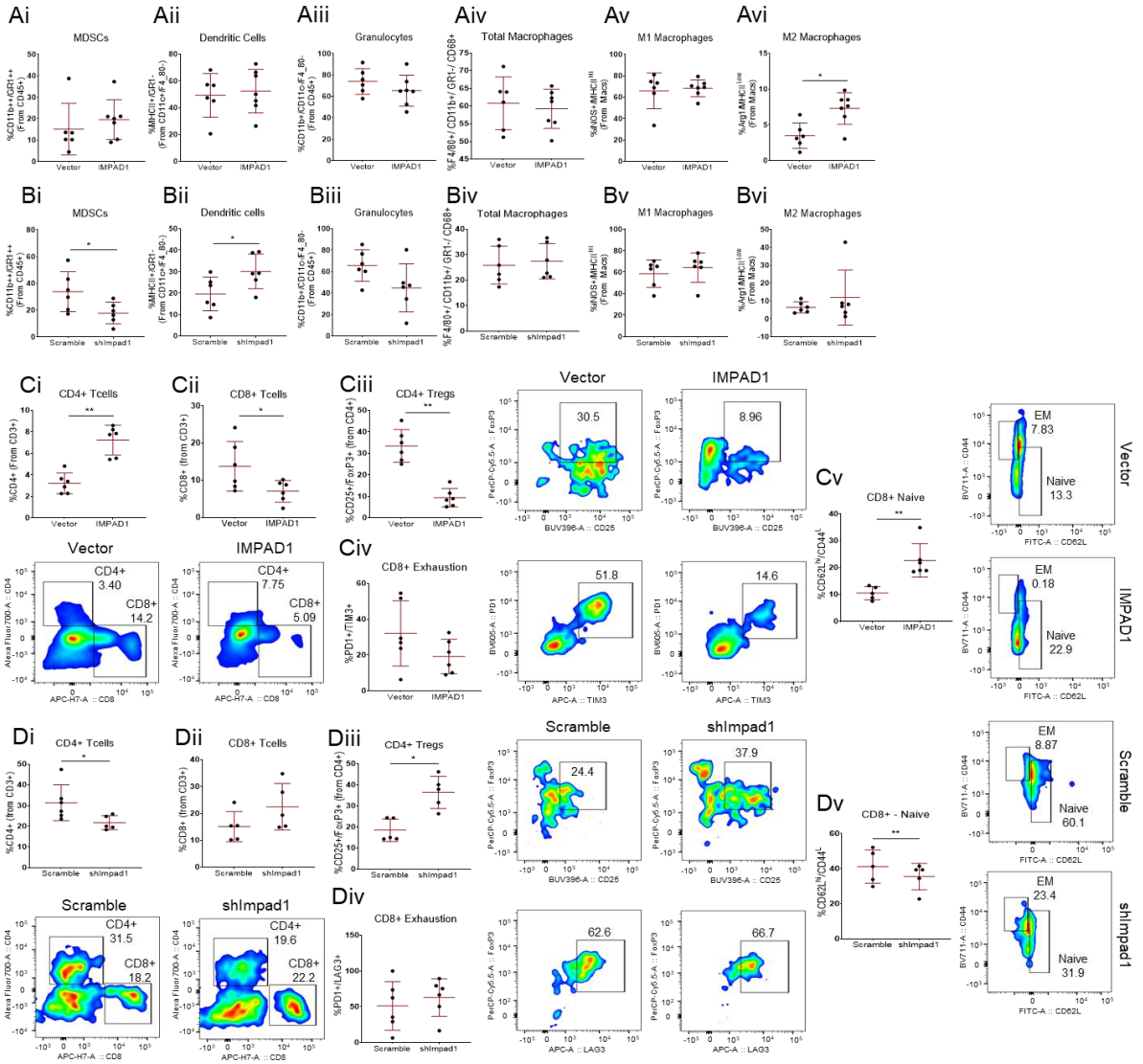

Figure 5-20. Impad1 regulates the tumor immune microenvironment. A, B. *Dot plots quantifying multi-parametric flow cytometry analysis for myeloid-derived cells in 344SQ vector and IMPAD1 overexpressing (A), as well as Scramble control and shImpad1 knockdown (B) syngeneic tumors N=6.* ***C, D.*** *Dot plots and representative FACS plots for lymphoid-derived CD4+, CD8+ T cells in 344SQ vector and IMPAD1 overexpressing (C), as well as Scramble control and shImpad1 knockdown (D) syngeneic tumors. N=6. Data are represented as mean ± SD. Significance by Student's T-test. P-value<0.05 - *; <0.002 - ***

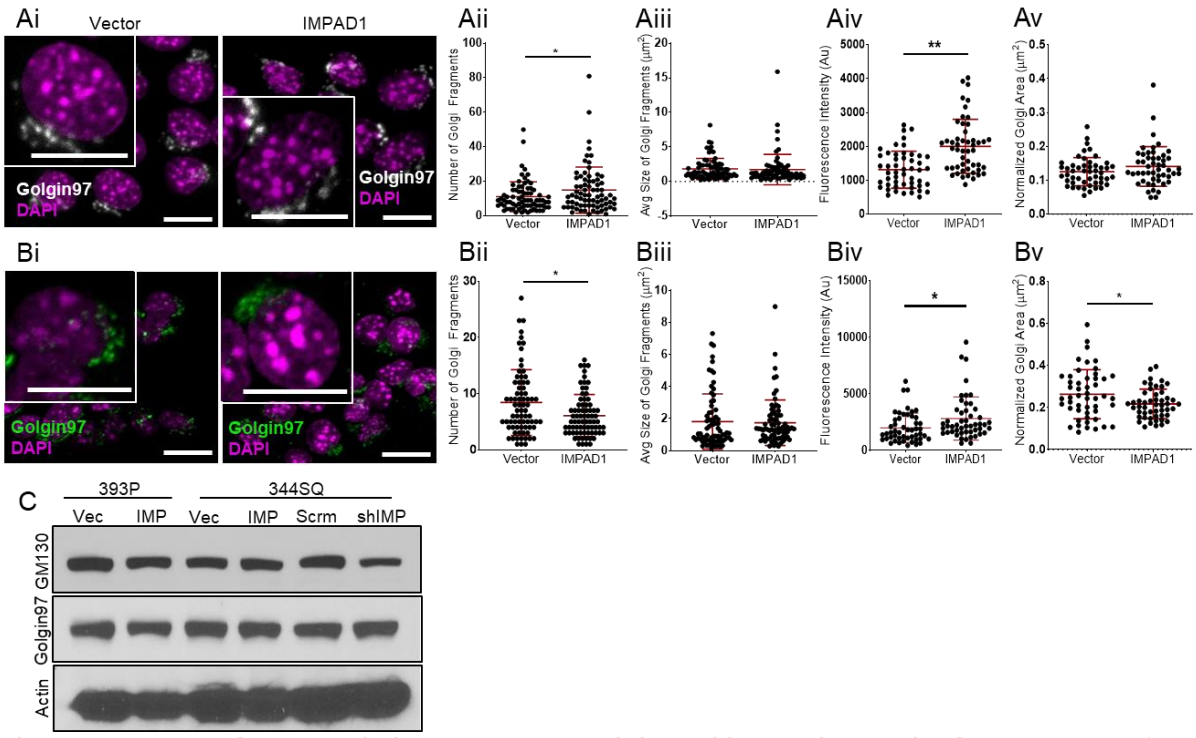

Figure 5-21. Impad1 upregulation promotes Golgi stacking and organization. A, B. *Confocal images of Golgi (Golgin97, white (A) green (B)) and nuclei (DAPI, magenta) in 393P (A) and 344SQ (B) vector or Impad1 overexpressing cells. Scatter plots show number of Golgi fragments/cell N=75 (Aii, Bii), average size of Golgi fragments/cell N=75 (Aiii, Biii), fluorescence intensity of Golgi N=50 (Aiv, Biv), and normalized Golgi area N=50 (Av, Bv).* ***C.*** *Western blot analysis for GM130 and Golgin97 expression upon Impad1 overexpression (393P and 344SQ) and knockdown (344SQ). Actin was used as loading control. All scale bars: 10uM. Data are represented as mean ± SD. Significance by Student's T-test. P-value<0.05 - *; <0.002 - ***

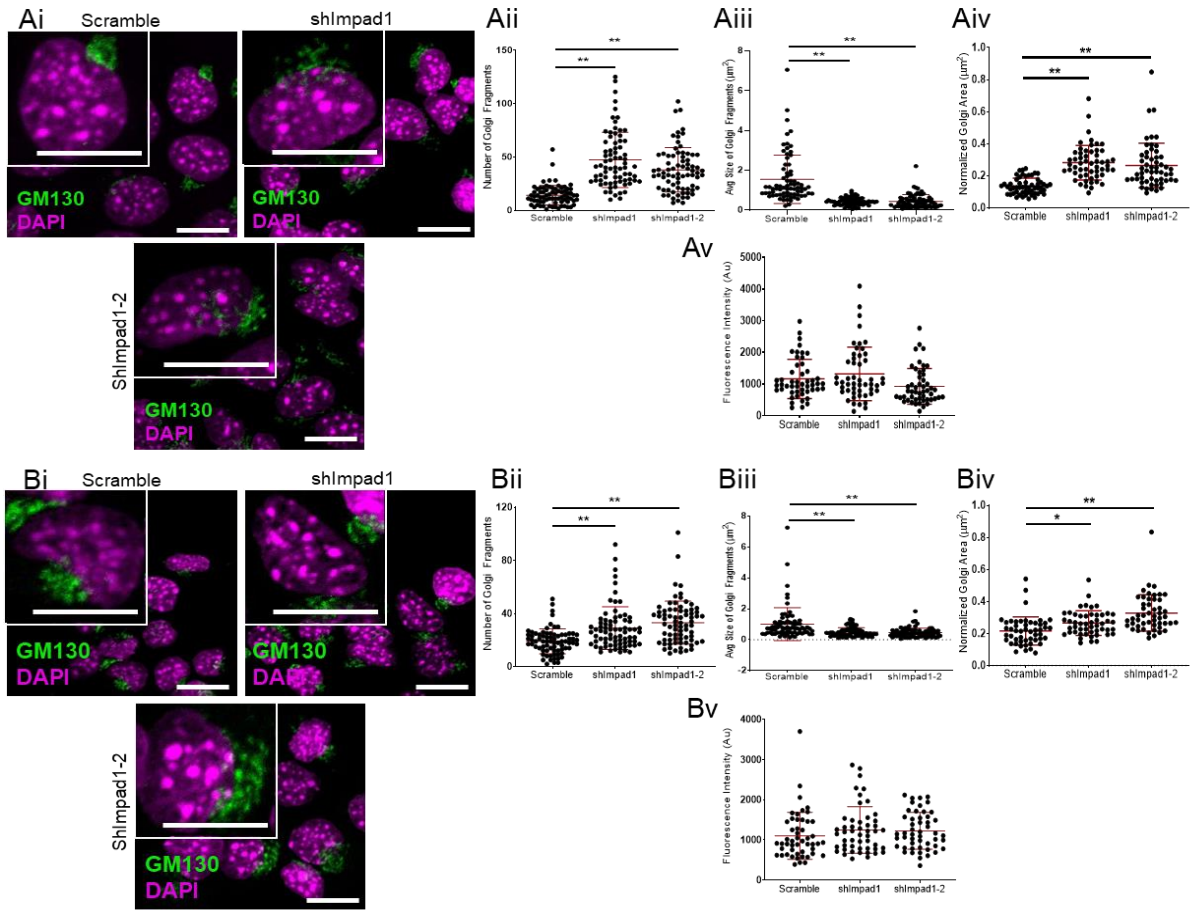

Figure 5-22. Loss of Impad1 disrupts Golgi morphology. A, B. *Confocal images of Golgi (GM130, green) and nuclei (DAPI, magenta) in 344P (A) and 344LN (B) scramble or Impad1 knockdown cells. Scatter plots show number of Golgi fragments/cell N=75 (Aii, Bii), average size of Golgi fragments/cell N=75 (Aiii, Biii), fluorescence intensity of Golgi N=50 (Aiv, Biv), and normalized Golgi area N=50 (Av, Bv). All scale bars: 10uM. Data are represented as mean ± SD. Significance by Student's T-test. P-value<0.05 - *; <0.002 - **.*

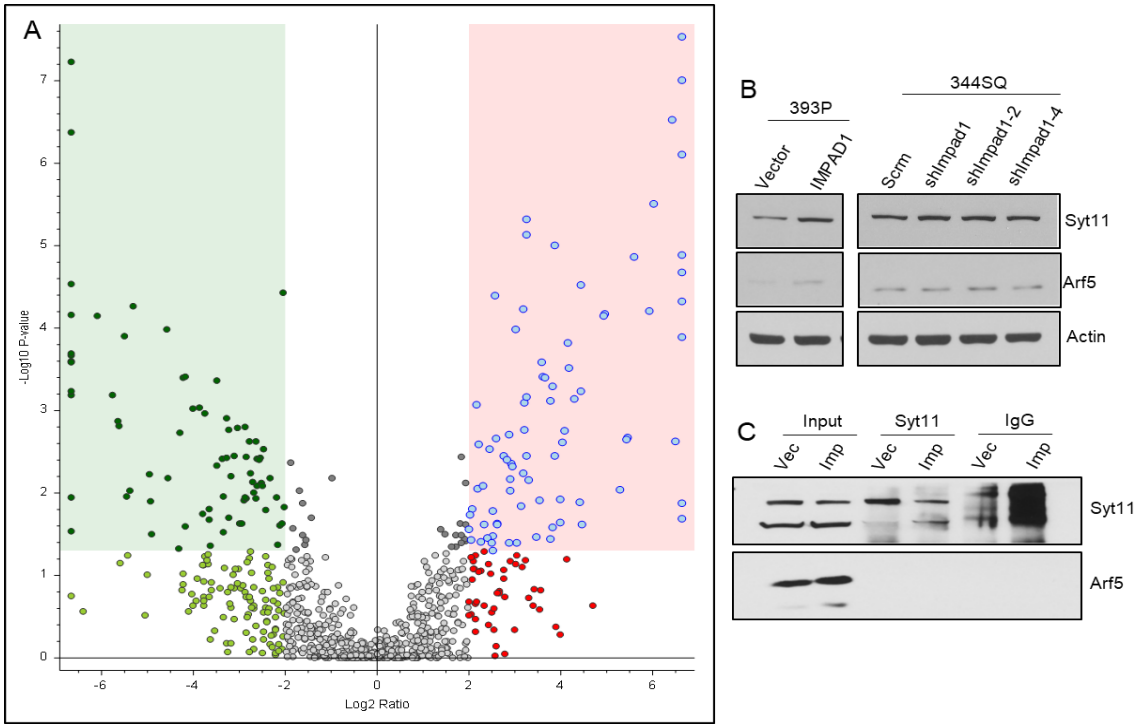

Figure 5-23. Impad1 interactome. A. *Volcano plot showing Impad1 interactome obtained from IP-MS analysis.* ***B.*** *Syt11 and Arf5 protein levels upon Impad1 overexpression (393P) and knockdown (344SQ).* ***C.*** *Co-immunoprecipitation of Syt11 and Arf5 in 393P vector and Impad1 overexpressing cells. see also Table 5-2.*

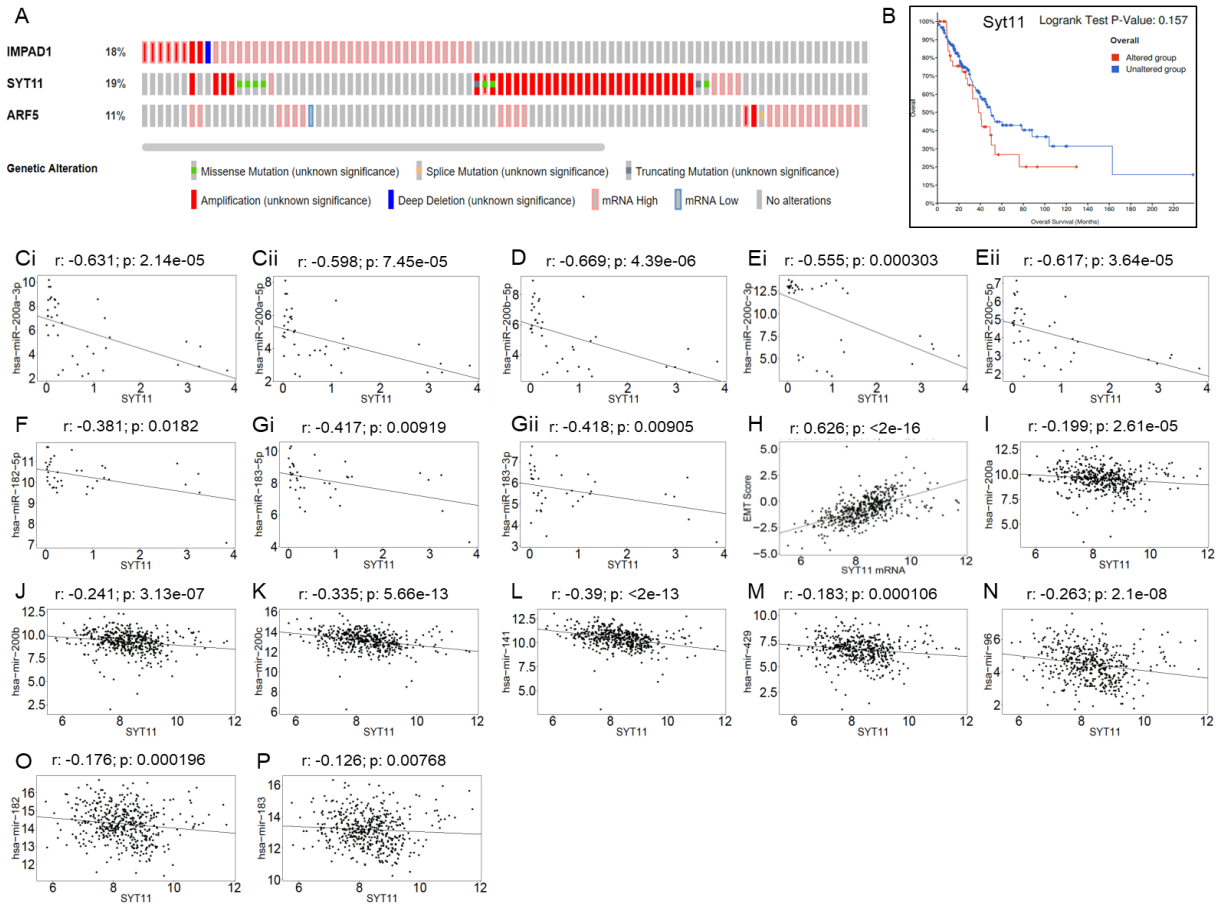

Figure 5-24. Syt11 is upregulated during EMT in lung adenocarcinoma. A. *Syt11 and Arf5 mutation frequency and amplification compared to Impad1 in lung adenocarcinoma (LuAd) patients according to TCGA (cBioPortal – Firehose legacy data).* ***B.*** *No significant change in survival upon alterations in Syt11 mRNA levels.* ***C-P.*** *Correlation of Syt11 with respective miRNA family/cluster members in human NSCLC cell lines (UTSW dataset, C-Gii) and tumors (TCGA-LuAd, H-P).*

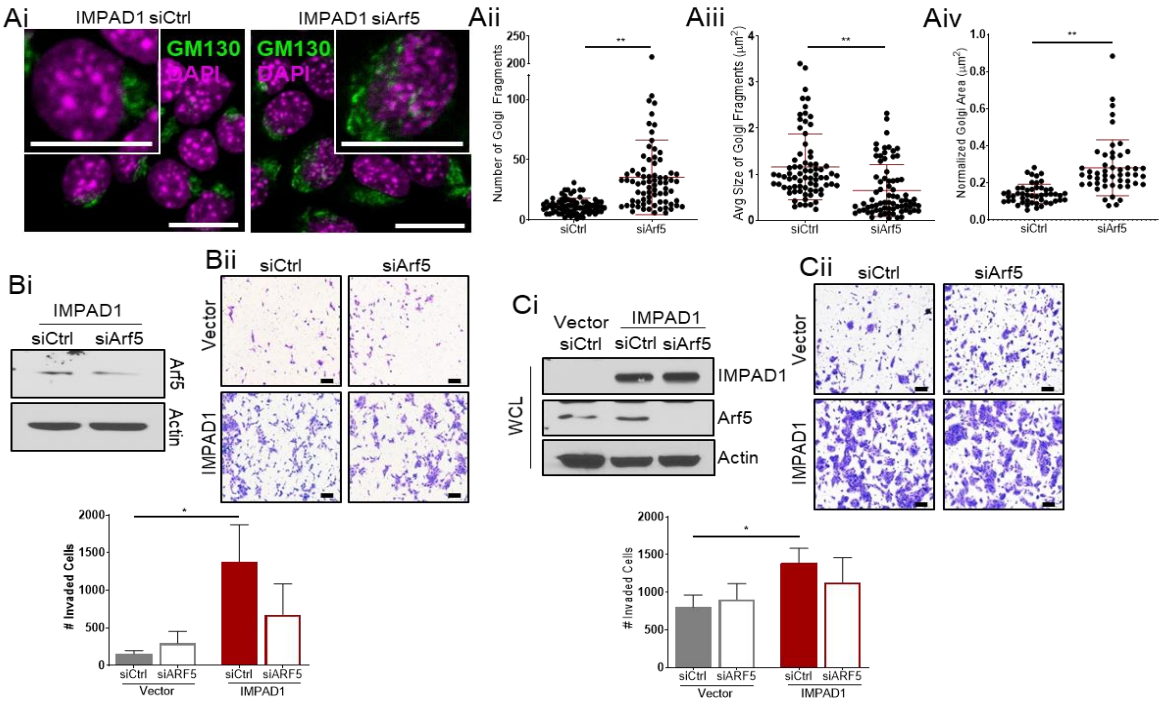

Figure 5-25. Impad1 interaction with Arf5 is necessary for maintaining Golgi morphology but not for regulating secretome-mediated invasion. A. *Confocal images of Golgi (GM130, green) and nucleus (DAPI, magenta) in 393P Impad1 overexpressing cells with siControl or siArf5 (i). Scatter plots show number of Golgi fragments/cell N=75 (ii), average size of Golgi fragments/cell N=75 (iii), and normalized Golgi area N=50 (iv). (scale bar: 10uM)* ***B.*** *Western blot analysis for siRNA-mediated knockdown of Arf5 in 393P Impad1 overexpressing cells (i). Representative images of invasion assay upon siArf5 in 393P vector or Impad1 overexpressing cells (ii). (scale bar: 100uM)* ***C.*** *Confirmation of siRNA-mediated knockdown of Arf5 in WCL of 393P Impad1 overexpressing cells (i). Secretome-mediated invasion assay quantifying invasiveness of 393P WT cells replenished with CM from 393P vector or Impad1 overexpressing cells with or without siArf5 (ii). (scale bar: 100uM)*

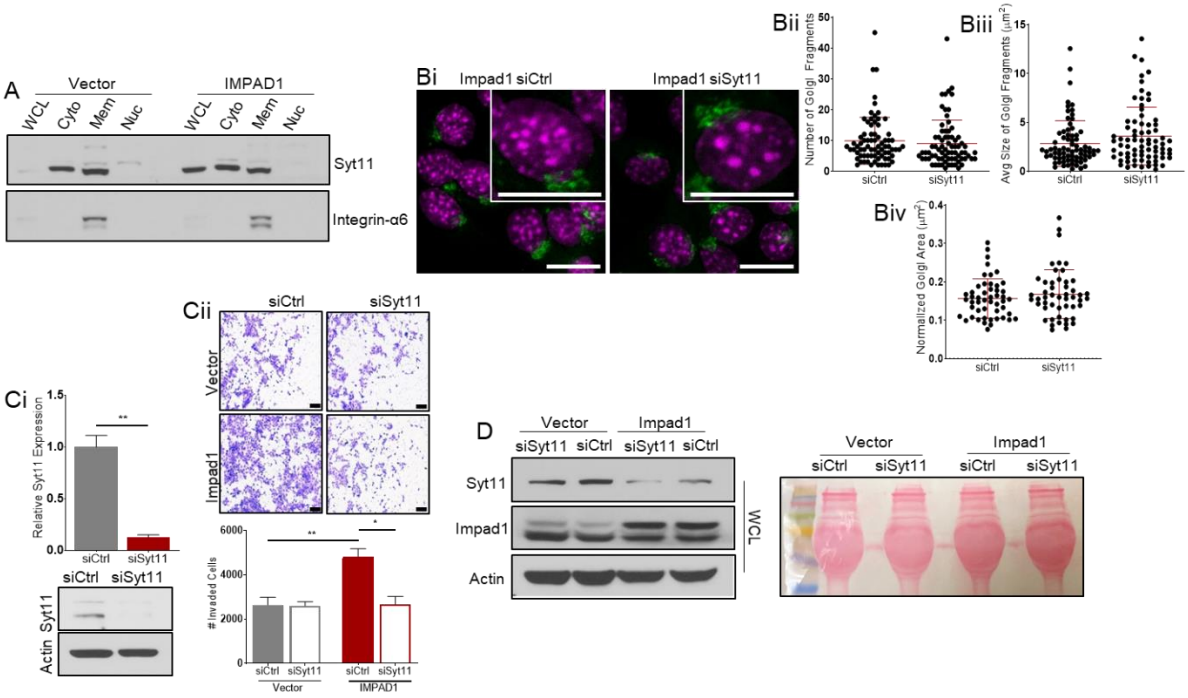

Figure 5-26. Impad1 interaction with Syt11 is necessary to drive exocytosis and invasion in lung cancer. A. *Fractionation assay to determine Syt11 localization in 393P Impad1 overexpressing cells. Integrin α6 was used as the loading control for the membrane fraction. WCL – whole cell lysate, Cyto – cytoplasmic fraction, Mem – membrane fraction, Nuc – nuclear and cytoskeletal fraction.* ***B.*** *Confocal images of Golgi (GM130, green) and nucleus (DAPI, magenta) in 393P Impad1 overexpressing cells with siControl or siSyt11 (i). Scatter plots show number of Golgi fragments/cell N=75 (ii), average size of Golgi fragments/cell N=75 (iii), and normalized Golgi area N=50 (iv). (scale bar: 10uM)* ***C.*** *mRNA and protein confirmation of siRNA-mediated knockdown of Syt11 in 344SQ Impad1 overexpressing cells (i). Representative images of Boyden chamber assay quantifying cell invasion upon siSyt11 in 344SQ vector or Impad1 overexpressing cells (ii). (scale bar: 100uM)* ***D.*** *Confirmation of siRNA-mediated knockdown of Syt11 in WCL of 393P vector or Impad1 overexpressing cells (left). Ponceau staining was used as loading control for blot run for conditioned media (right). Data are represented as mean ± SD. Significance by Student's T-test. P-value<0.05 - *; <0.002 - ***

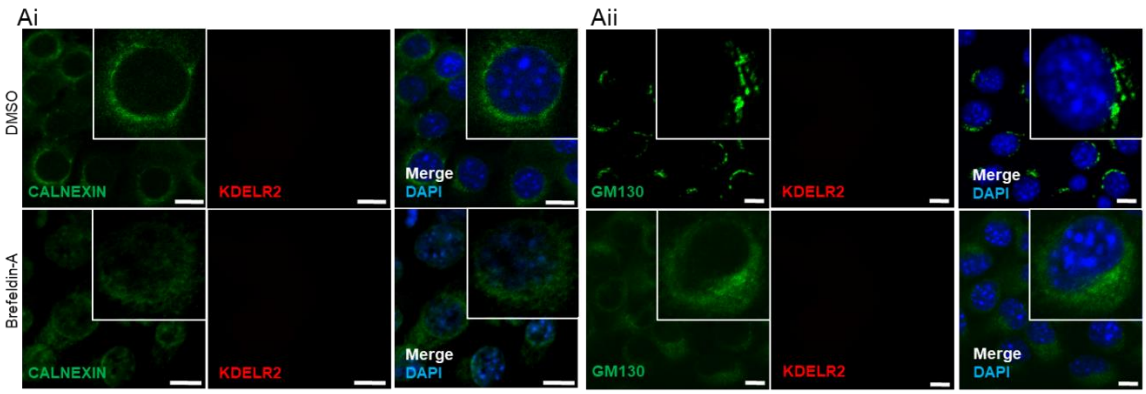

Figure 5-27. Kdelr2 localizes to the ER-Golgi pathway. A i-ii *Co-IF with FLAG (red) and ER marker, Calnexin (green) (i) or FLAG (red) and Golgi marker, GM130 (green) (ii) in 393P control cells. Nucleus was stained with DAPI. Cells were treated with DMSO (upper) or Brefeldin-A (1uM 6 hours) (lower).*

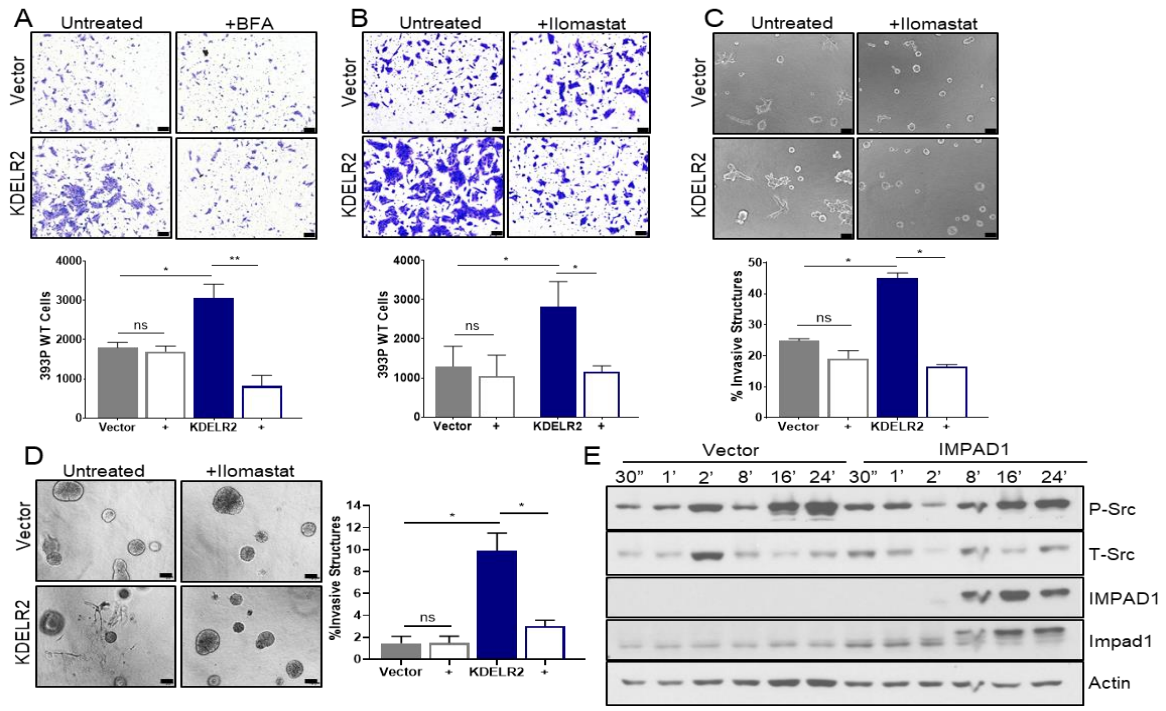

Figure 5-28. KDELR2 induces Golgi-mediated secretion of MMPs via the Src pathway to drive invasion. A-B. *CM from 344SQ KDELR2 overexpressing cells is sufficient to promote invasiveness of 393P WT cells. This phenotype is reversed upon treatment with BFA (1uM 6 hours) (**A**), and Ilomastat (1uM) (**B**). **C, D** Invasive structures formed upon Kdelr2 overexpression in collagen/matrigel matrix (1.5mg/ml) is inhibited upon MMP inhibition with Ilomastat (1uM) (day 5) in murine (**C**) and human (**D**) cells. (Scale bars: 100uM). **E.** Changes in Src signaling not attributed to increased IMPAD1 expression as shown by western blot.*

Table 1(A).

Gene	Ratio	P-value	Gene	Ratio	P-value	Gene	Ratio	P-value
Eif2s3y	6.64	6.7E-17	Hid1	6.64	6.7E-17	Ceacam1	6.64	6.7E-17
Wapl	6.64	6.7E-17	Tbc1d10a	6.64	6.7E-17	Adnp	6.64	6.7E-17
Rsl1d1	6.64	6.7E-17	Gfer	6.64	6.7E-17	B4galt4	6.64	6.7E-17
Pdlim	6.64	6.7E-17	Scaf11	6.64	6.7E-17	Ints7	6.64	6.7E-17
Avil	6.64	6.7E-17	Gbf1	6.64	6.7E-17	Polr3a	6.64	6.7E-17
Stag	6.64	6.7E-17	Tfip11	6.64	6.7E-17	Tns4	6.64	6.7E-17
Slc4a1ap	6.64	6.7E-17	Upp1	6.64	6.7E-17	Rbm10	6.64	6.7E-17
Pklr	6.64	6.7E-17	Hmg20a	6.64	6.7E-17	Vps50	6.64	6.7E-17
Bag3	6.64	6.7E-17	Ogfod1	6.64	6.7E-17	Arid2	6.64	6.7E-17
Serpinb2	6.64	6.7E-17	Ccdc91	6.64	6.7E-17	Ddc	6.64	6.7E-17
Esf1	6.64	6.7E-17	Wipf2	6.64	6.7E-17	Trim24	6.64	6.7E-17
Mdc1	6.64	6.7E-17	Rbm26	6.64	6.7E-17	Homer1	6.64	6.7E-17
Wipi1	6.64	6.7E-17	Me2	6.64	6.7E-17	Ranbp9	6.64	6.7E-17
Prmt3	6.64	6.7E-17	Ubqln4	6.64	6.7E-17	Suz12	6.64	6.7E-17
Anapc2	6.64	6.7E-17	Cog2	6.64	6.7E-17	Clasrp	6.64	6.7E-17
Fgf21	6.64	6.7E-17	Kank2	6.64	6.7E-17	Zc3h18	5.65	0.00144
Men	6.64	6.7E-17	Smg1	6.64	6.7E-17	Gm17190	5.34	4.3E-08
Emc8	6.64	6.7E-17	Dph2	6.64	6.7E-17	Cdkn2aip	5.28	6.7E-17
Sirt2	6.64	6.7E-17	Sema4g	6.64	6.7E-17	Rragc	5.14	6.7E-17
Nudcd3	6.64	6.7E-17	Aqr	6.64	6.7E-17	Thg1l	3.91	0.03733
Znf830	6.64	6.7E-17	Hectd3	6.64	6.7E-17	Dph7	3.65	0.06077
Anapc5	6.64	6.7E-17	Tssc4	6.64	6.7E-17	Ifrd1	3.5	0.00854
Matn3	6.64	6.7E-17	Smtn	6.64	6.7E-17	Hnrnpa3	3.39	4.0E-06
Cpsf2	6.64	6.7E-17	Ctc1	6.64	6.7E-17	Plscr1	3.38	6.5E-09
Pdgfb	6.64	6.7E-17	Plekha6	6.64	6.7E-17	Lman1l	3.1	0.16820
Tab1	6.64	6.7E-17	Hpx	6.64	6.7E-17	Nup37	2.28	0.04743
Med24	6.64	6.7E-17	Ccdc102a	6.64	6.7E-17	Tra2a	2.27	0.17473
Ttc5	6.64	6.7E-17	Gnaq	6.64	6.7E-17	Nup54	2.16	0.19020
Igf2bp1	6.64	6.7E-17	Itch	6.64	6.7E-17	Slc9a3r2	2.14	0.15346
Cavin2	6.64	6.7E-17	Csnk2a2	6.64	6.7E-17	Ccn2	2.05	0.00027
Uprt	6.64	6.7E-17	Khdc4	6.64	6.7E-17	Gcnt3	1.74	0.00391
Ubr7	6.64	6.7E-17	Cym	6.64	6.7E-17	Ccn1	1.27	0.08421
Ints12	6.64	6.7E-17	Prkab1	6.64	6.7E-17			

Table 1(B).

Gene	Ratio	P-value	Gene	Ratio	P-value	Gene	Ratio	P-value
Fbxo22	6.41	6.7E-17	Abr	3.65	1.5E-05	Optn	2.7	0.06805
Kpna1	5.3	6.5E-07	Ripk1	3.29	0.01613	Lsm7	2.63	2.8E-06
Dcaf8	4.59	8.9E-14	Prss35	2.95	0.18761	Atp6v1c1	1.63	0.17947
Rp2	4.11	9.8E-05	Cit	2.75	0.09061			

Table 1(C).

Gene	Ratio	P-value	Gene	Ratio	P-value	Gene	Ratio	P-value
Psmd4	-6.64	1.2E-16	Hmmr	-6.64	1.2E-16	Dars2	-6.64	1.2E-16
Akt3	-6.64	1.2E-16	Eif1ad	-6.64	1.2E-16	Wdr55	-6.64	1.2E-16
Rsf1	-6.64	1.2E-16	Nol4l	-6.64	1.2E-16	Rbfox2	-4.7	0.00051
Asf1b	-6.64	1.2E-16	Nemf	-6.64	1.2E-16	Ints2	-3.62	0.01869
Casp7	-6.64	1.2E-16	Ca13	-6.64	1.2E-16	Exoc2	-3.56	6.1E-06
Cdc40	-6.64	1.2E-16	Trmt13	-6.64	1.2E-16	Trmt5	-2.94	0.08145
Mpp6	-6.64	1.2E-16	Srfbp1	-6.64	1.2E-16	Tor2a	-2.34	0.00015
Cdk12	-6.64	1.2E-16	Uhrf1	-6.64	1.2E-16	Epn1	-2.28	0.01774
Rab11fip1	-6.64	1.2E-16	Sipa1	-6.64	1.2E-16	Mvb12a	-2.06	0.01596
Aktip	-6.64	1.2E-16	Rbm22	-6.64	1.2E-16	Riok3	-1.89	0.08286
Appl2	-6.64	1.2E-16	As3mt	-6.64	1.2E-16	Rras2	-1.88	0.00130
Rab3gap1	-6.64	1.2E-16	Ppip5k2	-6.64	1.2E-16	Btf3l4	-1.74	0.01361
Kif4	-6.64	1.2E-16	Pes1	-6.64	1.2E-16	Rrp1	-1.68	0.01889
Custos	-6.64	1.2E-16	Gm50478	-6.64	1.2E-16	Parvb	-1.5	0.10960
Tex30	-6.64	1.2E-16	Dmxl1	-6.64	1.2E-16	Adarb1	-1.43	0.17229
Itsn2	-6.64	1.2E-16	Pou2f1	-6.64	1.2E-16	Foxa2	-1.42	0.20886
Plekha2	-6.64	1.2E-16	Araf	-6.64	1.2E-16	Septin10	-1	0.20664
Dvl2	-6.64	1.2E-16	Ogn	-6.64	1.2E-16			

Table 1(D).

Gene	Ratio	P-value	Gene	Ratio	P-value	Gene	Ratio	P-value
Ybx3	6.64	6.7E-17	Tubgcp4	6.64	6.7E-17	Parg	6.64	6.7E-17
Prrc2b	6.64	6.7E-17	Hpse	6.64	6.7E-17	Ubl4a	6.64	6.7E-17
Fnbp4	6.64	6.7E-17	Gatad2b	6.64	6.7E-17	Stn1	6.64	6.7E-17
Sarg	6.64	6.7E-17	Limd1	6.64	6.7E-17	Col12a1	5.9	0.00781
Snrnp27	6.64	6.7E-17	Chac2	6.64	6.7E-17	Taok3	3.08	0.13803
Otud7b	6.64	6.7E-17	Luzp1	6.64	6.7E-17	Aamdc	2.69	0.05155
Acadsb	6.64	6.7E-17	Rab3gap2	6.64	6.7E-17	Lims1	2.42	0.04753
Mvk	6.64	6.7E-17	Rpl28	6.64	6.7E-17	KRT35	2.39	1.5E-05
Ythdf3	6.64	6.7E-17	Csnk2b	6.64	6.7E-17	Sorl1	2.11	0.18676
Dusp3	6.64	6.7E-17	Camsap1	6.64	6.7E-17	Eloa	1.52	0.63139
Washc4	6.64	6.7E-17	Dgcr2	6.64	6.7E-17	Parg	6.64	6.7E-17

Table 5-1. Factors exocytosed into secretome as identified by LC-MS/MS. A (First)*. Factors that were high in the CM of epithelial 393P Impad1 overexpressing cells and mesenchymal 344SQ scramble control cells.* ***B (Second).*** *Factors that were high in CM of 393P Impad1 overexpressing cells and low in 344SQ shImpad1 cells.* ***C (Third).*** *Factors that were high in CM of 344SQ scramble control cells and low in 344SQ shImpad1 cells.* ***D (Fourth).*** *Factors that were high in CM of 393P Impad1 overexpressing cells, high in 344SQ scramble control cells, and low in 344SQ shImpad1 cells.*

Gene	Ratio	P-Value	LuAd	Gene	Ratio	P-Value	LuAd
Igkv2-137	100	4.4E-05	0	Gar1	10	0.08004	
Saa1	100	5.6E-05	2.2	Hnrnpl	10	0.01681	10
Ighv10-1	100	0.00022	0	Rpl10	10	0.05405	
Igkv8-16	100	0.00150	0	Ighm	10	0.00102	2.1
Syt11	100	0.00192	17	Cfh	10	0.00118	13
Pdzd3	100	0.00350	5	Fn1	9	0.01791	5
Cfp	100	0.00531	7	Rbm39	9	0.03219	11
Trmt112	100	0.12468	7	Ssb	9	0.00367	9
Rad54l2	100	0.16177	6	Gc	9	0.07584	
Sdr9c7	91	0.04021	3	Cfb	9	0.13241	
Ighv10-3	86	0.00011	0	Mbl1	8	0.24348	
Caprin1	65	0.00078	7	C4b	8	0.00483	2.3
C1qa	61	0.00366	5	Trim30c	8	0.06434	
Ighv1-11	49	0.00150	0	IghV-21	8	0.06031	
Ighm	44	0.03786	2.1	Hnrnpa2b1	8	0.07966	
Ighk-VII	43	0.03883	1	Ighv1-82	7	0.09755	
Fcgr1	40	0.09755		Ddx17	7	0.24452	
Osbpl3	31	0.00367	12	Gm9242	7	0.03518	
Apoa1	31	0.00367	2.9	Ddx5	7	0.05552	
Pabpc4	22	0.17571		Ddx18	7	0.05405	
Cd5l	22	0.00253	12	Prpf6	6	0.17571	
Arf5	22	0.01581	10	Rps5	6	0.17571	
Nifk	21	0.12399		Igkc	6	0.03825	1
Hpx	20	0.01759	4	Plg	6	0.00312	
Gm4788	18	0.01001		Iglv2	6	0.27940	
Ighv7-2	18	0.00604	0	Ywhaq	6	0.21719	
Fus	17	0.03269	8	Myo1c	6	0.14390	
Znf488	16	0.04051	6	Rpl23a	6	0.24348	
Mlec	16	0.11576		Mybbp1a	5	0.04670	5
Ighg1	16	0.17297		Snrpf	5	0.22339	
C3	15	0.00141	7	Taf15	5	0.17731	
Hnrnpa0	15	0.05405		Mtdh	5	0.09018	
Ewsr1	14	0.01474	6	Hp	5	0.24260	
Ybx3	14	0.18660		Rps20	5	0.04259	9
C8a	14	0.01791	3	Ighv7-1	5	0.09628	
Rsl1d1	14	0.22813		C8b	5	0.01854	7
Igh-3	13	0.01270	0	Prps1l3	4	0.13962	
IghV	12	0.01266		Rps13	4	0.23252	
Igg-3C	12	0.00914		Rps7	4	0.15110	
IghV-345	12	0.11817		Rps3a	4	0.19350	
Tra2b	11	0.22095					

Table 5-2. Impad1 interactome identified by using IP-MS. *Table showing hits from IP-MS performed on 393P Impad1-Flag overexpressing cells. Hits filtered based on significant upregulation upon Impad1 overexpression (p-value<0.05), amplification in lung adenocarcinoma (>1.5-fold), and annotated to be associated with Golgi.*

Chapter 6: Future perspectives

Metastasis of the cancer cells is now widely accepted as the primary cause of cancer-related deaths, especially in highly aggressive types such as NSCLC. Treatments for lung cancer have evolved over the years, translating to enhanced and improved patient survival (Lim et al., 2020; Yuan et al., 2019). However, predictive models indicate that lung cancer will remain the leading cause of cancer-deaths for the next 20 years (Rahib et al., 2021). Thus, a better understanding of the underlying mechanisms of metastasis can introduce novel modes of treatment that help reduce this mortality. Given the complexity of the metastatic cascade, unbiased systematic approaches might be ideal to study the disease (Eccles et al., 2017). In chapter 3, I adopted one such approach by performing a high-throughput *in vitro* screen to identify novel drivers of NSCLC invasion and metastasis. The screen discovered >30 potent drivers of lung cancer invasion that were further validated, thus signifying the stringency and accuracy of the screen. Of these, I showed that Impad1 and Kdelr2 were sufficient and necessary for driving not only invasion but also metastasis. Investigating the underlying mechanisms of the hits will help in unraveling the intricacies of metastasis; thereby, opening new avenues for targeting the disease.

To do this, I explored the modes-of-regulation and the mechanisms-of-action of both Impad1 and Kdelr2. The Golgi serves many vital, conserved functions in the cell, such as regulation of protein trafficking, PTMs, and secretion. In general, the Golgi dynamics and exocytosis are altered during EMT (Tan et al., 2017), and mutations in Golgi-associated genes correlates with metastasis and poor survival (Halberg et al., 2016; Tan et al., 2020). However, much remains to be discovered

regarding the underlying mechanisms adopted by regulators of Golgi-mediated exocytosis to promote cancer metastasis. Chapters 4 and 5 established Impad1 as an imperative link in connecting EMT, Golgi trafficking and secretome changes, and metastasis **(Figure 5-15)**. Importantly, I also showed that repressing Impad1 can reverse this phenotype, leading to enhanced tumor immune cell infiltration, and decreased exocytosis and invasion. Thus, signifying the potential of targeting Impad1 in order to inhibit exocytosis and metastasis. Lastly, I demonstrated that Kdelr2 regulated Golgi secretion of invasive and metastatic components independent of EMT **(Figure 5-16)**. Consequently, highlighting that EMT is sufficient but not necessary to mediate Golgi secretory functions. This indicates the presence of an EMT-independent machinery that orchestrates exocytosis through other pathways (Makhoul et al., 2019); and exposes the insufficiencies in our knowledge of the Golgi and its regulators. Further studies exploring the differences between the EMT-dependent and EMT-independent methods of Golgi secretion will advance our understanding of the epistatic pathways involving the organelle, in metastasis.

Despite the significant tumor regression seen in pre-clinical models, translating Golgi or secretion inhibitors to the clinic has proven difficult (Zappa et al., 2018). The Golgi is a stacked organelle where various proteins with different functions scaffold together to maintain Golgi integrity and function. This ensures multi-faceted roles of the Golgi as well as its associated genes, highlighting one of the biggest hurdles faced when targeting it. This is especially apparent as my data indicates that Impad1 might have roles more diverse than just regulating vesicular trafficking and Golgi-mediated exocytosis. One such process that closely relates to vesicular trafficking is endosomal

recycling. Syt11, an Impad1 interacting protein, regulates endosomes to recycle dopamine at the plasma membrane for synaptic plasticity (Shimojo et al., 2019). It is unclear whether Syt11 performs this function independent of Impad1. Therefore, Impad1 might have an hitherto unknown role in mediating endosomal trafficking at the membrane. Investigating this function of Impad1 will give us a better understanding of the crosstalk between Golgi and endosomal trafficking and how they alter the TME during metastasis. Another hurdle that hampers successful targeting of Golgi secretion in cancer metastasis, is the dynamic nature of the Golgi structure itself (Makhoul et al., 2019). My data shows that Impad1 orchestrates EMT-mediated Golgi stacking and organization. Additionally, I also determine that loss of Impad1 disrupts Golgi integrity leading to organelle fragmentation. As described in section 1.3.1, the Golgi oscillates between the condensed, ribbon-like, and fragmented architectures in a context-dependent manner; and each Golgi phase can promote cancer progression via different pathways (Rahajeng et al., 2019; Tan et al., 2017). Inhibiting Impad1 might hinder condensed Golgi structure but may lead to other malignant Golgi forms. Hence, targeting the functional morphology of the organelle is a fine-tuned balance and should be further investigated to identify the key players of the process. Future work in these two areas will give a clearer picture of the role of impad1 in the Golgi as well as in trafficking, thereby making it easier to target efficiently in the clinic.

Despite the disadvantages of the diverse and prevalent nature of the Golgi proteins scaffolding together, this ability can be used to better target the organelle and secretion. I demonstrated that repressing Impad1 affected both Golgi morphology and vesicular trafficking in lung cancer cells. However, interrupting the Impad1 interaction

with Syt11 explicitly inhibited vesicular trafficking and exocytosis but had no non-specific effects on Golgi morphology. Conversely, inhibiting the Impad1 interaction with Arf5 specifically disturbed Golgi morphology but not trafficking and secretion. Based on my work, I propose that as an alternative to inhibiting individual Golgi proteins that can alter other cellular processes, disrupting specific protein-protein interactions may be more therapeutically advantageous. Given the high degree of conservation between Rab family members and the difficulty in inhibiting specific Rabs, a similar approach is already used to target Rab proteins. Inhibitors such as RFP26 block Rab proteins from binding to its effectors and performing downstream functions (Ferro, 2020). Thus, future work investigating the protein interactions essential for regulating Golgi dynamics and secretion to drive lung cancer metastasis might make the Golgi more targetable.

Lastly, this project and the investigation of unexplored proteins like Impad1 and Kdelr2 also have implications beyond the realm of cancer. My dissertation work introduces novel regulators of Golgi dynamics, thus giving new insights into the basic biology of the organelle. Golgi secretion is a critical component in physiological processes such as neurotransmission, endocrine signaling, innate immunity, development, etc. Therefore, the finding that Impad1 and Kdelr2 affect Golgi exocytosis also deepens our understanding of these vital cellular pathways as well as the diseases associated with them. For example, loss-of-function of Impad1 is linked with chondrodysplasia, and deformed bone and cartilage development (Frederick et al., 2008; Sohaskey et al., 2008; Vissers et al., 2011). I determine that Impad1 facilitates deposition of collagens and GAGs – factors that help form the bone and

cartilage ECM. Thus, upregulating Impad1 holds potential as a treatment for these skeletal diseases. Hence, my work not only determines Impad1 as a novel target for treating lung cancer metastasis by inhibiting Golgi exocytosis, but also expands our knowledge of the role of Golgi proteins in additional physiological and pathological processes.

Bibliography

Agrawal, G. K., Jwa, N. S., Lebrun, M. H., Job, D., & Rakwal, R. (2010). Plant secretome: unlocking secrets of the secreted proteins. *Proteomics, 10*(4), 799-827. doi:10.1002/pmic.200900514

Ahn, Y. H., Gibbons, D. L., Chakravarti, D., Creighton, C. J., Rizvi, Z. H., Adams, H. P., Pertsemlidis, A., Gregory, P. A., Wright, J. A., Goodall, G. J., Flores, E. R., & Kurie, J. M. (2012). ZEB1 drives prometastatic actin cytoskeletal remodeling by downregulating miR-34a expression. *J Clin Invest, 122*(9), 3170-3183. doi:10.1172/jci63608

Albacete-Albacete, L., Sanchez-Alvarez, M., & Del Pozo, M. A. (2021). Extracellular Vesicles: An Emerging Mechanism Governing the Secretion and Biological Roles of Tenascin-C. *Front Immunol, 12*, 671485. doi:10.3389/fimmu.2021.671485

Arango Duque, G., Fukuda, M., & Descoteaux, A. (2013). Synaptotagmin XI regulates phagocytosis and cytokine secretion in macrophages. *J Immunol, 190*(4), 1737-1745. doi:10.4049/jimmunol.1202500

Bajaj, R., Kundu, S. T., Grzeskowiak, C. L., Fradette, J. J., Scott, K. L., Creighton, C. J., & Gibbons, D. L. (2020). IMPAD1 and KDELR2 drive invasion and metastasis by enhancing Golgi-mediated secretion. *Oncogene, 39*(37), 5979-5994. doi:10.1038/s41388-020-01410-z

Bento, C. F., Ashkenazi, A., Jimenez-Sanchez, M., & Rubinsztein, D. C. (2016). The Parkinson's disease-associated genes ATP13A2 and SYT11 regulate autophagy via a common pathway. *Nat Commun, 7*(1), 11803. doi:10.1038/ncomms11803

Bershadsky, A. D., & Futerman, A. H. (1994). Disruption of the Golgi-Apparatus by Brefeldin-a Blocks Cell Polarization and Inhibits Directed Cell-Migration. *Proceedings of the National Academy of Sciences of the United States of America, 91*(12), 5686-5689. doi:DOI 10.1073/pnas.91.12.5686

Bogdanov, A., Moiseenko, F., & Dubina, M. (2017). Abnormal expression of ATP1A1 and ATP1A2 in breast cancer. *F1000Res, 6*, 10. doi:10.12688/f1000research.10481.1

Bracken, C. P., Li, X., Wright, J. A., Lawrence, D. M., Pillman, K. A., Salmanidis, M., Anderson, M. A., Dredge, B. K., Gregory, P. A., Tsykin, A., Neilsen, C., Thomson, D. W., Bert, A. G., Leerberg, J. M., Yap, A. S., Jensen, K. B., Khew-Goodall, Y., & Goodall, G. J. (2014). Genome-wide identification of miR-200 targets reveals a regulatory network controlling cell invasion. *Embo j, 33*(18), 2040-2056. doi:10.15252/embj.201488641

Brandizzi, F., & Barlowe, C. (2013). Organization of the ER-Golgi interface for membrane traffic control. *Nat Rev Mol Cell Biol, 14*(6), 382-392. doi:10.1038/nrm3588

Bui, S., Mejia, I., Díaz, B., & Wang, Y. (2021). Adaptation of the Golgi Apparatus in Cancer Cell Invasion and Metastasis. *Front Cell Dev Biol, 9*. doi:10.3389/fcell.2021.806482

Burk, U., Schubert, J., Wellner, U., Schmalhofer, O., Vincan, E., Spaderna, S., & Brabletz, T. (2008). A reciprocal repression between ZEB1 and members of the miR-200 family promotes EMT and invasion in cancer cells. *EMBO Rep, 9*(6), 582-589. doi:10.1038/embor.2008.74

Byers, L. A., Diao, L., Wang, J., Saintigny, P., Girard, L., Peyton, M., Shen, L., Fan, Y., Giri, U., Tumula, P. K., Nilsson, M. B., Gudikote, J., Tran, H., Cardnell, R. J., Bearss, D. J., Warner, S. L., Foulks, J. M., Kanner, S. B., Gandhi, V., Krett, N., Rosen, S. T., Kim, E. S., Herbst, R. S., Blumenschein, G. R., Lee, J. J., Lippman, S. M., Ang, K. K., Mills, G. B., Hong, W. K., Weinstein, J. N., Wistuba, II, Coombes, K. R., Minna, J. D., & Heymach, J. V. (2013). An epithelial-mesenchymal transition gene signature predicts resistance to EGFR and PI3K inhibitors and identifies Axl as a therapeutic target for overcoming EGFR inhibitor resistance. *Clin Cancer Res, 19*(1), 279-290. doi:10.1158/1078-0432.Ccr-12-1558

Cancino, J., Jung, J. E., & Luini, A. (2013). Regulation of Golgi signaling and trafficking by the KDEL receptor. *Histochemistry and Cell Biology, 140*(4), 395-405. doi:10.1007/s00418-013-1130-9

Capitani, M., & Sallese, M. (2009). The KDEL receptor: New functions for an old protein. *Febs Letters, 583*(23), 3863-3871. doi:10.1016/j.febslet.2009.10.053

Chen, L., Gibbons, D. L., Goswami, S., Cortez, M. A., Ahn, Y. H., Byers, L. A., Zhang, X., Yi, X., Dwyer, D., Lin, W., Diao, L., Wang, J., Roybal, J., Patel, M., Ungewiss, C., Peng, D., Antonia, S., Mediavilla-Varela, M., Robertson, G., Suraokar, M., Welsh, J. W., Erez, B., Wistuba, II, Chen, L., Peng, D., Wang, S., Ullrich, S. E., Heymach, J. V., Kurie, J. M., & Qin, F. X. (2014). Metastasis is regulated via microRNA-200/ZEB1 axis control of tumour cell PD-L1 expression and intratumoral immunosuppression. *Nat Commun, 5*, 5241. doi:10.1038/ncomms6241

Deryugina, E. I., & Quigley, J. P. (2006). Matrix metalloproteinases and tumor metastasis. *Cancer Metastasis Rev, 25*(1), 9-34. doi:10.1007/s10555-006-7886-9

Du, C., Wang, Y., Zhang, F., Yan, S., Guan, Y., Gong, X., Zhang, T., Cui, X., Wang, X., & Zhang, C. X. (2017). Synaptotagmin-11 inhibits cytokine secretion and phagocytosis in microglia. *Glia, 65*(10), 1656-1667. doi:10.1002/glia.23186

Eccles, M. R., Chatterjee, A., & Rodger, E. J. (2017). Identifying drivers of metastasis; towards a systematic approach. *Translational Cancer Research, 6*, S273-S276. doi:10.21037/tcr.2017.09.52

Ferrarotto, R., Goonatilake, R., Yoo, S. Y., Tong, P., Giri, U., Peng, S., Minna, J., Girard, L., Wang, Y., Wang, L., Li, L., Diao, L., Peng, D. H., Gibbons, D. L., Glisson, B. S., Heymach, J. V., Wang, J., Byers, L. A., & Johnson, F. M. (2016). Epithelial-Mesenchymal Transition Predicts Polo-Like Kinase 1 Inhibitor-Mediated Apoptosis in Non-Small Cell Lung Cancer. *Clin Cancer Res, 22*(7), 1674-1686. doi:10.1158/1078-0432.Ccr-14-2890

Ferro, E., Bosia, C., and Campa, C. C. . (2020). RAB11-mediated trafficking and human cancers: an updated review. *Biology, 10*(1).

Fidler, I. J. (2003). The pathogenesis of cancer metastasis: the 'seed and soil' hypothesis revisited. *Nat Rev Cancer, 3*(6), 453-458. doi:10.1038/nrc1098

Franses, J. W., Baker, A. B., Chitalia, V. C., & Edelman, E. R. (2011). Stromal endothelial cells directly influence cancer progression. *Sci Transl Med, 3*(66), 66ra65. doi:10.1126/scitranslmed.3001542

Frederick, J. P., Tafari, A. T., Wu, S. M., Megosh, L. C., Chiou, S. T., Irving, R. P., & York, J. D. (2008). A role for a lithium-inhibited Golgi nucleotidase in skeletal development and sulfation. *Proc Natl Acad Sci U S A, 105*(33), 11605-11612. doi:10.1073/pnas.0801182105

Friedl, P., Locker, J., Sahai, E., & Segall, J. E. (2012). Classifying collective cancer cell invasion. *Nat Cell Biol, 14*(8), 777-783. doi:10.1038/ncb2548

Gibbons, D. L., Byers, L. A., & Kurie, J. M. (2014). Smoking, p53 mutation, and lung cancer. *Mol Cancer Res, 12*(1), 3-13. doi:10.1158/1541-7786.Mcr-13-0539

Gibbons, D. L., Lin, W., Creighton, C. J., Rizvi, Z. H., Gregory, P. A., Goodall, G. J., Thilaganathan, N., Du, L., Zhang, Y., Pertsemlidis, A., & Kurie, J. M. (2009). Contextual extracellular cues promote tumor cell EMT and metastasis by regulating miR-200 family expression. *Genes Dev, 23*(18), 2140-2151. doi:10.1101/gad.1820209

Gibbons, D. L., Lin, W., Creighton, C. J., Zheng, S., Berel, D., Yang, Y., Raso, M. G., Liu, D. D., Wistuba, II, Lozano, G., & Kurie, J. M. (2009). Expression signatures of metastatic capacity in a genetic mouse model of lung adenocarcinoma. *PLoS One, 4*(4), e5401. doi:10.1371/journal.pone.0005401

Goldenring, J. R. (2013). A central role for vesicle trafficking in epithelial neoplasia: intracellular highways to carcinogenesis. *Nat Rev Cancer, 13*(11), 813-820. doi:10.1038/nrc3601

Gregory, P. A., Bert, A. G., Paterson, E. L., Barry, S. C., Tsykin, A., Farshid, G., Vadas, M. A., Khew-Goodall, Y., & Goodall, G. J. (2008). The miR-200 family and miR-205 regulate epithelial to mesenchymal transition by targeting ZEB1 and SIP1. *Nat Cell Biol, 10*(5), 593-601. doi:10.1038/ncb1722

Gregory, P. A., Bert, A. G., Paterson, E. L., Barry, S. C., Tsykin, A., Farshid, G., Vadas, M. A., Khew-Goodall, Y., & Goodall, G. J. (2008). The miR-200 family

and miR-205 regulate epithelial to mesenchymal transition by targeting ZEB1 and SIP1. *Nat Cell Biol, 10*(5), 593-601. doi:10.1038/ncb1722

Gregory, P. A., Bracken, C. P., Smith, E., Bert, A. G., Wright, J. A., Roslan, S., Morris, M., Wyatt, L., Farshid, G., Lim, Y. Y., Lindeman, G. J., Shannon, M. F., Drew, P. A., Khew-Goodall, Y., & Goodall, G. J. (2011). An autocrine TGF-beta/ZEB/miR-200 signaling network regulates establishment and maintenance of epithelial-mesenchymal transition. *Mol Biol Cell, 22*(10), 1686-1698. doi:10.1091/mbc.E11-02-0103

Grzeskowiak, C. L., Kundu, S. T., Mo, X., Ivanov, A. A., Zagorodna, O., Lu, H., Chapple, R. H., Tsang, Y. H., Moreno, D., Mosqueda, M., Eterovic, K., Fradette, J. J., Ahmad, S., Chen, F., Chong, Z., Chen, K., Creighton, C. J., Fu, H., Mills, G. B., Gibbons, D. L., & Scott, K. L. (2018). In vivo screening identifies GATAD2B as a metastasis driver in KRAS-driven lung cancer. *Nat Commun, 9*(1), 2732. doi:10.1038/s41467-018-04572-3

Gyorffy, B., Surowiak, P., Budczies, J., & Lanczky, A. (2013). Online survival analysis software to assess the prognostic value of biomarkers using transcriptomic data in non-small-cell lung cancer. *PLoS One, 8*(12), e82241. doi:10.1371/journal.pone.0082241

Halberg, N., Sengelaub, C. A., Navrazhina, K., Molina, H., Uryu, K., & Tavazoie, S. F. (2016). PITPNC1 Recruits RAB1B to the Golgi Network to Drive Malignant Secretion. *Cancer Cell, 29*(3), 339-353. doi:10.1016/j.ccell.2016.02.013

Herbst, R. S., Heymach, J. V., & Lippman, S. M. (2008). Lung cancer. *N Engl J Med, 359*(13), 1367-1380. doi:10.1056/NEJMra0802714

Huang, C., Li, Y., Li, Z., Xu, Y., Li, N., Ge, Y., Dong, J., Chang, A., Zhao, T., Wang, X., Wang, H., Yang, S., Xie, K., Hao, J., & Ren, H. (2019). LIMS1 Promotes Pancreatic Cancer Cell Survival under Oxygen-Glucose Deprivation Conditions by Enhancing HIF1A Protein Translation. *Clin Cancer Res, 25*(13), 4091-4103. doi:10.1158/1078-0432.Ccr-18-3533

Ignashkova, T. I., Gendarme, M., Peschk, K., Eggenweiler, H. M., Lindemann, R. K., & Reiling, J. H. (2017). Cell survival and protein secretion associated with

Golgi integrity in response to Golgi stress-inducing agents. *Traffic, 18*(8), 530-544. doi:10.1111/tra.12493

Jayatilleke, K. M., & Hulett, M. D. (2020). Heparanase and the hallmarks of cancer. *Journal of Translational Medicine, 18*(1), 453. doi:10.1186/s12967-020-02624-1

Julien, S., Picco, G., Sewell, R., Vercoutter-Edouart, A. S., Tarp, M., Miles, D., Clausen, H., Taylor-Papadimitriou, J., & Burchell, J. M. (2009). Sialyl-Tn vaccine induces antibody-mediated tumour protection in a relevant murine model. *Br J Cancer, 100*(11), 1746-1754. doi:10.1038/sj.bjc.6605083

Kalluri, R., & Weinberg, R. A. (2009). The basics of epithelial-mesenchymal transition. *J Clin Invest, 119*(6), 1420-1428. doi:10.1172/jci39104

Karantza, V. (2011). Keratins in health and cancer: more than mere epithelial cell markers. *Oncogene, 30*(2), 127-138. doi:10.1038/onc.2010.456

Khajah, M. A., Mathew, P. M., & Luqmani, Y. A. (2018). Na+/K+ ATPase activity promotes invasion of endocrine resistant breast cancer cells. *PLoS One, 13*(3), e0193779. doi:10.1371/journal.pone.0193779

Kundu, S. T., Byers, L. A., Peng, D. H., Roybal, J. D., Diao, L., Wang, J., Tong, P., Creighton, C. J., & Gibbons, D. L. (2016). The miR-200 family and the miR-183~96~182 cluster target Foxf2 to inhibit invasion and metastasis in lung cancers. *Oncogene, 35*(2), 173-186. doi:10.1038/onc.2015.71

Kundu, S. T., Grzeskowiak, C. L., Fradette, J. J., Gibson, L. A., Rodriguez, L. B., Creighton, C. J., Scott, K. L., & Gibbons, D. L. (2018). TMEM106B drives lung cancer metastasis by inducing TFEB-dependent lysosome synthesis and secretion of cathepsins. *Nat Commun, 9*(1), 2731. doi:10.1038/s41467-018-05013-x

Kundu, S. T., Grzeskowiak, C. L., Fradette, J. J., Gibson, L. A., Rodriguez, L. B., Creighton, C. J., Scott, K. L., & Gibbons, D. L. (2018). TMEM106B drives lung cancer metastasis by inducing TFEB-dependent lysosome synthesis and secretion of cathepsins. *Nat Commun, 9*(1), 2731. doi:10.1038/s41467-018-05013-x

Lambert, A. W., Pattabiraman, D. R., & Weinberg, R. A. (2017). Emerging Biological Principles of Metastasis. *Cell, 168*(4), 670-691. doi:10.1016/j.cell.2016.11.037

Larsen, J. E., Nathan, V., Osborne, J. K., Farrow, R. K., Deb, D., Sullivan, J. P., Dospoy, P. D., Augustyn, A., Hight, S. K., Sato, M., Girard, L., Behrens, C., Wistuba, II, Gazdar, A. F., Hayward, N. K., & Minna, J. D. (2016). ZEB1 drives epithelial-to-mesenchymal transition in lung cancer. *J Clin Invest, 126*(9), 3219-3235. doi:10.1172/jci76725

Lim, S. M., Hong, M. H., & Kim, H. R. (2020). Immunotherapy for Non-small Cell Lung Cancer: Current Landscape and Future Perspectives. *Immune Netw, 20*(1), e10. doi:10.4110/in.2020.20.e10

Lodish H, B. A., Zipursky SL, et al. (2000a). Overview of the Secretory Pathway. In *Molecular Cell Biology* (4th ed.). New York: W. H. Freeman.

Lodish H, B. A., Zipursky SL, et al. (2000b). Protein Glycosylation in the ER and Golgi Complex. In *Molecular Cell Biology*. New York: W. H. Freeman.

Lou, Y., Diao, L., Cuentas, E. R., Denning, W. L., Chen, L., Fan, Y. H., Byers, L. A., Wang, J., Papadimitrakopoulou, V. A., Behrens, C., Rodriguez, J. C., Hwu, P., Wistuba, II, Heymach, J. V., & Gibbons, D. L. (2016). Epithelial-Mesenchymal Transition Is Associated with a Distinct Tumor Microenvironment Including Elevation of Inflammatory Signals and Multiple Immune Checkpoints in Lung Adenocarcinoma. *Clin Cancer Res, 22*(14), 3630-3642. doi:10.1158/1078-0432.Ccr-15-1434

Ma, L., & Weinberg, R. A. (2008). Micromanagers of malignancy: role of microRNAs in regulating metastasis. *Trends Genet, 24*(9), 448-456. doi:10.1016/j.tig.2008.06.004

Makhoul, C., Gosavi, P., & Gleeson, P. A. (2019). Golgi Dynamics: The Morphology of the Mammalian Golgi Apparatus in Health and Disease. *Front Cell Dev Biol, 7*, 112. doi:10.3389/fcell.2019.00112

Manshouri, R., Coyaud, E., Kundu, S. T., Peng, D. H., Stratton, S. A., Alton, K., Bajaj, R., Fradette, J. J., Minelli, R., Peoples, M. D., Carugo, A., Chen, F., Bristow, C., Kovacs, J. J., Barton, M. C., Heffernan, T., Creighton, C. J., Raught, B., & Gibbons, D. L. (2019). ZEB1/NuRD complex suppresses

TBC1D2b to stimulate E-cadherin internalization and promote metastasis in lung cancer. *Nat Commun, 10*(1), 5125. doi:10.1038/s41467-019-12832-z

Martinotti, S., & Ranzato, E. (2020). Scratch Wound Healing Assay. *Methods Mol Biol, 2109*, 225-229. doi:10.1007/7651_2019_259

McMillan, E. A., Ryu, M. J., Diep, C. H., Mendiratta, S., Clemenceau, J. R., Vaden, R. M., Kim, J. H., Motoyaji, T., Covington, K. R., Peyton, M., Huffman, K., Wu, X., Girard, L., Sung, Y., Chen, P. H., Mallipeddi, P. L., Lee, J. Y., Hanson, J., Voruganti, S., Yu, Y., Park, S., Sudderth, J., DeSevo, C., Muzny, D. M., Doddapaneni, H., Gazdar, A., Gibbs, R. A., Hwang, T. H., Heymach, J. V., Wistuba, I., Coombes, K. R., Williams, N. S., Wheeler, D. A., MacMillan, J. B., Deberardinis, R. J., Roth, M. G., Posner, B. A., Minna, J. D., Kim, H. S., & White, M. A. (2018). Chemistry-First Approach for Nomination of Personalized Treatment in Lung Cancer. *Cell, 173*(4), 864-878.e829. doi:10.1016/j.cell.2018.03.028

Meidhof, S., Brabletz, S., Lehmann, W., Preca, B. T., Mock, K., Ruh, M., Schüler, J., Berthold, M., Weber, A., Burk, U., Lübbert, M., Puhr, M., Culig, Z., Wellner, U., Keck, T., Bronsert, P., Küsters, S., Hopt, U. T., Stemmler, M. P., & Brabletz, T. (2015). ZEB1-associated drug resistance in cancer cells is reversed by the class I HDAC inhibitor mocetinostat. *EMBO Mol Med, 7*(6), 831-847. doi:10.15252/emmm.201404396

Mikoshiba, K., Fukuda, M., Ibata, K., Kabayama, H., & Mizutani, A. (1999). Role of synaptotagmin, a Ca2+ and inositol polyphosphate binding protein, in neurotransmitter release and neurite outgrowth. *Chem Phys Lipids, 98*(1-2), 59-67. doi:10.1016/s0009-3084(99)00018-3

Nakamura, N., Rabouille, C., Watson, R., Nilsson, T., Hui, N., Slusarewicz, P., Kreis, T. E., & Warren, G. (1995). Characterization of a cis-Golgi matrix protein, GM130. *J Cell Biol, 131*(6 Pt 2), 1715-1726. doi:10.1083/jcb.131.6.1715

Nieto, M. A., Huang, R. Y., Jackson, R. A., & Thiery, J. P. (2016). EMT: 2016. *Cell, 166*(1), 21-45. doi:10.1016/j.cell.2016.06.028

Ochieng, J. K., Kundu, S. T., Bajaj, R., Leticia Rodriguez, B., Fradette, J. J., & Gibbons, D. L. (2020). MBIP (MAP3K12 binding inhibitory protein) drives

NSCLC metastasis by JNK-dependent activation of MMPs. *Oncogene, 39*(43), 6719-6732. doi:10.1038/s41388-020-01463-0

Padhye, A., Konen, J. M., Rodriguez, B. L., Fradette, J. J., Ochieng, J. K., Diao, L., Wang, J., Lu, W., Solis, L. S., Batra, H., Raso, M. G., Peoples, M. D., Minelli, R., Carugo, A., Bristow, C. A., & Gibbons, D. L. (2021). Targeting CDK4 overcomes EMT-mediated tumor heterogeneity and therapeutic resistance in KRAS-mutant lung cancer. *JCI Insight, 6*(17). doi:10.1172/jci.insight.148392

Padhye, A., Ungewiss, C., Fradette, J. J., Rodriguez, B. L., Albritton, J. L., Miller, J. S., & Gibbons, D. L. (2019). A novel ex vivo tumor system identifies Src-mediated invasion and metastasis in mesenchymal tumor cells in non-small cell lung cancer. *Sci Rep, 9*(1), 4819. doi:10.1038/s41598-019-41301-2

Palade, G. (1975). Intracellular aspects of the process of protein synthesis. *Science, 189*(4200), 347-358. doi:10.1126/science.1096303

Paltridge, J. L., Belle, L., & Khew-Goodall, Y. (2013). The secretome in cancer progression. *Biochim Biophys Acta, 1834*(11), 2233-2241. doi:10.1016/j.bbapap.2013.03.014

Pangon, L., Ng, I., Giry-Laterriere, M., Currey, N., Morgan, A., Benthani, F., Tran, P. N., Al-Sohaily, S., Segelov, E., Parker, B. L., Cowley, M. J., Wright, D. C., St Heaps, L., Carey, L., Rooman, I., & Kohonen-Corish, M. R. (2016). JRK is a positive regulator of β-catenin transcriptional activity commonly overexpressed in colon, breast and ovarian cancer. *Oncogene, 35*(22), 2834-2841. doi:10.1038/onc.2015.347

Paolino, M., Choidas, A., Wallner, S., Pranjic, B., Uribesalgo, I., Loeser, S., Jamieson, A. M., Langdon, W. Y., Ikeda, F., Fededa, J. P., Cronin, S. J., Nitsch, R., Schultz-Fademrecht, C., Eickhoff, J., Menninger, S., Unger, A., Torka, R., Gruber, T., Hinterleitner, R., Baier, G., Wolf, D., Ullrich, A., Klebl, B. M., & Penninger, J. M. (2014). The E3 ligase Cbl-b and TAM receptors regulate cancer metastasis via natural killer cells. *Nature, 507*(7493), 508-512. doi:10.1038/nature12998

Parris, T. Z., Kovacs, A., Hajizadeh, S., Nemes, S., Semaan, M., Levin, M., Karlsson, P., & Helou, K. (2014). Frequent MYC coamplification and DNA

hypomethylation of multiple genes on 8q in 8p11-p12-amplified breast carcinomas. *Oncogenesis, 3*, e95. doi:10.1038/oncsis.2014.8

Peng, D. H., Kundu, S. T., Fradette, J. J., Diao, L., Tong, P., Byers, L. A., Wang, J., Canales, J. R., Villalobos, P. A., Mino, B., Yang, Y., Minelli, R., Peoples, M. D., Bristow, C. A., Heffernan, T. P., Carugo, A., Wistuba, II, & Gibbons, D. L. (2019). ZEB1 suppression sensitizes KRAS mutant cancers to MEK inhibition by an IL17RD-dependent mechanism. *Sci Transl Med, 11*(483). doi:10.1126/scitranslmed.aaq1238

Peng, D. H., Rodriguez, B. L., Diao, L., Chen, L., Wang, J., Byers, L. A., Wei, Y., Chapman, H. A., Yamauchi, M., Behrens, C., Raso, G., Soto, L. M. S., Cuentes, E. R. P., Wistuba, II, Kurie, J. M., & Gibbons, D. L. (2020). Collagen promotes anti-PD-1/PD-L1 resistance in cancer through LAIR1-dependent CD8(+) T cell exhaustion. *Nat Commun, 11*(1), 4520. doi:10.1038/s41467-020-18298-8

Peng, D. H., Rodriguez, B. L., Diao, L., Gaudreau, P.-O., Padhye, A., Konen, J. M., Ochieng, J. K., Class, C. A., Fradette, J. J., Gibson, L., Chen, L., Wang, J., Byers, L. A., & Gibbons, D. L. (2021). Th17 cells contribute to combination MEK inhibitor and anti-PD-L1 therapy resistance in KRAS/p53 mutant lung cancers. *Nat Commun, 12*(1), 2606. doi:10.1038/s41467-021-22875-w

Peng, D. H., Ungewiss, C., Tong, P., Byers, L. A., Wang, J., Canales, J. R., Villalobos, P. A., Uraoka, N., Mino, B., Behrens, C., Wistuba, II, Han, R. I., Wanna, C. A., Fahrenholtz, M., Grande-Allen, K. J., Creighton, C. J., & Gibbons, D. L. (2017). ZEB1 induces LOXL2-mediated collagen stabilization and deposition in the extracellular matrix to drive lung cancer invasion and metastasis. *Oncogene, 36*(14), 1925-1938. doi:10.1038/onc.2016.358

Petrosyan, A. (2015). Onco-Golgi: Is Fragmentation a Gate to Cancer Progression? *Biochem Mol Biol J, 1*(1). doi:10.21767/2471-8084.100006

Petrosyan, A. (2019). Unlocking Golgi: Why Does Morphology Matter? *Biochemistry (Mosc), 84*(12), 1490-1501. doi:10.1134/s0006297919120083

Pietilä, M., Sahgal, P., Peuhu, E., Jäntti, N. Z., Paatero, I., Närvä, E., Al-Akhrass, H., Lilja, J., Georgiadou, M., Andersen, O. M., Padzik, A., Sihto, H., Joensuu, H.,

Blomqvist, M., Saarinen, I., Boström, P. J., Taimen, P., & Ivaska, J. (2019). SORLA regulates endosomal trafficking and oncogenic fitness of HER2. *Nat Commun, 10*(1), 2340. doi:10.1038/s41467-019-10275-0

Pinho, S. S., & Reis, C. A. (2015). Glycosylation in cancer: mechanisms and clinical implications. *Nat Rev Cancer, 15*(9), 540-555. doi:10.1038/nrc3982

Plasterer, C., Tsaih, S. W., Lemke, A., Schilling, R., Dwinell, M., Rau, A., Auer, P., Rui, H., & Flister, M. J. (2019). Identification of a Rat Mammary Tumor Risk Locus That Is Syntenic with the Commonly Amplified 8q12.1 and 8q22.1 Regions in Human Breast Cancer Patients. *G3-Genes Genomes Genetics, 9*(5), 1739-1743. doi:10.1534/g3.118.200873

Rahajeng, J., Kuna, R. S., Makowski, S. L., Tran, T. T. T., Buschman, M. D., Li, S., Cheng, N., Ng, M. M., & Field, S. J. (2019). Efficient Golgi Forward Trafficking Requires GOLPH3-Driven, PI4P-Dependent Membrane Curvature. *Dev Cell, 50*(5), 573-585.e575. doi:10.1016/j.devcel.2019.05.038

Rahib, L., Wehner, M. R., Matrisian, L. M., & Nead, K. T. (2021). Estimated Projection of US Cancer Incidence and Death to 2040. *JAMA Network Open, 4*(4), e214708-e214708. doi:10.1001/jamanetworkopen.2021.4708

Reka, A. K., Chen, G., Jones, R. C., Amunugama, R., Kim, S., Karnovsky, A., Standiford, T. J., Beer, D. G., Omenn, G. S., & Keshamouni, V. G. (2014). Epithelial-mesenchymal transition-associated secretory phenotype predicts survival in lung cancer patients. *Carcinogenesis, 35*(6), 1292-1300. doi:10.1093/carcin/bgu041

Ricciardelli, C., Lokman, N. A., Pyragius, C. E., Ween, M. P., Macpherson, A. M., Ruszkiewicz, A., Hoffmann, P., & Oehler, M. K. (2017). Keratin 5 overexpression is associated with serous ovarian cancer recurrence and chemotherapy resistance. *Oncotarget, 8*(11), 17819-17832. doi:10.18632/oncotarget.14867

Ruggiero, C., Fragassi, G., Grossi, M., Picciani, B., Di Martino, R., Capitani, M., Buccione, R., Luini, A., & Sallese, M. (2015). A Golgi-based KDELR-dependent signalling pathway controls extracellular matrix degradation. *Oncotarget, 6*(5), 3375-3393. doi:10.18632/oncotarget.3270

Ruggiero, C., Grossi, M., Fragassi, G., Di Campli, A., Di Ilio, C., Luini, A., & Sallese, M. (2018). The KDEL receptor signalling cascade targets focal adhesion kinase on focal adhesions and invadopodia. *Oncotarget, 9*(12), 10228-10246. doi:10.18632/oncotarget.23421

Shibue, T., & Weinberg, R. A. (2017). EMT, CSCs, and drug resistance: the mechanistic link and clinical implications. *Nat Rev Clin Oncol, 14*(10), 611-629. doi:10.1038/nrclinonc.2017.44

Shimojo, M., Madara, J., Pankow, S., Liu, X., Yates, J., 3rd, Südhof, T. C., & Maximov, A. (2019). Synaptotagmin-11 mediates a vesicle trafficking pathway that is essential for development and synaptic plasticity. *Genes Dev, 33*(5-6), 365-376. doi:10.1101/gad.320077.118

Siegel, R. L., Miller, K. D., Fuchs, H. E., & Jemal, A. (2022). Cancer statistics, 2022. *CA Cancer J Clin, 72*(1), 7-33. doi:10.3322/caac.21708

Sohaskey, M. L., Yu, J., Diaz, M. A., Plaas, A. H., & Harland, R. M. (2008). JAWS coordinates chondrogenesis and synovial joint positioning. *Development, 135*(13), 2215-2220. doi:10.1242/dev.019950

Spaderna, S., Schmalhofer, O., Wahlbuhl, M., Dimmler, A., Bauer, K., Sultan, A., Hlubek, F., Jung, A., Strand, D., Eger, A., Kirchner, T., Behrens, J., & Brabletz, T. (2008). The transcriptional repressor ZEB1 promotes metastasis and loss of cell polarity in cancer. *Cancer Res, 68*(2), 537-544. doi:10.1158/0008-5472.Can-07-5682

Steeg, P. S., & Theodorescu, D. (2008). Metastasis: a therapeutic target for cancer. *Nat Clin Pract Oncol, 5*(4), 206-219. doi:10.1038/ncponc1066

Tan, X., Banerjee, P., Guo, H. F., Ireland, S., Pankova, D., Ahn, Y. H., Nikolaidis, I. M., Liu, X., Zhao, Y., Xue, Y., Burns, A. R., Roybal, J., Gibbons, D. L., Zal, T., Creighton, C. J., Ungar, D., Wang, Y., & Kurie, J. M. (2017). Epithelial-to-mesenchymal transition drives a pro-metastatic Golgi compaction process through scaffolding protein PAQR11. *J Clin Invest, 127*(1), 117-131. doi:10.1172/jci88736

Tan, X., Banerjee, P., Pham, E. A., Rutaganira, F. U. N., Basu, K., Bota-Rabassedas, N., Guo, H. F., Grzeskowiak, C. L., Liu, X., Yu, J., Shi, L., Peng,

D. H., Rodriguez, B. L., Zhang, J., Zheng, V., Duose, D. Y., Solis, L. M., Mino, B., Raso, M. G., Behrens, C., Wistuba, II, Scott, K. L., Smith, M., Nguyen, K., Lam, G., Choong, I., Mazumdar, A., Hill, J. L., Gibbons, D. L., Brown, P. H., Russell, W. K., Shokat, K., Creighton, C. J., Glenn, J. S., & Kurie, J. M. (2020). PI4KIIIβ is a therapeutic target in chromosome 1q-amplified lung adenocarcinoma. *Sci Transl Med, 12*(527). doi:10.1126/scitranslmed.aax3772

Tang, C. H., & Lu, M. E. (2009). Adiponectin increases motility of human prostate cancer cells via adipoR, p38, AMPK, and NF-kappaB pathways. *Prostate, 69*(16), 1781-1789. doi:10.1002/pros.21029

Taylor, A., Melton, J. V., Herrero, L. J., Thaa, B., Karo-Astover, L., Gage, P. W., Nelson, M. A., Sheng, K. C., Lidbury, B. A., Ewart, G. D., McInerney, G. M., Merits, A., & Mahalingam, S. (2016). Effects of an In-Frame Deletion of the 6k Gene Locus from the Genome of Ross River Virus. *J Virol, 90*(8), 4150-4159. doi:10.1128/JVI.03192-15

Thiery, J. P., Acloque, H., Huang, R. Y., & Nieto, M. A. (2009). Epithelial-mesenchymal transitions in development and disease. *Cell, 139*(5), 871-890. doi:10.1016/j.cell.2009.11.007

Tsai, J. H., & Yang, J. (2013). Epithelial-mesenchymal plasticity in carcinoma metastasis. *Genes Dev, 27*(20), 2192-2206. doi:10.1101/gad.225334.113

Uhlen, M., Fagerberg, L., Hallstrom, B. M., Lindskog, C., Oksvold, P., Mardinoglu, A., Sivertsson, A., Kampf, C., Sjostedt, E., Asplund, A., Olsson, I., Edlund, K., Lundberg, E., Navani, S., Szigyarto, C. A., Odeberg, J., Djureinovic, D., Takanen, J. O., Hober, S., Alm, T., Edqvist, P. H., Berling, H., Tegel, H., Mulder, J., Rockberg, J., Nilsson, P., Schwenk, J. M., Hamsten, M., von Feilitzen, K., Forsberg, M., Persson, L., Johansson, F., Zwahlen, M., von Heijne, G., Nielsen, J., & Ponten, F. (2015). Tissue-based map of the human proteome. *Science, 347*(6220). doi:UNSP 1260419

10.1126/science.1260419

Uhlen, M., Zhang, C., Lee, S., Sjostedt, E., Fagerberg, L., Bidkhori, G., Benfeitas, R., Arif, M., Liu, Z., Edfors, F., Sanli, K., von Feilitzen, K., Oksvold, P., Lundberg, E., Hober, S., Nilsson, P., Mattsson, J., Schwenk, J. M.,

Brunnstrom, H., Glimelius, B., Sjoblom, T., Edqvist, P. H., Djureinovic, D., Micke, P., Lindskog, C., Mardinoglu, A., & Ponten, F. (2017). A pathology atlas of the human cancer transcriptome. *Science, 357*(6352). doi:10.1126/science.aan2507

Ungewiss, C., Rizvi, Z. H., Roybal, J. D., Peng, D. H., Gold, K. A., Shin, D.-H., Creighton, C. J., & Gibbons, D. L. (2016). The microRNA-200/Zeb1 axis regulates ECM-dependent β1-integrin/FAK signaling, cancer cell invasion and metastasis through CRKL. *Scientific Reports, 6*(1), 18652. doi:10.1038/srep18652

Viotti, C. (2016). ER to Golgi-Dependent Protein Secretion: The Conventional Pathway. *Methods Mol Biol, 1459*, 3-29. doi:10.1007/978-1-4939-3804-9_1

Vissers, L. E., Lausch, E., Unger, S., Campos-Xavier, A. B., Gilissen, C., Rossi, A., Del Rosario, M., Venselaar, H., Knoll, U., Nampoothiri, S., Nair, M., Spranger, J., Brunner, H. G., Bonafe, L., Veltman, J. A., Zabel, B., & Superti-Furga, A. (2011). Chondrodysplasia and abnormal joint development associated with mutations in IMPAD1, encoding the Golgi-resident nucleotide phosphatase, gPAPP. *Am J Hum Genet, 88*(5), 608-615. doi:10.1016/j.ajhg.2011.04.002

Wang, C., Wang, Y., Hu, M., Chai, Z., Wu, Q., Huang, R., Han, W., Zhang, C. X., & Zhou, Z. (2016). Synaptotagmin-11 inhibits clathrin-mediated and bulk endocytosis. *EMBO Rep, 17*(1), 47-63. doi:10.15252/embr.201540689

Wellner, U., Schubert, J., Burk, U. C., Schmalhofer, O., Zhu, F., Sonntag, A., Waldvogel, B., Vannier, C., Darling, D., zur Hausen, A., Brunton, V. G., Morton, J., Sansom, O., Schüler, J., Stemmler, M. P., Herzberger, C., Hopt, U., Keck, T., Brabletz, S., & Brabletz, T. (2009). The EMT-activator ZEB1 promotes tumorigenicity by repressing stemness-inhibiting microRNAs. *Nat Cell Biol, 11*(12), 1487-1495. doi:10.1038/ncb1998

Wiersma, V. R., Michalak, M., Abdullah, T. M., Bremer, E., & Eggleton, P. (2015a). Mechanisms of translocation of ER chaperones to the cell surface and immunomodulatory roles in cancer and autoimmunity. *Frontiers in Oncology, 5*. doi:UNSP 7

10.3389/fonc.2015.00007

Wiersma, V. R., Michalak, M., Abdullah, T. M., Bremer, E., & Eggleton, P. (2015b). Mechanisms of Translocation of ER Chaperones to the Cell Surface and Immunomodulatory Roles in Cancer and Autoimmunity. *Front Oncol, 5*, 7. doi:10.3389/fonc.2015.00007

Wu, X., Yan, Q., Zhang, Z., Du, G., & Wan, X. (2012). Acrp30 inhibits leptin-induced metastasis by downregulating the JAK/STAT3 pathway via AMPK activation in aggressive SPEC-2 endometrial cancer cells. *Oncol Rep, 27*(5), 1488-1496. doi:10.3892/or.2012.1670

Xu, L., Zhang, Y., Qu, X., Che, X., Guo, T., Cai, Y., Li, A., Li, D., Li, C., Wen, T., Fan, Y., Hou, K., Ma, Y., Hu, X., & Liu, Y. (2017). E3 Ubiquitin Ligase Cbl-b Prevents Tumor Metastasis by Maintaining the Epithelial Phenotype in Multiple Drug-Resistant Gastric and Breast Cancer Cells. *Neoplasia, 19*(4), 374-382. doi:10.1016/j.neo.2017.01.011

Yang, J., & Weinberg, R. A. (2008). Epithelial-mesenchymal transition: at the crossroads of development and tumor metastasis. *Dev Cell, 14*(6), 818-829. doi:10.1016/j.devcel.2008.05.009

Yuan, M., Huang, L.-L., Chen, J.-H., Wu, J., & Xu, Q. (2019). The emerging treatment landscape of targeted therapy in non-small-cell lung cancer. *Signal Transduction and Targeted Therapy, 4*(1), 61. doi:10.1038/s41392-019-0099-9

Zappa, F., Failli, M., & De Matteis, M. A. (2018). The Golgi complex in disease and therapy. *Curr Opin Cell Biol, 50*, 102-116. doi:10.1016/j.ceb.2018.03.005

Zhang, P., Wei, Y., Wang, L., Debeb, B. G., Yuan, Y., Zhang, J., Yuan, J., Wang, M., Chen, D., Sun, Y., Woodward, W. A., Liu, Y., Dean, D. C., Liang, H., Hu, Y., Ang, K. K., Hung, M. C., Chen, J., & Ma, L. (2014). ATM-mediated stabilization of ZEB1 promotes DNA damage response and radioresistance through CHK1. *Nat Cell Biol, 16*(9), 864-875. doi:10.1038/ncb3013

Zheng, S., El-Naggar, A. K., Kim, E. S., Kurie, J. M., & Lozano, G. (2007). A genetic mouse model for metastatic lung cancer with gender differences in survival. *Oncogene, 26*(48), 6896-6904. doi:10.1038/sj.onc.1210493

Zheng, X., Carstens, J. L., Kim, J., Scheible, M., Kaye, J., Sugimoto, H., Wu, C.-C., LeBleu, V. S., & Kalluri, R. (2015). Epithelial-to-mesenchymal transition is dispensable for metastasis but induces chemoresistance in pancreatic cancer. *Nature, 527*(7579), 525-530. doi:10.1038/nature16064

Vita

Rakhee Bajaj was born in India. She moved to the U.S. for her Bachelor's at Michigan State University where she double majored in Biochemistry and Molecular Biology. After graduation, she moved back to India and worked as a research assistant at the Advanced Center for Treatment, Research, and Education in Cancer (ACTREC). She then came back to the U.S. and pursued her Master's at the University of Michigan, Ann Arbor in Human Genetics. In August 2016, Rakhee moved to Houston for her PhD in Cancer Biology at the University of Texas MD Anderson Cancer Center UTHealth Graduate School.